Atlantic thermohaline changes and its implications on the carbon cycle during the Last Interglacial

Augustin Kessler

Thesis for the degree of Philosophiae Doctor (PhD)
University of Bergen, Norway
2020

UNIVERSITY OF BERGEN

Atlantic thermohaline changes and its implications on the carbon cycle during the Last Interglacial

Augustin Kessler

Thesis for the degree of Philosophiae Doctor (PhD)
at the University of Bergen

Date of defense: 16.06.2020

Year: 2020

Title: Atlantic thermohaline changes and its implications on the carbon cycle during the Last Interglacial

Name: Augustin Kessler

Print: Skipnes Kommunikasjon / University of Bergen

Scientific environment

This thesis has been performed while employed at NORCE Norwegian Research Centre (former Uni Research) where I have been a member of the Earth System group and associated with the Bjerknes Centre for Climate Research under the ocean biogeochemistry theme group. Most of the courses taken during this PhD have been completed at the Geophysical Institute at the University of Bergen, but also within the research school CHESS.

This PhD position has been funded by the Research Council of Norway's (RCN) KLIMAFORSK program under the project: Thresholds for destabilizing thermohaline circulation and ocean carbon cycling in a warmer world. A close collaboration with the Laboratoire des Sciences du Climat et de l'Environnement (LSCE), France, had been made including several weeks of research stay.

Finally, the work had been presented at several occasions during the EGU general assembly in 2018 and 2019, the Bjerknes annual meeting in 2018 and during CHESS annual meetings in 2017, 2018 and 2019.

NORCE

UNIVERSITAS BERGENSIS

CHESS
Research school on changing climates in the coupled earth system

BJERKNES CENTRE for Climate Research

Acknowledgements

First I would like to thank my main supervisor *Jerry Tjiputra* and my two co-supervisors *Nadine Goris* and *Are Olsen* for allowing me to go through this PhD experience. *Jerry Tjiputra*, your strong independence and leadership skills at work inspired me. You are a hard worker and your are surrounded by this calm and positive energy that you are able to naturally share with your peers. Under your main supervision I felt trusted and knew I could rely on your support and wisdom in any situations even during the darkest time. I am happy to have been the first PhD candidate under your supervision and from my PhD perspective you did a very good job!

Next, I would like to thank the leader of the project my PhD is included in, *Ulysses Ninnemann*. You are not only a past climate bible and a great teacher, but you also share your motivation and excitement at work. I am glad that you and *Eirik Galaasen* have supported me along this three years and thus played the role of past climate mentors.

On a more personal note, I would like to thank again my co-supervisor *Nadine Goris* and the senior HR adviser *Åse Kvinnsland Kodal* for having helped me sorting things out at work during the darkest times and shown a lot of support. You are very compassionate persons that care for others. I thank also *Marie Pontoppidan* who never got tired of my attempts to talk norwegian. A special thanks to *Anthony*, *Zoé*, *Sonja*, *Lander* and, in a more general way the PhD community at the geophysical institute. Most of us shared a common passion for climbing (and little bit climate), which built true friendships in and out of the work environment. My PhD life was mostly fun thanks to you.

To *Susanne*, thank you for cheering me up and making my life exciting everyday. You never stopped listening to my complains and gave me credit for every (they were many) end-of-PhD mood swings. You kept me sane through the last year of my PhD and I surely owe you its accomplishment in good health.

Lastly, my family for supporting me through both the journey of being a PhD and the one of settling in a far country. To my *parents* for not complaining too much when it has been weeks that I haven't given any news and gently ask if I am still alive. You are always of good and wise advices and teach me how to become a better human being. To my big sister, *Violette*, you are my example to follow since I am a little boy, and I would probably not have gone through this journey if not motivated by it. Thank you, you are amazing!

Abstract

Large and abrupt changes in the Earth's climate have been recorded in marine records and Greenland ice cores and mostly characterize the last glacial period. These sudden transitions of climate, occurring within a few decades, have been associated with abrupt modifications of the Atlantic Meridional Overturning Circulation (AMOC). While this process is well studied during the glacial period, during warmer Interglacials the AMOC is thought to be relatively vigorous on multi-millennial (equilibrium) timescales. However, recent high-resolution reconstructions reveal large and sudden variations in benthic $\delta^{13}C$ during the Last Interglacial (LIG, 125ka - 115ka), as recorded in several North Atlantic sediment cores. The origin of these isotopic variations remains poorly understood and may point toward a strong modification in ocean interior biogeochemistry and/or ocean circulation.

The main goal of this thesis is to better understand the response of AMOC to warmer boundary conditions - the LIG - and its implication on the ocean carbon cycle. To this end, the first part of this thesis explores the mechanisms behind the changes in oceanic carbon cycle dynamics by comparing two simulated quasi-equilibrium states: the early, warm LIG (125 ka) versus late, cooler LIG (115 ka). The second and third parts focus on the origin of the abrupt and large changes observed in the North Atlantic benthic $\delta^{13}C$ and investigate how these short-lived transitions occur mechanistically through a series of model simulations.

Using the Norwegian Earth system Model, we found that the ocean dissolved inorganic carbon (DIC) content is considerably reduced (314.1 PgC) during the early and warm phase of the last interglacial (125ka) relative to the latter portion (115ka). The difference between these two quasi equilibrium states is attributed to the changes in biological pump and the ocean DIC disequilibrium. This difference in ocean carbon storage is particularly marked in the Atlantic Ocean where large water mass reorganization occurs, affecting the ventilation timescales and the remineralized carbon budget. While the Southern Source Water (SSW) extends across the Equator at 115ka, it retreats further south during the warmer 125ka, reducing the volume of this DIC-rich water mass within the interior Atlantic ocean. This process is found to be linked to the Southern Ocean sea-ice retreat at 125ka.

In a transient simulation, the model of intermediate complexity iLOVECLIM also simulates a smaller ocean DIC content (360 PgC) at 125ka as compared to 115ka. More interestingly, it was able to reproduce spontaneous variations in bottom water $\delta^{13}C_{DIC}$

on magnitude and timescale (multi-centennial) found in the data reconstruction during the LIG. In the model, these isotopic variations arise due to the variable influence of depleted-$\delta^{13}C_{DIC}$ SSW and enriched-$\delta^{13}C_{DIC}$ northern sourced water (NSW) — consistent with previously proposed interpretations of this proxy. The simulated water mass redistributions are associated to changes in AMOC strength suggesting that both the structure and strength of circulation could be varying under interglacial boundary conditions. Thus, our model is consistent with, and mechanistically underpins, previously proposed interpretations of this proxy as related to water mass shifts.

Finally, two regions of deep convection have been identified and linked to these sudden large transitions: (1) the region between Norway and Svalbard, and (2) south of Greenland. In the model, (1) is subject to saline Atlantic water intrusion which activates the deep convection and the ocean circulation north of the Iceland-Scotland ridge. Within a few decades — through a series of processes involving sea-ice retreat, ocean heat release, and wind-stress anomalies — the polar surface waters retreat further north along the Greenland East coastline. Intrusion of high salinity Atlantic surface waters following polar water retreat triggers increased deep convection in region (2). As a result, the AMOC strength increases. The AMOC strength relaxes back to its lower state when the subsurface water south of Svalbard have cooled enough, which allows the sea-ice to grow, cutting off the heat released to the atmosphere and induced anomalies of temperature and wind-stress.

In summary, the results presented in this study show that large changes in the interior ocean can be simulated owing to the differences in the early and late LIG boundary conditions. These differences, simulated in ocean carbon storage occur in concert with changes in (AMOC) strength and structure of circulation. Such rapid changes in circulation and ocean carbon cycling are of concern regarding the ongoing global warming as they are all affected by the changes in the sea-ice extent. More broadly the results emphasize that interglacial climate, circulation, and carbon cycling may all be abruptly perturbed. Under gradually changing climate conditions our model suggests AMOC state changes could even arise spontaneously due to coupled atmosphere-ocean-sea ice feedbacks.

List of papers

1. Augustin Kessler, Eirik V. Galaasen, Ulysses S. Ninnemann, and Jerry F. Tjiputra, (2018): *Ocean carbon inventory under warmer climate conditions the case of the Last Interglacial*, Climate of the Past, 14(12), 1961–1976. doi: 10.5194/732cp-14-1961-2018.

2. Augustin Kessler, Nathaelle Bouttes, Didier M. Roche, Ulysses S. Ninnemann, Eirik V. Galaasen, and Jerry F. Tjiputra (in revision): *Atlantic Meridional Overturning Circulation and $\delta^{13}C$ variability during the Last Interglacial*, Paleoceanography and Paleoclimatology.

3. Augustin Kessler, Nathaelle Bouttes, Didier M. Roche, Ulysses S. Ninnemann, and Jerry F. Tjiputra (submitted): *Dynamics of spontaneous (multi) centennial-scale1variations of the Atlantic Meridional Overturning Circulation strength during the Last Interglacial*, Paleoceanography and Paleoclimatology.

Contents

Chapter 1

Introduction

1.1 Context

Human activities cause the global climate to change rapidly through unabated release of greenhouse gas into the atmosphere. Over the last decades multiple analyse of data from satellites, *in-situ*, and multiple proxy sources show that the climate is already changing toward a warmer Earth system. However, the magnitude and the extent of changes remain difficult to predict in future projections. A large remaining uncertainty is to potential of change in the Thermohaline Circulation (THC) and its consequences for climate, draught, regional sea level and ocean carbon uptake. An abrupt change of this circulation would have dramatic and widespread consequences on the ecosystems and our society.

The Intergovernmental Panel on Climate Change (IPCC) assessment report 2013 suggests that changes in the Atlantic Meridional Overturning Circulation (AMOC), a major component of the THC, are likely to occur by the end of the century suggesting the decline of its strength from the current state by about 11% (32%) under low (high) CO_2 emission scenario (*Stocker et al.*, 2014). However, the risk of an abrupt climate change to occur, associated with a rapid collapse the AMOC, is not excluded and one recent study assessed the chance for collapse at up to 15% (*Castellana et al.*, 2019) while recent observations hint that the AMOC may have already started changing (*Smeed et al.*, 2014). Therefore it is crucial to narrow the uncertainties both in its likelihood for change but also its potential impacts.

Predicting future climate variability and impacts remains challenging due to the complexity of the system involved and climate models are the principle tools that have been developed to provide comprehensive and physically consistent insights into the climate system. Despite their comprehensiveness, they still provide imperfect representations of the complex Earth systems. Studying past climate variability offers crucial opportunities to test these models and their fidelity in representing the full complexity and behavior of the natural system. Thus, studying past climate variability of warm

Earth system periods is key step in potentially elucidating the mystery of the future climate under the ongoing global warming.

1.2 Scientific background

1.2.1 The Atlantic Meridional Overturning Circulation

The global ocean overturning circulation (Fig. 1.1a) is defined as the large scale movement of waters in the ocean basins, namely the Atlantic, Pacific and Indian basins. It is mainly driven by two distinct physical mechanisms interacting with each other (*Rahmstorf*, 2006): (1) the wind-driven current, and (2) the thermohaline (THC) current. While (1) is the direct transport of water masses induced by the friction with the wind at the ocean's surface, (2) is induced by the changes in water mass density with the fluctuation of its temperature and salt content through the water column. Both processes result in horizontal (Fig. 1.1a, arrows) and vertical (Fig. 1.1a, orange patches) water mass transport, which carry with them physical and biogeochemical properties, e.g., temperature and carbon, across the globe.

The Atlantic Meridional Overturning Circulation (AMOC) has emerged as an important metric for describing the overturning circulation in the Atlantic and is defined as the north-south flow across hemispheres connecting surface and deep water masses (Fig. 1.1b). It is characterized by two overturning cells, which are affected by both the wind and the changes in temperature-salinity. The upper cell transports relatively warm and salty near-surface water northwards where it gradually cools, becomes denser, and ultimately sinks into the ocean interior. Currently the sinking sites are mainly localised in the Labrador and Nordic Seas. Together they form the North Atlantic Deep Water (NADW), which is a cold and deep southward flow (Fig. 1.1b, blue arrow) representing the starting point of the AMOC. The lower cell consists of a bottom northward flow of dense and cold Antarctic Bottom Water (AABW, Fig. 1.1b, purple), which is produced in the Southern Ocean (*Foster and Carmack*, 1976; *Kuhlbrodt et al.*, 2007). This northward flow at the bottom of the Atlantic ocean is compensated by the southward deep return flow where both NADW and AABW mix and, after transformation within the indo-pacific (*Talley*, 2013), are eventually returned to the surface in the Southern Ocean via the wind-driven upwelling (*Toggweiler and Samuels*, 1995).

The climate of the North Atlantic is intimately related to the AMOC, which has the unique characteristic of transporting heat from the Southern Hemisphere to the Northern Hemisphere. Consequently, a significant amount of heat, roughly 1.1 PW (PW = 10^{15} Watt) at $20°N$, is transported from the tropics to the northern high latitudes (*Buckley and Marshall*, 2016; *Ganachaud and Wunsch*, 2000). This heat is released to the atmosphere and contributes to the mild climate in the northwest Europe, which is up to $6°C$ warmer than its counterpart in the Pacific (*Palter*, 2015). On the other hand, it also plays an essential role in regulating the uptake of atmospheric CO_2 in the North Atlantic and transporting it to the interior ocean for long-term storage (also known

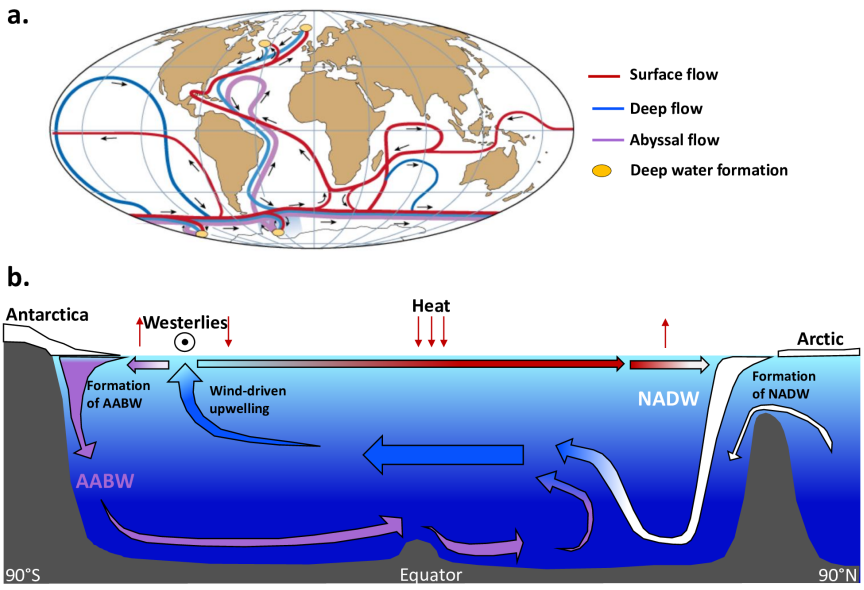

Figure 1.1: ***a.*** *Simplified schematic of the global ocean circulation, illustrating the overall water mass flow associated to their relative depths: surface (red), deep (blue) and abyssal (purple). The associated deep water formation regions are represented by the orange patch. Modified from Rahmstorf (2002). A simplified schematic of the Atlantic Meridional Overturning Circulation (AMOC) in its current operating mode is represented in* ***b.***

as the solubility pump), thus making the AMOC a critical component of the climate system (*Clark et al.*, 2002; *Rahmstorf*, 2002).

An important factor that characterizes the unique conditions of the Atlantic basin, in addition to the transport of heat across the Equator, is its unusually high salinity. This is maintained by an excess of evaporation over precipitation, river runoff and ice melt (*Emile-Geay et al.*, 2003; *Warren*, 1983), and the transport of saline water through the Agulhas leakage along the South African coastline (*De Ruijter et al.*, 1999). This preconditions the Atlantic for deep water convection as these high-salinity water masses cools in the northern high latitudes. Interestingly, the AMOC also self-sustains its northward salt advection. Consequently, a strong AMOC state (as is it today) maintains suitable conditions for deep convection to occur by transporting more salt than at weaker state, thus providing a powerful AMOC feedback called salt-advection feedback. Consequently, the concept of an AMOC collapse has emerged as the salt-advection feedback can also further reduce a declining AMOC as less salt would be advected into the convection regions. Model studies predict global consequences associated to an AMOC collapse, possibly affecting the the Atlantic sink of CO_2,the marine biology, the Intertropical Convergence Zone (ITCZ), the precipitation pattern and the air temperature (*Schmittner*, 2005; *Schuster and Watson*, 2007; *Vellinga and Wood*, 2002). For example, a disruption of the AMOC could generate a cooling over

the North Atlantic of up to 10°*C* (*Liu et al.*, 2017).

1.2.2 AMOC and abrupt climate changes

Evidence from the paleoclimate records over the last Glacial period (115,000 - 11,700 years ago) have been the first to point toward a series of global climate shifts, spanning almost the full range of glacial to interglacial conditions, involving large modifications in the pattern of precipitations, surface air temperature, ocean biogeochemistry and greenhouse gas concentration (*Clement and Peterson*, 2008; *Schmittner and Galbraith*, 2008; *Voelker et al.*, 2002). These global climate shifts are represented by 25 abrupt variations, notably recorded in the glacial ice of Greenland (Fig. 1.2a), and have been commonly referred to as Dansgaard-Oeschger (D-O) events (*Dansgaard et al.*, 1984). They are characterized by rapid transitions within a few decades from cold (referred to as stadials) to warm (referred to as interstadials) intervals of millennial-timescale (*Voelker et al.*, 2002).

Ever since, the scientific community has attempted to elucidate the plausible mechanisms responsible for these past climate shifts and have suggested several potential processes: the sea-ice and its feedback on air-sea heat exchange and albedo (*Denton et al.*, 2005; *Gildor and Tziperman*, 2003; *Kaspi et al.*, 2004; *Li et al.*, 2005); tropical processes, as these regions connect both hemispheres and show large hydrologic variability which can potentially alter the water vapor (a powerful greenhouse gas) concentration in the atmosphere (*Clement et al.*, 2001; *Pierrehumbert*, 2000); the changes in the northward heat transport associated with modification in AMOC structure (and strength) (*Clark et al.*, 2002; *Rahmstorf*, 2002), which to this date seem to prevail. Notably, the temperature reconstruction recorded in the Antarctica's ice sheet is in antiphase from that recorded in Greenland (*Barker et al.*, 2011; *Blunier and Brook*, 2001), provides compelling evidence for climate variability consistent with the hypothesis involving the AMOC-induced heat transport changes where a reduction in northward heat transport ultimately leads to warming of the Southern Hemisphere (*Crowley*, 1992).

The idea that the AMOC may have several equilibrium states, which can be triggered to transition by input of freshwater, was first invoked in the pioneering modeling work of *Stommel* (1961), who described convection in a system affected by both temperature and salinity, thus highlighting the importance of the THC. It is only after the discovery of the last glacial climate shifts, more than two decades later, that the full relevance of his work was recognized. During some of these D-O events, layers of ice-rafted detritus (IRD) have been identified in marine sediment cores, hinting for drifting icebergs that periodically have spread over the convection areas of the North Atlantic (*Bond and Lotti*, 1995; *Broecker*, 1994; *Hemming*, 2004; *MacAyeal*, 1993). These cooling events have been referred to as Heinrich events and are associated with large IRD layers extending across the North Atlantic marking collapse of the Laurentide ice sheet (*Heinrich*, 1988). Thus, the idea of periodical large freshwater input over the convection zones of the North Atlantic became a convincing way of explaining the climate shifts through the variations of the AMOC and its production of NADW. Three

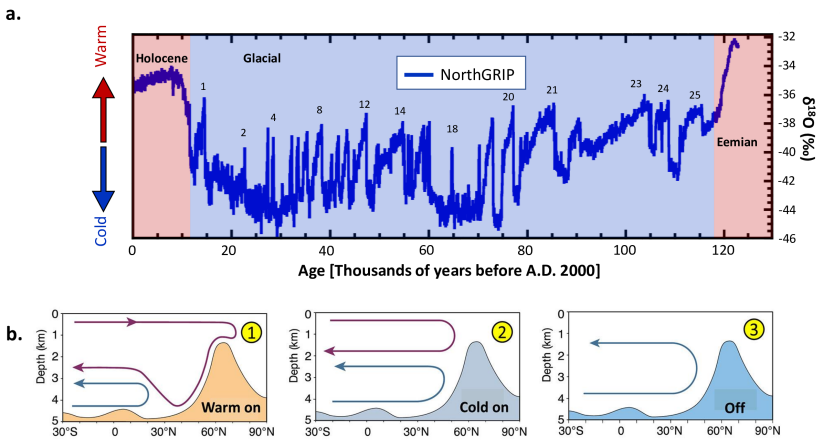

Figure 1.2: ***a.*** *Profiles of $\delta^{18}O$ recorded in an ice core from the North Greenland project covering the last 123,000 years (modified from North Greenland Ice Core Project members (2004)). This oxygen isotope is a proxy for air temperature and reveals its variations over Greenland during the last Glacial period fluctuating 25 times between cold and warm conditions known as Dansgaard-Oeschger (D-O) events.* ***b.*** *Simplified schematic of the three different modes of the Atlantic Meridional Overturning Circulation (AMOC), which characterize the last glacial period. The purple arrow represents the upper cell of the AMOC and the formation of North Atlantic Deep Water (NADW). The blue arrow represents the bottom cell and the penetration of southern Source Water (SSW) — today known as Antarctic Bottom Water (AABW). Panel (b) is modified from Rahmstorf (2002)).*

different operating modes (*Rahmstorf*, 2002) of the AMOC have been proposed in correlation with marine paleoclimate records pointing the rate of NADW production as main AMOC control (*Henry et al.*, 2016; *Lynch-Stieglitz*, 2017). Figure 1.2b illustrates these three operating modes: (1) the warm circulation state of today, characterized by a vigorous upper overturning cell transporting heat to the northern high latitudes and generating deep water in the Greenland-Iceland-Norwegian Seas; (2) the cold circulation state, which produces deep water further south, in the subpolar North Atlantic, and exhibits further penetration of southern source waters while the upper cell is shallower; (3) the (cold) off circulation state, which is typical of Heinrich events with a complete collapse of the NADW formation (*Henry et al.*, 2016; *Rahmstorf*, 2002).

Motivated by these interpretations, generations of numerical models have been testing the sensitivity of the AMOC to freshwater by performing freshwater "hosing" experiments (e.g., *Ganopolski and Rahmstorf* (2001); *Kageyama et al.* (2010); *Liu et al.* (2009); *Menviel et al.* (2014); *Schmittner et al.* (2007); *Stouffer et al.* (2006)). These model studies confirmed the ability of a large freshwater input over the North Atlantic Ocean to shut down the AMOC and generate cooler surface ocean in the high latitudes consistent with the proxy data. However, they also demonstrated that the AMOC responses to freshwater input vary as a function of background climate state and experimental design. The extent to which the recorded abrupt climate changes from the last glacial period were caused by only freshwater input remains under debate as many recent studies point out inconsistencies in the interpretation of the proxies and model set-

tings. For example, *Gutjahr and Lippold* (2011) showed for the Heinrich event 2 that the widespread deposition of IRD occurred 2,000 years after the AMOC had started weakening, while the proxy based study of *Barker et al.* (2015) revealed that the IRD deposition systematically lags the onset of the North Atlantic cooling.

In the mid noughties, *de Vries and Weber* (2005) and *Weber and Drijfhout* (2007) found that the dynamical regime of the AMOC comes from its capacity to export/import freshwater in the convection regions of the North Atlantic. To do so, they defined the metric, called F_{ovS}, representing the flux of freshwater (usually evaluated at $34°S$) induced by the overturning circulation itself, whose sign predicts the stability of the regime. A positive F_{ovS} translates to a mono-stable regime where freshwater is imported toward the convection sites. Consequently, a reduction of the AMOC also weakens the import of freshwater, creating denser (more saline) water masses in the convection regions, and leads to an increase in the overturning circulation. A negative F_{ovS} corresponds to a bi-stable regime where freshwater is exported from the convective regions, generating a saline dense water mass. Thus, a reduction of the AMOC also weakens the production of dense saline water, thus further decreasing the AMOC. This discovery was followed by a myriad of model analysis through the full spectrum of complexity and under varying boundary conditions. It revealed that a majority of the current climate models exhibit a mono-stable AMOC regime (*Drijfhout et al.*, 2011; *Weaver et al.*, 2012), which potentially generates a too stable AMOC (*Liu et al.*, 2017). However, they also showed that multiple equilibria states of the AMOC are closely linked to the salt-advection feedback, which is sensitive to model details (*Weijer et al.*, 2019).

Meanwhile, other model simulations showed that internal processes to the atmosphere-ocean system can generate spontaneous AMOC variations without any changes in the freshwater input (*Arzel et al.*, 2012; *Drijfhout et al.*, 2013; *Friedrich et al.*, 2010; *Sakai and Peltier*, 1997; *Schulz et al.*, 2002; *Vettoretti and Peltier*, 2015; *Winton*, 1993). These model studies link the abrupt transitions between cold and warm state to the changes in vertical density gradient in the North Atlantic, while others highlight the instability of the sea-ice extent acting like an ocean heat insulator until it crosses a certain threshold and collapse from below (*Li et al.*, 2005, 2010; *Petersen et al.*, 2013). To summarize, both externally-forced and spontaneous AMOC variations seem strongly dependent on the background climate state and are consistent in the general features of the atmospheric, oceanic and sea-ice response. The addition of freshwater seems, however, to lead to a more complete shut down of the AMOC (*Brown and Galbraith*, 2016), which is of concern in the context of future global warming and ice sheet melting.

1.2.3 Climate stability under warmer boundary conditions

Warm interglacial climates strongly differ from cold glacial intervals (e.g., ice-sheet extent, sea level, atmospheric CO_2 levels and global surface temperature), and the incredibly persistent mild climate recorded in the deposited ice of Greenland over the last 8,000 years has led to the initial idea that interglacials were relatively stable and asso-

ciated with a relatively strong AMOC. However, the current stability seems to be more an exception than a rule as several Atlantic and European records indicate the presence of climate instability during the Last Interglacial (LIG, 130,000 - 115,000 years ago) (*Demény et al.*, 2017; *Fronval and Jansen*, 1996; *Irvalı et al.*, 2016; *Mokeddem et al.*, 2014; *Tzedakis et al.*, 2018), and a recent study showed that this high variability could apply also for other Interglacials of the past 500,000 years, at least for deep water properties (*Galaasen et al.*, 2020).

The LIG, also called Marine Isotope Stage (MIS) 5e or Eemian, is characterized in its early phase by a high insolation factor in the northern high latitudes due to favorable orbital configuration, which results in this period being 1-2°*C* warmer globally and the warmest interval of the past 250,000 years (*Kaspar et al.*, 2005; *Otto-Bliesner et al.*, 2006). Several aspects of this period are particularly interesting as they share similar features with the model projections of our future climate if anthropogenic greenhouse gas emissions continue unabated, such as high-latitudes warming (*Hoffman et al.*, 2017; *Otto-Bliesner et al.*, 2013), Greenland ice-sheet reduction, and higher sea level (*Kopp et al.*, 2009; *Otto-Bliesner et al.*, 2006). Nevertheless, even if this period provides a study case for a climate system under warmer-than-today conditions, the reader should keep in mind that many other aspects were also different such as the orbital configurations and the greenhouse gas concentration.

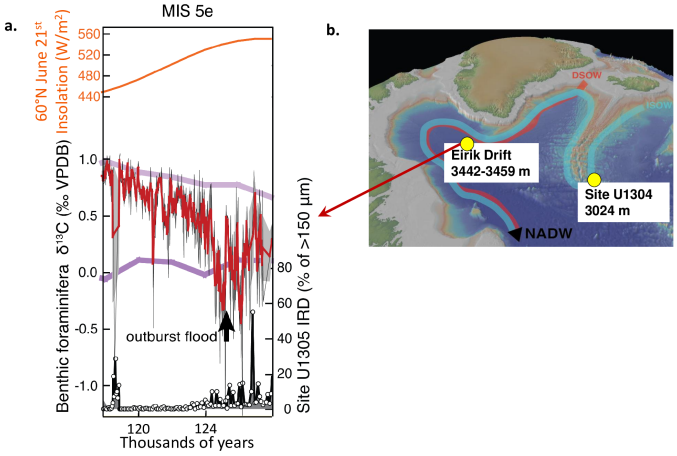

Figure 1.3: a. Bottom water $\delta^{13}C$ reconstruction from Eirik Drift (red, three-point running mean; shading, standard error of the three-point window) over the Last Interglacial (LIG). Abrupt variations of up to 0.7 ‰ are depicted comparable to the glacial-interglacial magnitude. The light and dark purple tick lines denote the mid-depth North and deep South Atlantic composites, representing characteristic Northern and Southern Source Waters, respectively. The 65°N insolation at 21 June is represented in orange, while Eirik Drift IRD records is shown by the black thick line (in %) with arrows denoting freshwater outburst floods. Modified from (Galaasen et al., 2020). The panel (b) shows the localisation of the Eirik Drift sediment core (MD03-2664), noting that abrupt changes in bottom water $\delta^{13}C$ have also been found at Gardar Drift (Site U1304) also shown on the map.

The difficulty in assessing the climate variability of the LIG (and other past period)

resides in the resolution of the climate records and our ability to reconstruct and interpret the data. On the multi-millennial timescale, the rate of NADW production is relatively vigorous and stable (*Adkins et al.*, 1997; *Galaasen et al.*, 2014; *Oppo et al.*, 1997). On the other hand, very little is known about the shorter-term variability as the resolution of proxies is often too low to provide much information about higher frequency changes. However, using North Atlantic proxy data with a resolution better than a century, recent studies revealed large and irregular swings of water mass distribution (*Galaasen et al.*, 2014, 2020; *Hodell et al.*, 2009) showed by sudden variations of the stable isotope ratios of carbon ($\delta^{13}C$), measured in the calcareous shells of bottom-dwelling foraminifera. This discovery indicated that interglacial dynamics do not exclude rapid changes in water mass influence and that this could affect the entire water column down to the sea floor.

The link between the variations measured in benthic $\delta^{13}C$ and the ocean circulation is, however, not straightforward and requires additional tools such as model simulations to evaluate how they are associated (*Bakker et al.*, 2015). Nevertheless, the importance of freshwater in shaping the structure of the AMOC and the production of NADW during that period is also highlighted via the presence of IRD. This relationship is most apparent during the early part of the LIG, when ice melting was strongest due to the final retreat of the Laurentide ice sheet from the previous glaciation (*Colville et al.*, 2011; *Oppo et al.*, 1997; *Otto-Bliesner et al.*, 2006). In some respects this relationship between circulation and freshwater (IRD) is similar to that observed for the glacial period and D-O variability — although deviations occur over shorter timescales during the LIG. However, not all changes in deep ocean chemistry are associated with IRD as shown in Fig. 1.3a. Thus not only is the connection between $\delta^{13}C$ and circulation uncertain, the drivers of these changes also remain enigmatic. In order to better understand what can trigger $\delta^{13}C$ variations it is instructive to review the mechanisms leading to different $\delta^{13}C$ values in the interior ocean.

1.2.4 Physical and biogeochemical mechanisms behind $\delta^{13}C$

Carbon isotopes provide clues to past carbon cycling changes in the Earth System. The different behaviour of the light ^{12}C and heavy ^{13}C stable forms during reaction and exchange of carbon leads to a fractionation of the carbon isotopes in the different carbon reservoirs. The ratio of these isotopes provide important insight into these fractionating processes and the size of enriched or depleted reservoirs.

The $\delta^{13}C$ represents the standardized ratio $^{13}C/^{12}C$ (*Zeebe and Wolf-Gladrow*, 2001), which is expressed in permil (‰) units as follow:

$$\delta^{13}C = \left(\frac{(^{13}C/^{12}C)}{(^{13}C/^{12}C)_{standard}} - 1\right) \times 1000 \tag{1.1}$$

The $(^{13}C/^{12}C)_{standard}$ ratio is the Pee Dee Belemnite ratio which provides the "zero"

point for comparing isotopic variations (*Craig*, 1957). The ^{13}C is slightly heavier than ^{12}C due to its additional neutron in its core, which generates a fractionation effect during air-sea gas exchange and marine biological activities (photosynthesis) and causing the $\delta^{13}C$ to change in the water column (*Eide et al.*, 2017a; *Lynch-Stieglitz et al.*, 1995; *Schmittner et al.*, 2013; *Zhang et al.*, 1995). The terrestrial and marine organisms preferentially incorporate the lighter ^{12}C over ^{13}C during photosynthesis, which lowers the isotopic ratio (^{13}C/^{12}C) in plants and phytoplanktons. Consequently, at the surface of the ocean, where photosynthesis takes place, more ^{12}C is consumed over ^{13}C, leaving the near surface water with a higher ^{13}C/^{12}C ratio, therefore increasing $\delta^{13}C$. With time and gravity, the ^{12}C-rich biological particles eventually sink through the water column and to the deep ocean where they are remineralized. This releases the ^{12}C to the surrounding waters, decreasing the ^{13}C/^{12}C ratio and $\delta^{13}C$ values in the deep ocean. In other words, the surface ocean has a relatively high $\delta^{13}C$ while at depth, the older water masses generally have lower $\delta^{13}C$ (Fig. 1.4). Both signatures are imprinted in the calcareous shells of planktic (surface) and benthic (deep) foraminifera in the sediments which provide an archive spanning millions of years of history (*Hilting et al.*, 2008).

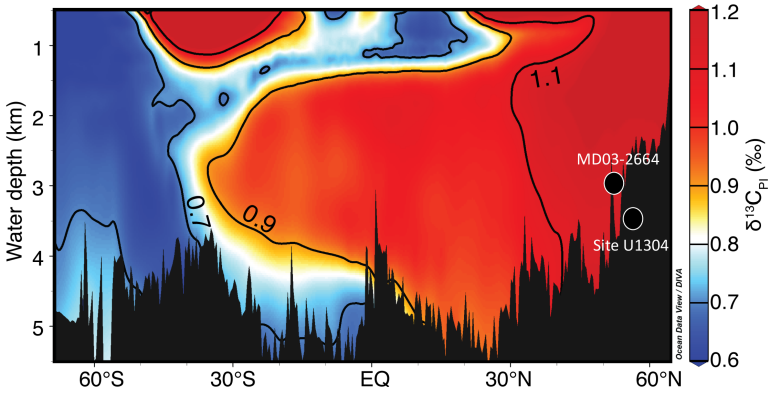

Figure 1.4: North-south section of the pre-industriel $\delta^{13}C$ (Eide et al., 2017b) in the Atlantic Ocean. Modified from Galaasen et al. (2020). The regions with high $\delta^{13}C$ signature correspond to the newly ventilated North Atlantic Deep Water (NADW), commonly called Northern Source Water (NSW).

As both the mechanisms of biological pump and the air-sea gas exchange are different between the North Atlantic and the Southern Ocean, the NADW and AABW have very distinct $\delta^{13}C$ signatures (Fig. 1.4). The low biological net efficiency (iron limited) of the Southern Ocean results in low-$\delta^{13}C$ (AABW, approximately the blue shades below 4000 m depths), as opposite to the high-$\delta^{13}C$ NADW, which is characterized with a more efficient biological pump. Consequently, the analysis of $\delta^{13}C$ is often used to reconstruct the variations in ocean circulation (*Duplessy et al.*, 1988) and strength of biological pump (*Crucifix*, 2005; *Curry and Oppo*, 2005; *Eide et al.*, 2017a; *Morée et al.*, 2018). Despite its vast potential, significant uncertainties remain in its interpretation as a proxy of past carbon cycle and circulation changes (*Broecker and McGee*, 2013; *Oliver et al.*, 2010), as well as in the interpretation with regard to modern ocean data and as a proxy for ocean carbon cycle changes (*Eide et al.*, 2017a,b), emphasizing the

necessity of additional model-data comparison. Besides, the air-sea gas exchange and terrestrial carbon storage also play an important role in setting the values of $\delta^{13}C$ in the ocean. For example, the dust-borne iron and atmospheric CO_2 levels are suggested to be closely linked to the $\delta^{13}C$ variations of the past 350,000 years (*Ziegler et al.*, 2013), while the terrestrial carbon storage seems also to play an important role in setting the mean ocean value of $\delta^{13}C$ for glacial-interglacial transitions (*Menviel et al.*, 2017).

Chapter 2

Motivations and objectives

The recent discovery of high frequency variability in the North Atlantic $\delta^{13}C$ bottom water during the Last Interglacial period questions the relatively well established idea that warm interglacials are stable. This challenge arises due to the unusually high-resolution of the latest proxy results, down to or even surpassing centennial scale resolution. The role of freshwater still seems important in disturbing the production of NADW during the early LIG, due to the relic influences of the previous glacial period, and at its very end when the warm climate had slowly cooled approaching the next glaciation. The current interpretation of these reconstructed $\delta^{13}C$ variations is that shifts occur in water masses influencing the sediment core sites. Bottom waters appear to vary between $\delta^{13}C$ values typical of the Southern Source Water (SSW) and the Northern Source Water (NSW) (*Galaasen et al.*, 2014; *Hodell et al.*, 2009), hinting at more unstable Earth system than previously thought for the LIG (and in general during Interglacials). Yet, the interpretation of these apparent carbon isotope changes in terms of their implications for both ocean circulation and carbon cycle changes remains uncertain — providing a central motivation for this thesis.

First, changes in the ocean carbon cycle during this period may have altered the distribution of carbon in the ocean interior between the warm early and cold late LIG, while the atmospheric CO_2 remained relatively stable around 270-280 ppm (*Lourantou et al.*, 2010; *Schneider et al.*, 2013). Secondly, the interpretation of the proxy remains poorly tested where the connection between bottom water $\delta^{13}C$ and ocean circulation changes is not straightforward (*Bakker et al.*, 2015). Can the current generation of models reproduce such variability in the bottom water $\delta^{13}C$ within the timescale (centennial-scale) and magnitudes observed in the data reconstructions? Can these be linked to such reorganization of the AMOC during the LIG? Finally, as not all $\delta^{13}C$ variations have been associated with freshwater (IRD), what other mechanisms may trigger and contribute AMOC instability during the LIG?

2.1 Introduction to the papers

In this thesis I present three papers that address each of the issues outlined above. Consequently, this thesis aims to provide more insights into the $\delta^{13}C$-AMOC relationship during the LIG, and to better understand the major changes in the ocean carbon cycle that could have affected the distribution of this tracer during this period.

Paper I, explores the mechanisms leading to modifications of the oceans carbon cycle and budget during the LIG, using a state-of-the-art Earth system model. The main objective of this paper is to identify the most sensitive regions that undergo carbon dynamic changes between the warm and early LIG (125ka), as opposite to the colder and late LIG (115ka), and establish the mechanisms leading to these changes. Thus, Paper I addresses the question:

- What processes are leading to the changes in the ocean carbon cycle and budget under the warm boundary condition of the LIG?

Paper II, is a model-data comparison between the model of intermediate complexity iLOVECLIM and the reconstructed data of North Atlantic bottom water $\delta^{13}C$ during the LIG at the Eirik and Gardar drifts (*Galaasen et al.*, 2014; *Hodell et al.*, 2009). This paper is a first order test to the previous interpretation of the proxy and therefore is centered around the following questions:

- Can the current generation of models reproduce the variability in the bottom water $\delta^{13}C$ within the timescale (centennial-scale) and magnitudes observed in the high-resolution data reconstructions of the North Atlantic during the LIG, and is the reorganization of the AMOC responsible for it?

Finally, *Paper III* investigates in more detail the mechanisms and threshold giving rise to AMOC variations in the model by simulating an additional set of transient experiments during the LIG. The aim of this study is to elucidate the mechanisms behind spontaneous or unforced AMOC variability simulated under LIG boundary conditions and determine the model specific thresholds/regime under which such variability can occur. Hence, this paper addresses the question:

- What are the physical mechanisms and boundary conditions responsible for the simulated spontaneous AMOC variations during the LIG?

Together, these papers provide a relatively complete overview of the ocean dynamics from the LIG, from the changes in the carbon cycling, to the stability of the ocean circulation and its interpretation though the $\delta^{13}C$ tracer.

Chapter 3

Summary of results

Paper I: Augustin Kessler, Eirik V. Galaasen, Ulysses S. Ninnemann, and Jerry F. Tjiputra, (2018): *Ocean carbon inventory under warmer climate conditions the case of the Last Interglacial*, Climate of the Past, 14(12), 1961–1976. doi: 10.5194/732cp-14-1961-2018.

Using the state-of-the-art Earth system model NorESM1-ME, we simulated two states of the penultimate interglacial period (the warm 125ka vs the cold 115ka) to make a first attempt at quantifying the biogeochemical and physical processes causing the ocean carbon storage to change under different (interglacial) orbital configurations and background climates.

Significant reductions in the ocean carbon storage capacity (314.1 PgC) are found under the warmer climate at 125ka where the reduction in the biological pump plays a major role, contributing to more than 48% of the ocean carbon budget decrease. This reduction occurs mainly in the interior ocean while there is a weak increase in the top 1000 to 1500 m depth. Two factors are found to mainly contribute to the drop in carbon budget in the deeper interior ocean: (1) a weaker biological component from both the soft-tissue and the carbonate pumps that dominates at the depth between 1000 and 3000 m, and (2) a stronger disequilibrium effect of DIC in the bottom waters.

The Atlantic Ocean is revealed as the most sensitive basin to changes in the biological pump where shorter residence time of interior deep water masses lead the ocean carbon budget to decrease due to higher ventilation rate (i.e., a reduced time for remineralization of the organic matters). The reorganization of the NSW-SSW distribution in the interior ocean also reflects the higher ventilation rate at 125ka and arises from the southward retreat at depth of the poorly ventilated SSW when the Southern Ocean sea-ice retreats.

At the surface ocean, heterogeneous changes in phosphate availability and carbon export production especially between the Atlantic and Pacific basins are found, suggesting different basin responses of the biogeochemical divide to warmer boundary conditions. Nevertheless, this study suggests that the Atlantic sector of the Southern

Ocean is most sensitive to past climate change and hence could be a potential indicator of similar large-scale circulation changes and carbon sequestration rate in the future.

Paper II: Augustin Kessler, Nathaelle Bouttes, Didier M. Roche, Ulysses S. Ninnemann, Eirik V. Galaasen, and Jerry F. Tjiputra (in revision): *Atlantic Meridional Overturning Circulation and $\delta^{13}C$ variability during the Last Interglacial*, Paleoceanography and Paleoclimatology.

In this study, we compare the bottom water $\delta^{13}C$ from two sediment cores in the North Atlantic (MD03-2664, Eirik Drift and Site U1304, Gardar Drift), that show high frequency variability during the LIG, with a transient simulation from 125ka to 115ka. The simulation is forced only with natural greenhouse gas and orbital evolution, using the iLOVECLIM Earth system model of intermediate complexity. Thereby, we make a first order test of whether or not this model is able to reproduce the bottom $\delta^{13}C$ variations in this region, and if the previous interpretation involving modifications in water mass distributions of SSW and NSW in the deep ocean are mechanistically plausible.

Our simulation reproduces the short timescale (centennial) and much of the magnitude (up to 0.65 ‰) of bottom water $\delta^{13}C$ variations inferred from high resolution proxy reconstructions at two core locations. Furthermore, the simulated offset in bottom water $\delta^{13}C$ (0.4 ‰) at these two locations corresponds in magnitude to the observed gradient in the subpolar North Atlantic during the late LIG and translates to the relative influence of SSW versus NSW to the sediment core locations.

In the model, the variations of bottom water $\delta^{13}C$ closely follow the variations in water mass influences (NSW versus NSW), supporting the previous interpretation of the proxies, and the AMOC strength. Consequently, high values of bottom $\delta^{13}C$ corresponding to strong AMOC are associated to a major influence of NSW to the sediment core sites. Conversely, when the AMOC weakens, the bottom water $\delta^{13}C$ at both core locations decreases, revealing, however, two distinct values, suggesting that the southernmost core location (Site U1304) is more sensitive to the influence of SSW than the northernly located MD03-2664.

The spontaneous AMOC variations is found associated to the activation and deactivation of deep convection areas south of Greenland where saline Atlantic surface water penetrates when the sea-ice in this region retreats. This paper underlines that the convection south of Greenland (Irminger and Labrador Seas) is closely related to the overall overturning circulation strength, and that it may be plausible that it has also switched on and off at centennial-timescales during the LIG, reminiscent of the mechanisms invoked for abrupt millennial-scale ocean-climate changes observed during the last glacial cycle.

Paper III: Augustin Kessler, Nathaelle Bouttes, Didier M. Roche, Ulysses S. Ninnemann, and Jerry F. Tjiputra (submitted): *Dynamics of spontaneous (multi) centennial-scale1variations of the Atlantic Meridional Overturning Circulation strength during the Last Interglacial*, Paleoceanography and Paleoclimatology.

In this study, we explore the internal mechanisms and thresholds of the intermediate complexity model iLOVECLIM in simulating spontaneous AMOC variations during the LIG. We performed three additional experiments to that previously described over the LIG in order to differentiate the relative importance of the change in orbital and greenhouse gas forcings, and determine the role of terrestrial vegetation-induced climate feedback on AMOC.

We found that the spontaneous 300 years frequency of the AMOC variations are associated to the changes in orbital forcing and the resulting decline of summer insolation in the high northern latitudes. Two key regions of North Atlantic deep convection are identified as playing a major role in initiating the AMOC increases and declines: (1) the northern Nordic Seas (NNS) and (2) the northwestern North Atlantic (NWNA). These regions are linked through a series of processes involving the atmosphere-ocean-cryosphere system where an early increase in deep convection in region (1) leads to the activation or increase of the deep convection in (2), resulting in the strengthening of the AMOC.

The model seems to exhibit a summer air temperature threshold ($\sim$-4$^{\circ}C$) between the latitude bands 69$^{\circ}N$-80$^{\circ}N$ below which the AMOC switches rapidly to be preferentially simulated at lower state ($\sim$10 Sv). This is associated to the rapid expansion of the sea-ice in both regions (1) and (2) and the transport of more fresh polar water along the Greenland coastline. This study shows that spontaneous variations of the AMOC may have been plausible during the LIG and that the ocean-atmosphere-cryosphere system may also hold enough energy to trigger it under the warm conditions of the LIG.

In short, complex coupled feedbacks in the climate system play a key role in generating spontaneous AMOC variability, but only when boundary conditions are right for them to arise. In this case, they involve large sea ice changes as a crucial component. Future projections suggest that the North Atlantic will likely be free of sea-ice as early as the second half of this century, therefore we suggest that such AMOC variations are very unlikely to occur at the end of the century.

3.1 Main conclusion

Collectively these papers use model analysis together with model-data comparisons to provide a detailed assessment of the coupled ocean physico-chemical dynamics during the LIG. They provide new insights into the physical mechanisms behind proxy ($\delta^{13}C$) variability during this period and its implication for ocean (in)stability during a past period of warm(er) climate. Therefore, based on the results of the three papers outlined above, the main conclusions of this thesis are:

- The warm boundary conditions at 125ka reduces the ocean capacity to store carbon by more than 300 PgC as compared to what it is at 115ka. The Atlantic basin large scale circulation structure is the most impacted with a profound change in

NSW-SSW distribution in the interior ocean. The 125ka simulation results in a reduced standing volume of old deep water (SSW) with high remineralized carbon content, while very little changes occur in the surface primary production.

- This thesis supports the previous interpretation of abrupt bottom water $\delta^{13}C$ variations involving rapid shifts in waster masses influence in the deep ocean during the LIG (*Galaasen et al.*, 2014; *Hodell et al.*, 2009). It shows that (1) it is mechanistically plausible to abruptly modify the bottom water $\delta^{13}C$ via changes in NSW-SSW influence, (2) the strength of the AMOC could be linked to the relative influence of SSW in the North Atlantic.

- The atmosphere-ocean-cryosphere system could enter a regime of nonlinear instability during the LIG, resulting in spontaneous transitions between weak and strong AMOC without external (anomalously applied freshwater) forcing. The key non-linearity may arise, in this case, due to the phase change as convection modulation appears to be tightly coupled to sea ice cover changes. Such sea-ice conditions are very unlikely to occur at the end of the century, when the North Atlantic is expected to be sea-ice free.

3.2 Perspectives and outlook

This section discusses the limitations of the model results presented in this thesis in the context of the recorded LIG climate conditions and potential relevance for future climate.

In general, several aspects of the LIG climate conditions have been substituted with pre-industrial in this study state because of the lack of constraints from past proxy records or due to computational limitations. First, the use of quasi-equilibrium states in Paper I in representing two time slice of the LIG (125ka and 115ka) and of an equilibrium state at 125ka as starting point for the LIG transient simulation in Paper II and III, is unrealistic. It ignores transient forcings and shorter-term variability in the case of Paper I and removes potential effects from reminiscent glacial conditions in Paper II and III. Consequently, internal climate variability in our model simulations likely do not represent that of the past LIG. However, Paper I still provides insight into the baseline changes and distribution of DIC when forced by different LIG orbital configurations, while Paper II and III demonstrate that the climate response to natural transient changes in greenhouse gas and orbital forcings is sufficient to generate large shifts in interior ocean carbon distribution and water mass geometry, thus supporting the previous interpretation of $\delta^{13}C$ proxy. Nevertheless, it remains to be explored how the same model response if different or more realistic initial conditions were to be used.

Secondly, in Paper I, riverine input of nutrients, sea level and atmospheric loads of dust have been set to pre-industrial levels while they are likely to be different during the LIG. For instance, the sea level is suggested to have been 6-9 m above the present levels during the LIG (*Kopp et al.*, 2009). This could have impacted the long term

ocean carbon cycling by altering the production of calcium carbonate ($CaCO_3$) matter from corals and shallow water algae during the early 125ka as compared to that during the cold 115ka when the sea level is suggested to decrease with the Earth system entering the new glaciation (*Frankignoulle et al.*, 1994; *Kleinen et al.*, 2016). Note that the results Paper I highlight very little impact of the changes in hard shell $CaCO_3$ as compared to the soft-tissues remineralization. In addition, we realize that consequent changes could arise from the change in dust load into the atmosphere between 125ka and 115ka, especially by iron-fertilizing the ocean under the cold 115ka boundary conditions, affecting therefore the biological pump (*Ziegler et al.*, 2013). Based on previous studies, an increase of the carbon budget during the colder 115ka can be expected from the addition of more iron-borne dust as compared to 125ka by increasing its surface production of organic matter and consequently more remineralization in the interior ocean.

Finally, the freshwater input from ice sheet melting is the primary source of uncertainties in the model studies from this thesis, so as the extent of the sea-ice edge during the LIG. These remain poorly documented for the LIG and difficult to constrain. The early LIG seems to be more sensitive to strong episodic freshwater inputs as recorded by the IRD pulses during that period (*Galaasen et al.*, 2014), but quantifying their magnitudes and discharge rates remain challenging. Both short-lived freshwater contribution, such as the recorded 8.2-like outburst through the Hudson straight at around 125ka (*Galaasen et al.*, 2014; *Nicholl et al.*, 2012), and longer-term transient melting of the Greenland ice sheet remain relatively poorly understood, so as their implications for altering ventilation rates, interior water mass geometry and bottom-water chemistry. Papers II and III reveal however that even without the contribution of freshwater both on the long and short-term, self sustained variations from complex interactions of the atmosphere-ocean-cryosphere system are sufficient to simulate comparable changes in the ocean carbon dynamic ($\delta^{13}C$) and may be plausible under the LIG.

In the context of the work presented in this thesis, I would recommend for the direction of future research to:

- encourage the implementation additional ocean tracers such as the $\delta^{13}C$ in the latest generation Earth system models. This would benefit the paleoclimate community in constraining past climate variations with more insight into the carbon cycle and ocean circulation, especially if model are capable of resolving higher resolution changes for selected key paleoclimate states and variability.
- lead additional $\delta^{13}C$ model-data comparison over the LIG in order to constrain the first order results of this thesis, but also to perform similar transient experiments over older interglacials that showed bottom water $\delta^{13}C$ abrupt variations (*Galaasen et al.*, 2020). This would narrow to what boundary conditions such abrupt variability may be reproduced and how they may or may not be relevant under the projected future warmer world.
- lead a model inter-comparison project, but instead of using different time-slices of past periods (e.g., *Kageyama et al.* (2018)), performing a set of transient simulations. For this, Earth system models of intermediate complexity (EMIC) could

be used as they are less expensive than ESMs and allow for multi millennial-timescales simulations. Alternatively, ESMs with a reduced resolution could also be considered. This would constrain the results of this thesis over the LIG, and could also give more insight into the climatic impact from such abrupt AMOC fluctuations.

- Increase the available sea ice proxy reconstructions for the LIG, a time period from which very few data are currently available (*Stein et al.*, 2017). The work done in this thesis suggests that, similar as for abrupt climate changes during glacial periods (e.g., *Li and Born* (2019) for a review), sea ice feedbacks may also play a crucial role in ocean circulation and climate variability during interglacials. Sea ice reconstructions from key convection regions could provide a crucial empirical test of this hypothesis.

Chapter 4

Scientific results

Paper I

4.1 Ocean carbon inventory under warmer climate the case of the Last Interglacial

Augustin Kessler, Eirik V. Galaasen, Ulysses S. Ninnemann, and Jerry F. Tjiputra
Climate of the Past, **14**, 1961—1976, 2018. doi:10.5194/cp-14-1961-2018

Clim. Past, 14, 1961–1976, 2018
https://doi.org/10.5194/cp-14-1961-2018

Climate of the Past
Open Access
EGU

Ocean carbon inventory under warmer climate conditions – the case of the Last Interglacial

Augustin Kessler[1], **Eirik Vinje Galaasen**[2], **Ulysses Silas Ninnemann**[2], **and Jerry Tjiputra**[1]

[1]NORCE Norwegian Research Centre, Bjerknes Centre for Climate Research, P.O. Box 22, 5838 Bergen, Norway
[2]Department of Earth Science, University of Bergen and Bjerknes Centre for Climate Research, Bergen, Norway

Correspondence: Augustin Kessler (augustin.kessler@norceresearch.no)

Received: 25 June 2018 – Discussion started: 3 July 2018
Revised: 2 November 2018 – Accepted: 8 November 2018 – Published: 11 December 2018

Abstract. During the Last Interglacial period (LIG), the transition from 125 to 115 ka provides a case study for assessing the response of the carbon system to different levels of high-latitude warmth. Elucidating the mechanisms responsible for interglacial changes in the ocean carbon inventory provides constraints on natural carbon sources and sinks and their climate sensitivity, which are essential for assessing potential future changes. However, the mechanisms leading to modifications of the ocean's carbon budget during this period remain poorly documented and not well understood. Using a state-of-the-art Earth system model, we analyze the changes in oceanic carbon dynamics by comparing two quasi-equilibrium states: the early, warm Eemian (125 ka) versus the cooler, late Eemian (115 ka). We find considerably reduced ocean dissolved inorganic carbon (DIC; − 314.1 PgC) storage in the warm climate state at 125 ka as compared to 115 ka, mainly attributed to changes in the biological pump and ocean DIC disequilibrium components. The biological pump is mainly driven by changes in interior ocean ventilation timescales, but the processes controlling the changes in ocean DIC disequilibrium remain difficult to assess and seem more regionally affected. While the Atlantic bottom-water disequilibrium is affected by the organization of sea-ice-induced southern-sourced water (SSW) and northern-sourced water (NSW), the upper-layer changes remain unexplained. Due to its large size, the Pacific accounts for the largest DIC loss, approximately 57 % of the global decrease. This is largely associated with better ventilation of the interior Pacific water mass. However, the largest simulated DIC differences per unit volume are found in the SSWs of the Atlantic. Our study shows that the deep-water geometry and ventilation in the South Atlantic are altered between the two climate states where warmer climatic conditions cause SSWs to retreat southward and NSWs to extent further south. This process is mainly responsible for the simulated DIC reduction by restricting the extent of DIC-rich SSW, thereby reducing the storage of biological remineralized carbon at depth.

1 Introduction

The Last Interglacial (LIG, or Eemian) is composed of a warm onset around 125 ka characterized by warmer temperature at high latitudes relative to the present and a progressive cooling toward 115 ka when the last glaciation initiated (Otto-Bliesner et al., 2006; Masson-Delmotte et al., 2010). Evidence from land, ice, and ocean records identify the former as the period with the most intense global warming during the last 200 000 years (Turney and Jones, 2010; Dorthe Dahl-Jensen et al., 2013; Capron et al., 2014) mainly due to changes in the orbital configurations. If anthropogenic greenhouse gas emissions continue unabated, a climatically anomalously warm state is expected to occur in the near future with a warming by the end of this century that may be equivalent to the high-latitude reconstructed temperature for the LIG (Otto-Bliesner et al., 2013). The changes in the warm Eemian period may therefore be considered an analog for a future warmer climate.

Few model-based studies examine the carbon cycle dynamics for the LIG period with a particular focus on the ability of models to simulate the transient changes in atmospheric CO_2 concentration, which remains relatively stable around 270–280 ppm without displaying any

trends (Lourantou et al., 2010; Schneider et al., 2013). Most of these studies provide a better understanding of the land carbon budget, particularly highlighting the importance of temperature changes on the land vegetation and slow processes of CO_2 change such as peatland carbon dynamics and $CaCO_3$ shallow-water accumulation (Schurgers et al., 2006; Kleinen et al., 2016; Brovkin et al., 2016). Although there are numerous studies that have analyzed the role of the ocean carbon cycle in regulating the atmospheric CO_2, especially for the interglacial-glacial transition period (Ridgwell, 2001; Sigman and Boyle, 2000; Menviel et al., 2012), to the authors' knowledge there is no study that investigate in details changes in marine carbon and nutrient cycling during the Eemian period of the LIG (125–115 ka).

With respect to changes in large-scale ocean circulation, reconstructions indicate that deep Atlantic circulation patterns and water mass geometries likely change over this interval. While mid-depth ventilation of northern-sourced waters (NSWs) is maintained in the North Atlantic by millennial-scale sustained North Atlantic Deep Water formation throughout the LIG (McManus et al., 2002; Mokeddem et al., 2014), southern-sourced waters (SSWs) expanded at depth toward 115 ka (Govin et al., 2009). In addition to large-scale circulation changes, temperature-induced changes in carbon solubility pumps and biological production are expected to alter the ocean carbon budget, in particular in the interior ocean. Other changes such as sea ice extent and ocean ventilation could also affect ocean carbon sequestration rate during the LIG. Elucidating the mechanisms responsible for changes in the ocean carbon distribution and inventory is of interest as it provides past constraints and context for evaluating the response of natural carbon sources and sinks to future climate change. This study aims to fill this knowledge gap by analyzing and comparing, in terms of ocean carbon dynamic, two opposite states of the LIG: the early and warm Eemian onset (125 ka) versus the cooler and late Eemian (115 ka). Using a state-of-the-art Earth system model, our study addresses the regional differences in the ocean carbon storage and the underlying mechanisms.

The paper is organized as follows: in Sect. 2, we describe the model, the experiment design, and the terms and metrics used to quantify the differences in carbon dynamics during the two periods. Section 3 presents the results of the model simulations, while discussions and comparison with previous studies are presented in Sect. 4. Finally, the study is summarized in Sect. 5.

2 Method

2.1 Model description

The present study uses output of an updated version of the Norwegian Earth System Model (NorESM1-ME), which has recently been further developed to efficiently perform multi-millennial and ensemble simulations (Bentsen et al., 2013; Luo et al., 2018; Guo et al., 2018). This model includes an isopycnal-coordinate ocean general circulation model based on the Miami Isopycnic Coordinate Ocean Model (MICOM; Bleck et al., 1992) and a biogeochemical ocean module adapted from the Hamburg Oceanic Carbon Cycle (HAMOCC5) model (Maier-Reimer, 1993; Maier-Reimer et al., 2005; Tjiputra et al., 2013). The inorganic seawater carbon chemistry in HAMOCC5 includes prognostic partial pressure of CO_2 (pCO_2) according to the Ocean Carbon-Cycle Model Intercomparison Project (OCMIP) protocols. The pCO_2 is computed as a function of temperature, salinity, dissolved inorganic carbon (DIC), total alkalinity (TALK), and pressure. This adapted version of HAMOCC5 does not include prognostic weathering fluxes but does employ a 12-layer sediment model following Heinze et al. (1999), which is particularly relevant for long-term transient simulations. The horizontal resolution of the land and atmospheric components is approximately 2°, while the ocean and ice components have higher resolutions of approximately 1°. In the vertical, the ocean model adopts 53 isopycnal layers.

The land component in NorESM (CLM4, Community Land Model version 4) is based on version 4 of the CLM family (Lawrence et al., 2012a). The land surface is sub-gridded into three sub-gridded entities: land units, columns, and plant functional types (PFTs). These sub-gridded cells are used to represent large-scale patterns of the landscape, variability in the soil and snow state variables, and the exchanges between land surface and atmosphere, respectively. Each of the sub-grid entities has its own prognostic variables, is independent, and experiences the same atmospheric forcing. Each cell is averaged and weighted with its fractional area.

The marine ecosystem is based on a nutrient–phytoplankton–zooplankton–detritus (NPZD) model that includes dissolved organic carbon (DOC). The inorganic nutrients consist of three macronutrients (phosphate, nitrate, and silicate) and one micronutrient (dissolved iron). A constant Redfield ratio is adopted in the model as $P:C:N:\Delta O_2 = 1:122:16:-172$. The phytoplankton growth rate is expressed as a function of temperature, light (Smith, 1936; Eppley, 1972), phosphate, nitrate, and dissolved iron availability, and its loss is regulated by an exudation and mortality rate, in addition to zooplankton grazing. The penetration of light decreases with depth following an exponential function, which responds to a gradual extinction factor formulated as a function of water depth and chlorophyll concentration (Maier-Reimer et al., 2005). The model prescribes a global constant vertical sinking speed of particles produced in the euphotic zone (above 100 m depth). The particulate organic carbon (POC), which comprises dead phytoplankton and zooplankton, sinks through the water column at a speed of $5\,m\,day^{-1}$ and is remineralized at a constant rate of $0.02\ day^{-1}$ when oxygen is available. Other particles such as opal shells and particulate inorganic carbon (PIC) sink at a speed of 60 and $30\,m\,day^{-1}$, respectively. Particulates that reach the seafloor

without being remineralized interact chemically with the sediment pore water via bioturbation and vertical mixing and advection within the sediment layers. In the model, the air–sea gas exchange of CO_2 and O_2 only occurs between the ocean surface and the atmosphere in ice-free regions and is computed according to the following three components (Wanninkhof, 1992): the gas solubility in seawater, which is computed as a function of surface salinity and temperature according to Weiss (1970, 1974); the gas transfer velocity, which is proportional to the square of the surface wind speed and is computed as a function of the Schmidt number; and finally the air–sea gradient of gas partial pressures. To better elucidate various biogeochemical processes on the carbon cycle, the model is updated to also include preformed O_2, TALK, and PO_4 tracers in the biogeochemical module. At the surface, these preformed tracers are set to their non-preformed value and are advected passively by the ocean circulation in the interior without any other sources and sinks. Finally, in order to provide information of the water mass ages since its last contact with the atmosphere, an idealized age tracer is implemented and simulated in the NorESM model. Hence, the age tracer is set to zero for all water masses at the ocean surface and subsequently transported and mixed passively with circulation in the ocean interior and integrated with the model time step. This tracer is also used to estimate the ventilation rate of different interior water masses.

2.2 Experiment setup

Two equilibrium experiments are performed over the Eemian (model data available at https://doi.org/10.11582/2018.00038; Kessler, 2018), one near the onset (warmer than today, 125 ka) and one at the end (colder, 115 ka) of the Last Interglacial. Both experimental configurations follow the standard protocols of the third phase of the Paleoclimate Modelling Intercomparison Project (PMIP3; https://pmip3.lsce.ipsl.fr/, last access: 5 December 2018), with a fixed vegetation coverage from the preindustrial boundary conditions. The only differences from the preindustrial configurations are the orbital parameters and the greenhouse gases concentrations (CO_2, CH_4, N_2O). For the experiment at 125 ka (115 ka), the atmospheric CO_2, CH_4, and N_2O levels are prescribed to be 276 ppmv (273 ppmv), 640 ppb (472 ppb), and 263 ppb (251 ppb), respectively. The two experiments are branched off from 1000 years of spin-up with a preindustrial setup and forced with their respective interglacial boundary conditions for 4000 simulation years.

In the last 50 years of Eemian forcing simulations the ocean is close to equilibrium. Only small drifts remain, mainly in the Pacific basin where the equilibrium is still not fully established. Therefore, the global ocean DIC and TALK slightly decrease in the experiment at 125 ka (115 ka) by approximately $-0.15\,\mathrm{PgC\,yr^{-1}}$ ($-0.06\,\mathrm{PgC\,yr^{-1}}$) and $-0.01\,\mathrm{Pmol\,yr^{-1}}$ ($-0.01\,\mathrm{Pmol\,yr^{-1}}$), respectively. However, these drifts are small compared to the absolute ocean budget in DIC (37391 and 37705 PgC) and TALK (3291 and 3303 Pmol) for the 125 and 115 ka experiments, respectively. The differences in the pCO_2 and TALK budget are small between the two experiments. Such changes would affect the DIC budget by about 32 PgC. The CO_2 flux is relatively constant and depicts the ocean as a weak source to the atmosphere with an outgassing of 0.12 ± 0.06 at 115 ka and $0.15 \pm 0.06\,\mathrm{PgC\,yr^{-1}}$ at 125 ka. In addition, the difference in sedimentation rates between the two experiments ($\sim 6.10^{-4}$ PgC) appears to be negligible compared to the difference in DIC budget.

2.3 DIC decomposition

In order to analyze the oceanic carbon cycle, dissolved inorganic carbon (DIC) is decomposed into its preformed and biological components (Eq. 1), following Bernadello et al. (2014):

$$\mathrm{DIC^{tot}} = \mathrm{DIC^{pre}} + \mathrm{DIC^{bio}}. \quad (1)$$

The preformed component of DIC ($\mathrm{DIC^{pre}}$) comprises saturated and disequilibrium parts (Eq. 2).

$$\mathrm{DIC^{pre}} = \mathrm{DIC^{sat}} + \mathrm{DIC^{dis}}, \quad (2)$$

where the DIC at saturation ($\mathrm{DIC^{sat}}$) describes the DIC concentration when the water parcel is in full equilibrium with the atmospheric CO_2 when it is last in contact with the surface. In our model, changes in DIC^{sat} are mainly affected by changes in preformed TALK. We compute this variable offline with the inorganic carbon chemistry program CO2SYS developed in Matlab (van Heuven et al., 2011), including other parameters such as the model output of preformed alkalinity ($\mathrm{TALK^{pre}}$), preformed phosphate ($\mathrm{PO_4^{pre}}$), surface silicate, salinity, and temperature. In addition, the atmospheric CO_2 concentration from each experiment is used. To complete the CO2SYS input, we applied the dissociation constants K1 and K2 introduced by Mehrbach et al. (1973) and refitted by Dickson and Millero (1987). The disequilibrium part of DIC ($\mathrm{DIC^{dis}}$) measures the disequilibrium state of the surface water with respect to the atmosphere. This parameter is computed from the $\mathrm{DIC^{tot}}$ (output), from which the biological and saturated DIC components ($\mathrm{DIC^{bio}}$ and $\mathrm{DIC^{sat}}$) are subtracted. Therefore, all components are included in its calculation. A negative $\mathrm{DIC^{dis}}$ occurs when the water parcel sinks into the ocean interior before a full equilibration with the atmosphere is obtained, which leads to an undersaturation of the water parcel. This undersaturation can also be reinforced by biological CO_2 consumption at the surface, which tends to increase the timescale needed for the water parcel to equilibrate. However, a positive $\mathrm{DIC^{dis}}$ translates into a supersaturation. The latter occurs when deep waters, which

contain high concentration of DIC because of remineralization processes, upwell or mix vertically with the surface waters (Follows and Williams, 2004). Both DIC^{dis} and DIC^{sat} are transported by ocean circulation into the interior ocean.

The biological component of DIC comprises (1) the interior remineralization of organic matter (expressed in carbon), which is produced in the euphotic layer via photosynthesis (also referred to as soft-tissue pump), and (2) the remineralization of planktonic calcium carbonate shells (expressed in carbon; calcium carbonate pump). These two remineralization components are added to form the biological component of DIC, as shown in Eq. (3).

$$DIC^{bio} = DIC^{soft} + DIC^{carb} \quad (3)$$

The remineralization of soft tissues (hereafter DIC^{soft}) contributes via phosphate (PO_4) remineralization through a carbon phosphorus stoichiometric ratio $r_{C:P} = 122$. This component is calculated from the difference between the total and the preformed PO_4 according to

$$DIC^{soft} = r_{C:P}({PO_4}^{tot} - {PO_4}^{pre}). \quad (4)$$

The carbonate pump contributes through the dissolution of $CaCO_3$ hard shells, calculated as difference between the total and the preformed alkalinity and PO_4 following

$$DIC^{carb} = 0.5[{TALK}^{tot} - {TALK}^{pre} + r_{N:P}({PO_4}^{tot} - {PO_4}^{pre})], \quad (5)$$

where $r_{N:P} = 16$ is the Redfield ratio adopted by the model and the phosphate term accounts for the alkalinity changes owing to the soft-tissue pump.

In our analysis, we show differences between the warmer 125 ka and the colder 115 ka experiments. We therefore use the delta notations ΔDIC^{tot}, ΔDIC^{sat}, ΔDIC^{soft}, ΔDIC^{carb}, and ΔDIC^{dis} to refer to changes between the warmer and the colder periods.

2.4 Water mass analysis

In order to identify water mass sources, we apply the "PO" tracer as defined by Broecker (1974). It is computed using phosphate and oxygen fields following

$$PO = O_2 + r_{O:P}PO_4, \quad (6)$$

where $r_{O:P} = 172$ is the phosphorus-to-oxygen stoichiometric ratio used in the model. This tracer is presumed to be nearly constant for a specific water mass. It is based on the principle that phosphate is released while oxygen is used during remineralization, and vice versa during biological production. The distinction of water masses using PO is useful for contrasting water masses with very different surface PO values. Here, we mainly use PO to identify NSW and SSW masses in the deep ocean below 1000 m depth characterized by low and high PO values, respectively.

3 Results

Section 3.1 describes the sea surface temperature and sea ice changes, while changes in water mass properties are discussed in Sect. 3.2. The near-surface changes that particularly influence the biological pump are addressed in Sect. 3.3, and global to regional oceanic DIC storage changes are presented in Sect. 3.4. The analysis is performed over the average of the last 50 years of the simulations. In addition, the global ocean is divided into three main basins: Atlantic, Indian, and Pacific.

3.1 Sea surface temperature and sea ice

Our model simulates a global and annual increase of sea surface temperature (SST; +0.27 °C) at 125 ka relative to the 115 ka experiment. This warming is mainly simulated at high latitudes (Fig. 1a–d) where higher SSTs are simulated throughout the year in the Southern Ocean (SO), south of Greenland, the Norwegian Sea, and the northern part of the Pacific Ocean. This persistent warming at 125 ka induces the sea ice to melt (Fig. 1, green and purple lines). Consequently, in the areas where sea ice extent is reduced, there is more air–sea gas exchange and an increase in mixed-layer depth (MLD; Fig. 1, black lines in the Southern Ocean). In the Labrador Sea the mixed layer depth at 125 ka is deeper by more than 100 m than at 115 ka. This is due to higher salinity simulated in this region at 125 ka. At lower latitudes, the SSTs vary more spatially and seasonally. For example, in some parts of the Atlantic Ocean (North Atlantic Drift, the equatorial region, and some sections of the subantarctic near the 45° S band) cooler SSTs are simulated over several seasons ($\Delta SST < 0$, Fig. 1a–b). While the North Atlantic drift depicts cooler SSTs during boreal winter and spring (Fig. 1a–b), colder SSTs last until the boreal summer in the equatorial region of the Atlantic Ocean (Fig. 1a–c). The 45° S latitude band remains cooler over the four seasons. Here, the MLD seems to be more controlled by changes in salinity instead of temperature distribution.

We note that relative to the preindustrial, based on proxy (Hoffman et al., 2017), our model simulates consistent spatial feature of annual SST anomalies at 125 ka. It simulates, among other things, (i) strongest warming at high latitudes, specifically in parts of the Southern Ocean; (ii) weak cooling at low latitudes; (iii) cooler SST in most of the Indian Ocean; and (iv) a warmer eastern North Pacific. Nevertheless, the amplitude of SST warming and cooling at specific sites tends to be weaker in our model. This feature appears to be common in other global models and could be attributed to their low spatial resolutions (Hoffman et al., 2017).

3.2 Water mass properties

In order to analyze the water mass properties, it is useful to examine the changes in the overturning circulation. Figure 2

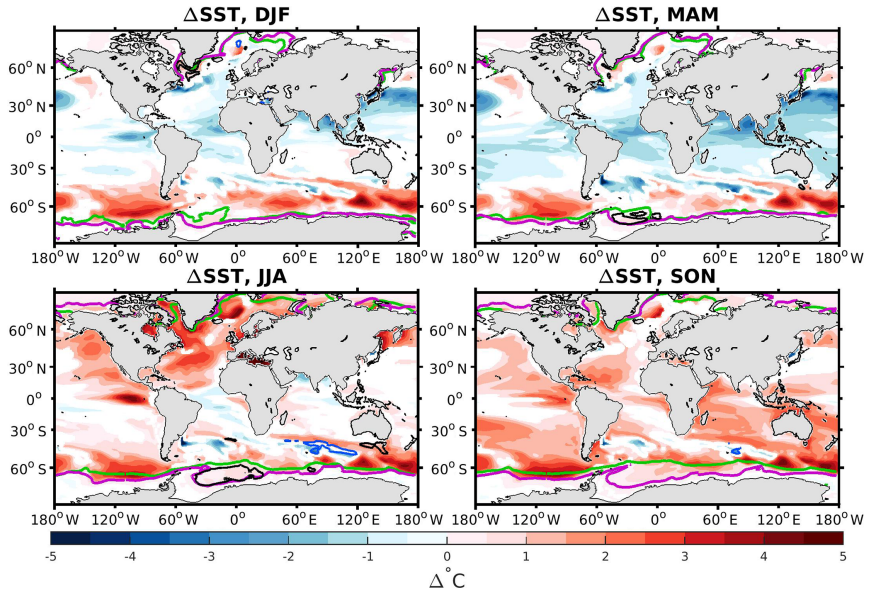

Figure 1. Difference in sea surface temperature (ΔSST) between 125 and 115 ka. Only significant differences (i.e., with absolute value greater than the interannual standard deviation over the last 50 years in both 125 and 115 ka) are shown. The green and purple lines correspond to 50 % sea ice extent at 115 and 125 ka, respectively. The black (blue) thick lines depict regions affected by a deepening (shallowing) of the mixed-layer depth (with difference greater than 100 m depth) at 125 ka compared to 115 ka.

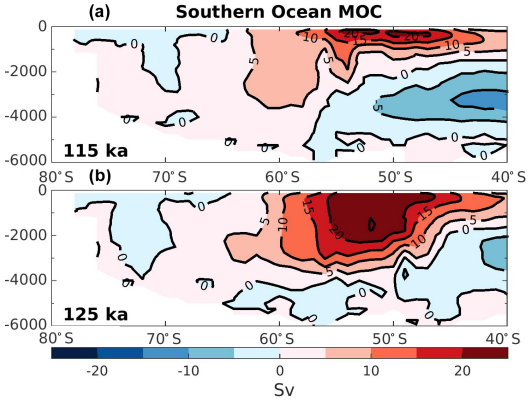

Figure 2. Southern Ocean overturning stream function in Sverdrup (Sv) for the experiment at 115 ka **(a)** and 125 ka **(b)**. Red colors represent water masses moving clockwise, while blue colors represent water masses moving counterclockwise.

shows the global overturning stream function in the Southern Ocean for both experiments. The Antarctic circumpolar current is simulated stronger and deeper at 125 ka compared to 115 ka (Fig. 2). This strengthening mainly occurs in the Pacific section of the Southern Ocean (near 50° S), suggesting an increase of the ventilation rate of the intermediate waters formed in this region. The Atlantic section of the Southern Ocean remains weakly modified. Indeed, using the same model simulations as the present study, Luo et al. (2018, Supplement Fig. S8) show that the surface wind speed in the eastern and western South Atlantic are relatively similar at 125 and 115 ka. In addition, they also show that the simulated Atlantic Meridional Overturning Circulation (AMOC) at 125 ka is as vigorous as at 115 ka but deepen by about 300 m depth. This suggests that the mid-depth and bottom water in the North Atlantic Ocean should be better ventilated at 125 ka than at 115 ka.

These changes in the overturning circulation affect the water mass age tracer. Analyzing this parameter allows us to examine the interior ocean ventilation rate. A reduction in water mass age translates to a faster ventilation rate and vice versa for an increase in age. The differences in water mass age between 125 and 115 ka are presented in Fig. 3, depicting the zonally averaged sections for each ocean basin. The water mass ages in the Atlantic and the Indian oceans show similar patterns, with mean older water masses in the upper layers at 125 ka (roughly +100 years) and younger water masses below 1000 m depth (as much as 500 years younger). This is consistent with a deeper and slightly stronger AMOC at

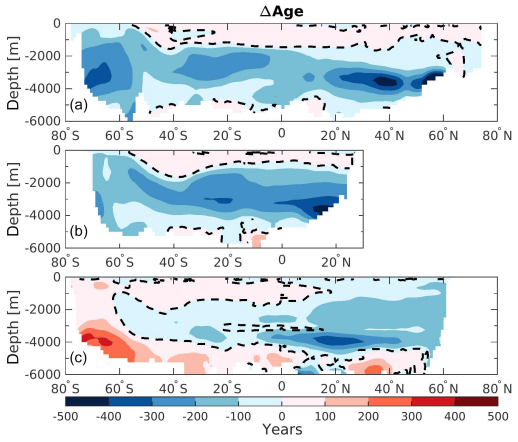

Figure 3. Zonally averaged section of the difference in water mass age (ΔAge) between 125 and 115 ka in **(a)** the Atlantic Ocean, **(b)** the Indian Ocean, and **(c)** the Pacific Ocean. The dashed lines display ΔAge = 0.

125 ka as shown in Luo et al. (2018). The Southern Ocean (south of 50° S) contains younger water masses throughout the entire water column in both basins at 125 ka, translating to a stronger ventilation rate. This is likely due to changes in the distribution of SSW and NSW. Figure 4 show that there is a clear distinction between interior water mass structure in the Atlantic basin between 115 ka (Fig. 4a) and 125 ka (Fig. 4c). It shows that below 2000 m depth the SSW retreats further southward at 125 ka relative to 115 ka in the Atlantic basin. This confinement in SSW is induced by the change in the Antarctic sea ice cover (Fig. 1), as explained by Ferrari et al. (2014). However, the model also simulates a modification in SSW density ($-0.2\,\mathrm{kg\,m^{-3}}$ at 125 ka compared to 115 ka; Fig. 4a, c). This reduction in water density is mainly driven by the input of low-salinity freshwater from the melting of the Antarctic sea ice and may have an additional impact on determining the Atlantic distributions of NSW and SSW. As a result of sea ice retreat, the winter mixed layer depth in this area increases, resulting in younger water mass age in the Southern Ocean. Near the surface (∼ 800 m depth) the SSW seems to enter further north in the Atlantic basin at 125 ka (Fig. 4c) relative to 115 ka (Fig. 4a).

While such large redistributions of northern- and southern-origin deep waters only occur in the Atlantic, these changes also influence water properties in the Indian Ocean due to the "downstream" advection of younger deep water into the interior during the warmest period (125 ka – Fig. 3b). In addition to simple advection of younger water northward in the Indian basin, the residence time of the Indian Ocean's deep water must also decrease since the ventilation ages decrease northward at depth. By contrast, in the Pacific Ocean, the zonally averaged bottom-water mass ages are simulated to be older at 125 ka (Fig. 3c). However, this basin can be divided between the western and eastern side. While the western side is also influenced by the younger water masses created in the Atlantic Ocean, the eastern side waters of the basin are simulated to be older at 125 ka by as much as 300 years. These older water masses are created in the Pacific SO and may be affected by a flattening of the isopycnals south of 60° S at 125 ka (Fig. 4d, gray lines). This flattening of the isopycnals is influenced by both sea ice melting and higher SSTs, and suggests stronger stratification and a weaker subduction rate. In addition, the SSW boundary (Fig. 4b, d; light purple dashed lines) seems to be slightly poleward at 125 ka (∼ 60° S) compared to 115 ka (∼ 58° S). This may suggest that more surface water originating from the subtropical gyre (more depleted in phosphate) enters the Pacific section of the Southern Ocean. Finally, the Pacific intermediate waters are simulated as younger at 125 ka when compared to 115 ka (Fig. 3c), which is consistent with the strengthening of the upper cell of the overturning circulation previously mentioned for this region.

The southern-sourced waters are particularly affected in terms of geometry distribution. We therefore divide the changes from these SSWs into the three basins. Table 1 summarizes the changes occurring below 1000 m depth in the SSWs in terms of volume, DIC, and water mass age for each basin and reveals the Atlantic as the most affected area under warmer climate conditions. The relative difference in all those three characteristics (ΔV_{SSW}, ΔAge_{SSW}, and ΔDIC_{SSW}) between 125 and 115 ka is the greatest in the Atlantic (−37 %, −262 years, and $-0.92\,\mathrm{g\,C\,m^{-3}}$). This demonstrates that the ventilation mechanism in the Atlantic sector of the SO is likely to be more sensitive (than in other basins) to climate change.

In response to the different forcings between 125 and 115 ka, significant changes are simulated in deep-water ventilation rates and water mass distribution in the three basins. While the responses in the Atlantic and Indian oceans have some similarity (better deep-water ventilation), the Atlantic basin seems to be the most sensitive and also simulates water mass geometry changes. However, the ventilation rate in the Pacific Ocean depicts an opposite sign of change to that of the Atlantic and Indian oceans. In the next section we discuss how these modification impact the near-surface productivity in our model.

3.3 Near-surface productivity

Figure 5 shows the differences in carbon export production (EPC) and phosphate (PO_4) at the surface of the ocean between 125 and 115 ka. When comparing the 125 and 115 ka experiments, our model simulates two major features characterized by (i) an increase in EPC in the equatorial region of the Atlantic Ocean (Fig. 5a, turquoise rectangle) and (ii) a reduction in EPC of similar magnitude in the equatorial re-

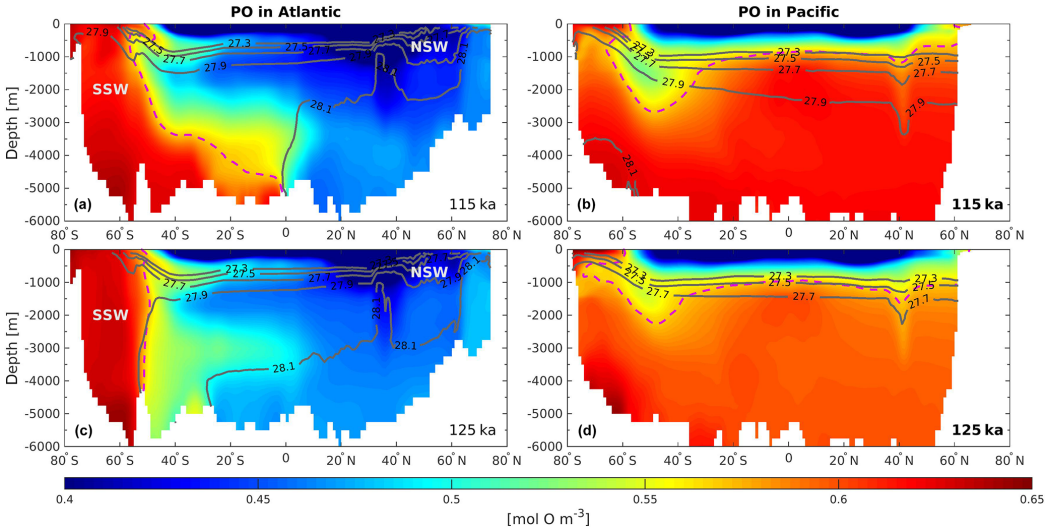

Figure 4. Zonally averaged section of PO as defined by Broecker (1974) in **(a, c)** the Atlantic Ocean at 115 and 125 ka, respectively, and **(b, d)** the Pacific Ocean at 115 and 125 ka, respectively. The light purple dashed lines delimit the water influenced by the SSW from water influenced by the NSW. The dark gray solid lines depict the neutral density (units: kg m^{-3}).

Table 1. Difference in southern-sourced water (Δ_{SSW}) in the global ocean and for each basin. Row 1 shows the volume (V_{SSW}) according to our PO $\geq$ 0.57 mol O m^{-3} criteria. Rows 2 and 3 summarizes the DIC and water mass age mean value for the two period of study. The changes relative to 115 ka are given as a percentage in parenthesis.

	Global	Atlantic	Indian	Pacific
ΔV_{SSW} [10^6 km^3]	−3.43 (1 %)	−18.91 (37 %)	+9.76 (8 %)	+5.72 (1 %)
ΔDIC_{SSW} [gC m^{-3}]	−0.34 (1.2 %)	−0.92 (3.3 %)	−0.61 (2.1 %)	−0.36 (1.2 %)
ΔAge_{SSW} [yr]	−108 (9.3 %)	−262 (78.2 %)	−152 (29.0 %)	−39 (3.0 %)

gion of the Pacific Ocean (Fig. 5a, purple rectangle). Although there are changes in surface wind speeds and vertical mass fluxes (not shown here) in the equatorial regions, they do not consistently explain the simulated changes in export production (i.e., stronger wind and upwelling in the eastern equatorial Pacific at 125 ka compared to 115 ka, where a decrease in export production is simulated; in parts of the equatorial Atlantic some increase in export production may be related to the simulated stronger upwelling at 125 ka). However, nutrient changes in the Atlantic and Pacific sections of the Southern Ocean are consistent with the changes in export production, and therefore we suggest the following mechanism. In the Atlantic Ocean, the subantarctic water (45° S latitude band) corresponds to the southern-sourced intermediate water formation in the model. This water mass sinks and reemerges along the Equator (Fig. 5, turquoise rectangles). This pattern expected from models and modern observations shows that the intermediate and mode waters formed at high southern latitudes feed the subtropical thermocline and act as a predominant source of nutrients important for sustaining low-latitude biological productivity (Gu and Philander, 1997; Sarmiento et al., 2004b). We acknowledge that there is uncertainty in the complex pathways of the subantarctic water masses toward the Equator simulated in the model. Nevertheless, due to higher preformed and remineralized phosphate in the subantarctic water sinking region, more PO_4 is advected through this "ocean tunnel" to the Equator and therefore leads to an increase in EPC (Fig. 5a, turquoise rectangle). A similar ocean tunnel (Fig. 5, purple rectangle) connects the high and low latitudes in the Pacific Ocean but results in the opposite sign of change. Here, as pointed out in Sect. 3.2, more subtropical waters seem to enter the Pacific Southern Ocean at 125 ka than at 115 ka. These waters are depleted in phosphate compared to southern-sourced waters. As a result, less phosphate is subducted toward the equatorial Pacific (Fig. 5b, purple rectangle), leading to a reduction in the EPC near the equatorial upwelling (Fig. 5a, purple rectangle).

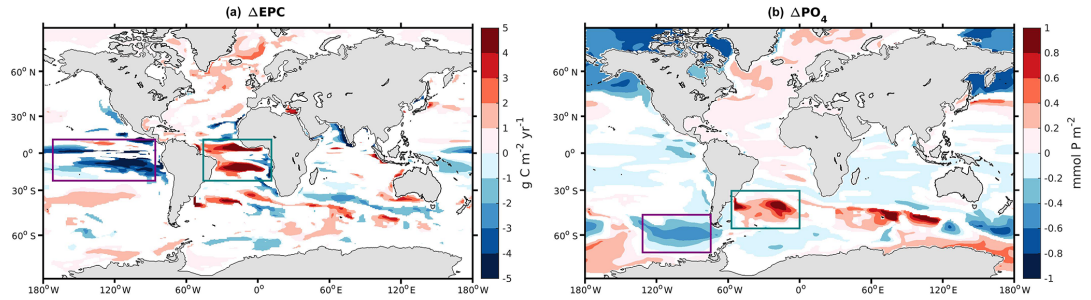

Figure 5. Difference in **(a)** export production of carbon at 100 m depth (ΔEPC) and **(b)** phosphate at the surface (ΔPO_4) between 125 and 115 ka. When the absolute value of the difference is below the standard deviation over the last 50 years at 125 and 115 ka, the value returns a NaN. Purple and turquoise rectangles highlight the two "ocean tunnels" linking the sinking/upwelling regions of southern-sourced intermediate waters in our model.

There are no significant changes in the biological activity in the Indian Ocean or the remaining Southern Ocean. Only a weaker carbon export at 125 ka relative to 115 ka is simulated around 40° S and the Arabian Sea.

Thus, the simulations reveal that changes in Southern Hemisphere thermocline ventilation regions modulate basin scale productivity and export production even within an interglacial period with modest changes in external forcing. This result is broadly consistent with previous studies suggesting that the upper limb of the biogeochemical divide is critical for setting biological export production and is sensitive to climate changes (Sarmiento et al., 2004a; Marinov et al., 2006; Moore et al., 2018). Despite zonally homogeneous forcing we find a basinally heterogeneous response both in subantarctic ventilation and in low-latitude productivity which is similar to, albeit more extreme than, the basin specific response simulated for future warming and stratification (Moore et al., 2018).

These changes in surface physical and biological activities could also have implications for the exchanges of carbon between near-surface and interior water masses, and therefore the interior carbon budget. In the next section, ventilation changes at 125 ka are compared to 115 ka by analyzing the simulated water mass properties.

3.4 Global and regional carbon budgets

Figure 6 shows the difference in the carbon inventory vertical profiles between 125 and 115 ka as simulated by our model. The changes in DIC^{tot}, DIC^{sat}, DIC^{soft}, DIC^{carb}, and DIC^{dis} are averaged over a 500 m depth interval. The global amount of DIC^{tot} is −314.1 PgC in the ocean under the warmer conditions (Fig. 6a, gray ΔDIC^{tot}). Since the atmospheric CO_2 is kept constant in each experiment, this carbon loss at 125 ka compared to 115 ka is implicitly assumed to be balanced out by the changes in the land carbon reservoir. Here, the Atlantic Ocean accounts for 15 % (−49.1 PgC) of that global decrease, while the Indian and the Pacific basins contribute 28 % (−87.2 PgC) and 57 % (−179.0 PgC), respectively. Only in the near-surface layers does the model simulate a positive ΔDIC^{tot}, which translates to higher surface DIC concentration at 125 ka relative to 115 ka. Most of the ocean interior has lower DIC concentration at 125 ka, with the strongest difference in ΔDIC^{tot} simulated between 2000 and 3000 m depths for each basin, except for the Atlantic (Fig. 6b–d). The soft-tissue pump and the disequilibrium effect are the main contributors for the reduced carbon inventory depicted at 125 ka at the global scale (Fig. 6a, green and purple bars) – each accounting for a third of the total −314.1 PgC decrease. Similarly, ΔDIC^{tot} in the Atlantic basin is also predominantly controlled by the biological pump, i.e., the soft-tissue plus carbonate pump throughout the entire water column with a decrease at depth and an increase in the near-surface (Fig. 6b). Except for the upper ocean, the contribution from the saturation component related to temperature and salinity change is generally negligible.

The ΔDIC^{tot} of the Indian basin also depicts a strong reduction at 125 ka relative to 115 ka. Here the soft-tissue and saturation components simulate the strongest decrease (Fig. 6c, green and blue bars). In addition, near-surface changes in ΔDIC^{tot} are controlled by the changes in ΔDIC^{sat}. Similarly, the near-surface layer of the Pacific Ocean is also controlled by the changes in the saturation component (Fig. 6d), simulating a positive difference of about +18 PgC. Changes in the deeper layers are mainly attributed to the disequilibrium effect and the soft-tissue pump, accounting for a decrease of −83.6 and −44.0 PgC at 125 ka relative to 115 ka, respectively. However, the saturation component also has a considerable influence on the carbon storage with persistent negative ΔDIC^{sat} throughout the water column.

In order to address the regional changes, we analyze the differences in each DIC components further by calculating

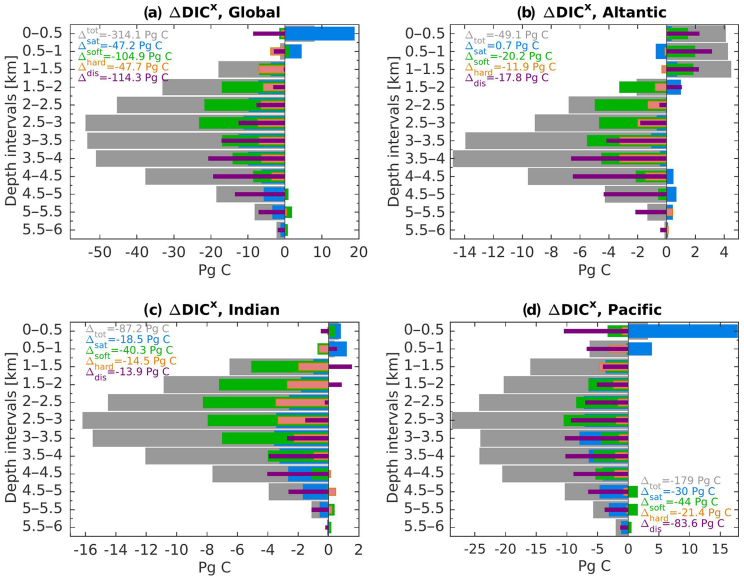

Figure 6. DIC differences between 125 and 115 ka (ΔDIC^x) in **(a)** the global ocean and the **(b)** Atlantic, **(c)** Indian, and **(d)** Pacific basins. The ΔDIC^x is averaged over a 500 m depth interval where "x" refers to the different components of the DIC. The DIC^{tot} is represented by the gray bars and is decomposed into its four components: ΔDIC^{sat} (blue), ΔDIC^{soft} (green), ΔDIC^{carb} (orange), and ΔDIC^{dis} (purple). The sum throughout the water column of each components is given by the legend.

the zonally averaged values in each basin. Figures 7, 8, and 9 depict these differences for the Atlantic, Indian, and Pacific basins, respectively. As shown in Fig. 6b, the carbon inventory of the Atlantic is reduced mainly below 1500 m depth. Here the Southern Hemisphere is the most affected region, which depicts the strongest differences in ΔDIC^{tot} (Fig. 7a, blue shading). This pattern corresponds well to the changes in soft-tissue pump (Fig. 7b). Near the surface, higher carbon export (Fig. 5a) increases the remineralization of organic matter, leading to higher DIC concentration at 125 ka. At depth, the slightly deeper AMOC at 125 ka (compared to 115 ka), leads to better-ventilated mid-depth to bottom waters in the Northern Hemisphere, leading to less remineralized organic matter by reducing the water mass age. This is reflected by the negative ΔDIC^{soft} and ΔDIC^{carb}, translating to a less effective soft-tissue and carbonate pump at 125 ka. Positive changes in ΔDIC^{tot} in near-surface waters and bottom water at 20° N also arise from the soft-tissue and carbonate signal due to the increase of the alkalinity (not shown here) and slightly older water masses along the African coast. The bottom waters in the Southern Hemisphere are mainly controlled by a stronger disequilibrium effect, i.e., negative change in comparison to 115 ka. This change in disequilibrium is due to the sea-ice-induced retreat of the SSW and the inflow of more NSW between 50° S and the Equator at 125 ka. The NSW mass, formed in the North Atlantic, is generally more subject to biological production during its near-surface northward transport before sinking into the interior than the SSW (Duteil et al., 2012). The biological production consumes DIC during photosynthesis and pushes the water mass further out of the equilibrium with the atmospheric CO_2, inducing ΔDIC^{dis} to be more negative. The negative values of ΔDIC^{dis} are conserved when the water parcel flows southward into the deep ocean. For this reason, the regions that are no longer influenced by SSW at 125 ka depict a negative ΔDIC^{dis} (Fig. 7d). However, the upper layers of the Atlantic Ocean are mostly simulated with higher DIC^{dis} (positive ΔDIC^{dis}, or less disequilibrium at 125 ka). This could be induced by more SSW (less disequilibrated than NSW) entering the Atlantic basin further north near the surface as Fig. 4c suggests. Finally, the loss of carbon in the Southern Ocean is shown to be mainly attributable to a decrease of the saturation component at 125 ka. This decrease is mainly attributed to lower $TALK^{pre}$ (not shown here), possibly provoked by the melting of the sea ice.

The DIC storage in the Indian Ocean generally shows a decrease at 125 ka, with the strongest changes occurring at depth north of 30° S (Fig. 8a, dark blue shading). Positive ΔDIC^{tot} are nevertheless simulated in the region that may correspond to the Antarctic Intermediate Water (AAIW) (Fig. 8a, red shading). Similar to the Atlantic basin, the pattern of the soft-tissue pump changes corresponds to the

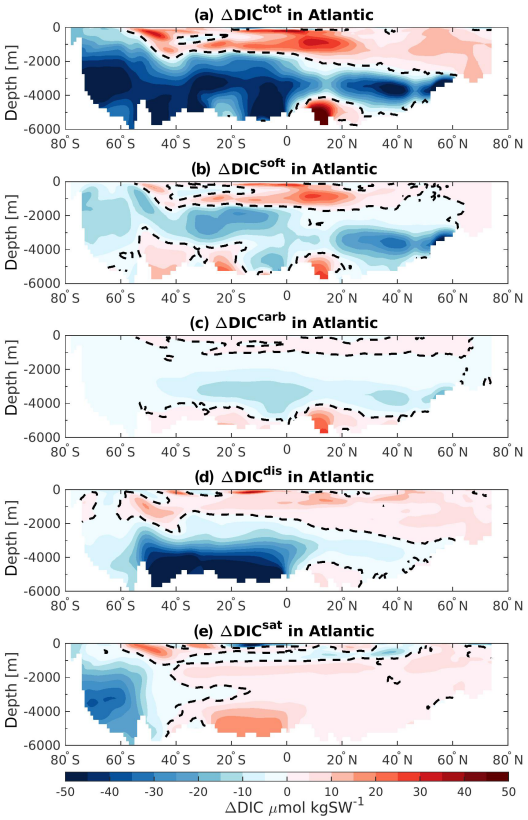

Figure 7. Atlantic zonally averaged section of the difference in **(a)** ΔDIC^{tot}, **(b)** ΔDIC^{soft}, **(c)** ΔDIC^{carb}, **(d)** ΔDIC^{dis}, and **(e)** ΔDIC^{sat} between 125 and 115 ka. The black dashed lines represent the zero values.

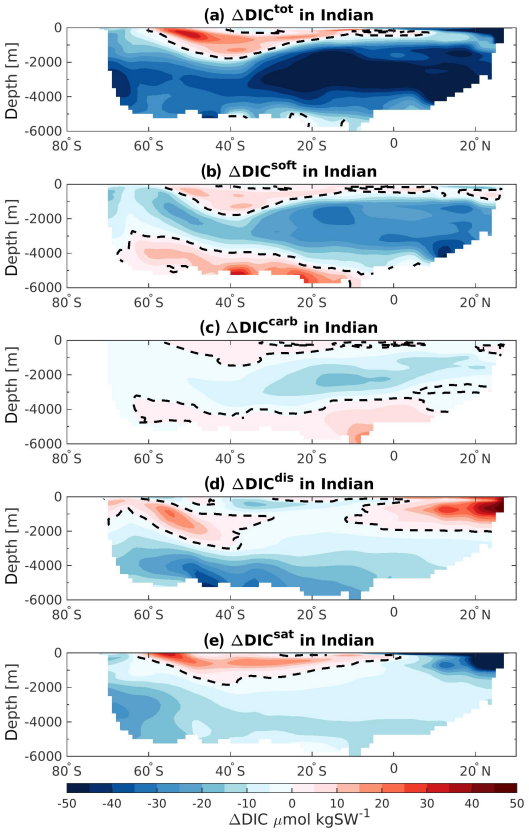

Figure 8. Same as Fig. 7 but for the Indian Ocean.

ΔDIC^{tot} pattern throughout most of the Indian Ocean. This decrease in biological remineralization is in agreement with the water mass age changes seen in Sect. 3.2 (Fig. 3b): younger water masses account for less biologically induced DIC content. However, the bottom and the surface waters show opposite signs in the ΔDIC^{tot}, which suggests that other processes are acting in these regions. The differences in the carbonate pump remain small and roughly follow the pattern of the soft-tissue pump (Fig. 8c). Changes in the bottom-water ΔDIC^{tot} can be attributed primarily to the difference in the disequilibrium effect, which is probably affected by larger influence of NSW at 125 ka relative to 115 ka as described for the Atlantic basin, and to a slight reduction in the saturation component. In addition, the disequilibrium component might also be influenced by stronger carbon export in the Southern Ocean (as the positive ΔDIC^{soft} and Fig. 5a suggest). The strong positive ΔDIC^{dis} simulated near the surface along the Indian coast is in good agreement with lower SSTs (Fig. 1a–c) allowing more DIC to be absorbed at 125 ka and a strong reduction in carbon export production (Fig. 5a). Finally the negative ΔDIC^{sat} depicted in the top layers in the north of the Indian Ocean is mainly attributed to a change in water mass origin from 115 to 125 ka. During 115 ka the SSW upwells from the deep ocean into the Arabian Sea. By contrast, at 125 ka, the waters coming from the Indonesian region mix with SSW. These Indonesian throughflow water masses initially coming from the Pacific Ocean are affected by strong precipitation in the Indonesian basin, which reduces the TALK at the surface and therefore DIC^{sat}.

The Pacific basin shows the strongest DIC^{tot} decrease in the Northern Hemisphere, mainly due to the reduction in soft-tissue pump (Fig. 9b). This decrease in biogenic carbon is induced by a better-ventilated water mass around 30° N (Fig. 3c), which may come from the increase of the overturning circulation in the upper cell of the Pacific Ocean. In contrast, the DIC inventory of the high-latitude South-

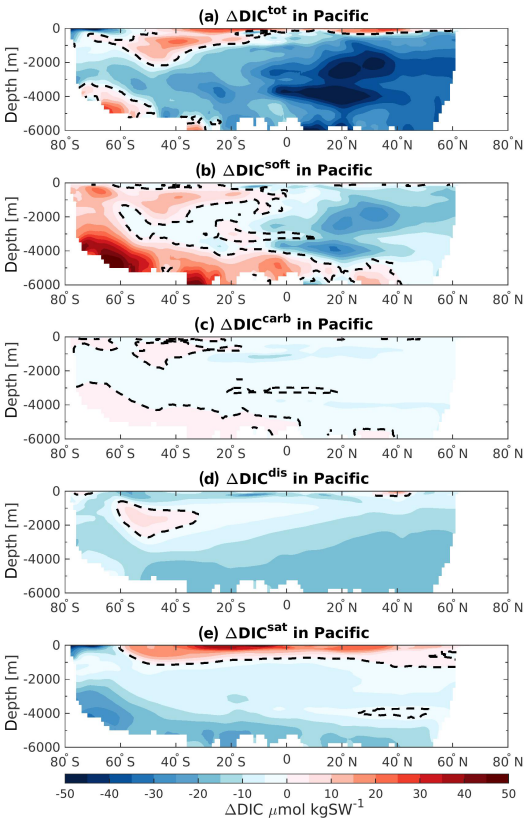

Figure 9. Same as Fig. 7 but for the Pacific Ocean.

ern Hemisphere bottom and near-surface waters is larger at 125 ka relative to 115 ka. This is attributed to the changes in soft-tissue pump, which is more effective at 125 ka due to longer residence time of the water masses (Fig. 3c). The carbonate pump has a relatively low impact on the total ΔDIC inventory in the Pacific basin but follows the same pattern as the changes in the organic carbon remineralization. The disequilibrium effect accounts for the strongest decrease of DIC throughout the basin as seen by the negative ΔDIC^{dis} in almost all regions (Fig. 9d). However, the bottom waters seem to be the most affected and become more undersaturated at 125 ka relative to 115 ka. This may be influenced by the slowing down of the subduction process in the Southern Ocean, induced by the flattening of the isopycnals. The possible higher carbon export production in the SO south of 60° S (Fig. 5a) may also push the water mass further out of equilibrium. Finally, the saturation component is controlling the changes occurring in the near-surface waters (Fig. 9e). Lower saturations are attributed to higher export of calcium carbonate south of 60° S, which lower the alkalinity at the surface and thereby the buffering capacity. On the other hand, the calcium carbonate formation decreases north of 60° S, resulting in a higher alkalinity and buffering capacity.

4 Discussion

The ocean plays an important role in storing carbon and, thus, in the long term regulation of atmospheric CO_2 levels. The processes involved in regulating the ocean carbon inventory are likely to change under warmer future conditions. In this study, we simulate two equilibrium states of the penultimate interglacial period using a state-of-the-art Earth system model and make a first attempt at quantifying the biogeochemical and physical processes responsible for carbon storage changes caused by different (interglacial) orbital configurations and background climates. Significant decreases in the ocean carbon storage capacity are found in a warmer climate. More than 48 % of this decrease is induced by the reduction of the biological pump. This decrease is found to be mainly driven by the shorter residence time of interior deep water masses arising from changes in Southern Ocean sea ice extent that influence the NSW and SSW mass geometry, in addition to changes in overturning circulation in the Atlantic (deeper but almost equally vigorous) and Pacific (stronger upper cell) basins.

Using the available proxy reconstructions during the LIG period allows us to assess the validity of important features in our model results. We assess the validity of the simulated 115–125 ka water mass geometry change using LIG proxy reconstructions of bottom-water $\delta^{13}C$, a water mass tracer strongly but inversely related to carbon and PO_4 contents (Eide et al., 2017). Similar to our results, expanded SSW in the late compared to early LIG is inferred from such reconstructions to explain bottom-water $\delta^{13}C$ decreases in different regions proximal to the Southern Ocean (Ninnemann and Charles, 2002; Govin et al., 2009). Bottom-water $\delta^{13}C$ reconstructions indicate less influence of NSW in the deep South Atlantic at 115 ka than at 125 ka (Ninnemann et al., 1999; Govin et al., 2009). In addition, persistent (millennial-scale) mid-depth NSW ventilation extending from the LIG and into the subsequent glacial inception is also suggested based on proxy reconstructions (Mokeddem et al., 2014; McManus et al., 2002) and is consistent with model simulations (Born et al., 2011; Wang and Mysak, 2002). In our study, even though the AMOC is simulated slightly stronger and deeper at 125 ka, vigorous AMOC persists until 115 ka, ventilating the North Atlantic mid-depth. We also note that our model may not properly represent North Atlantic overflows due to its sparse resolution. This can further add uncertainties to North Atlantic water ventilation.

Also consistent with our results, ice core proxies indicate that Southern Ocean sea ice extent is greater at 115 ka than at 125 ka (Wolff et al., 2006; Röthlisberger et al., 2008),

while our model reproduces the volumetric SSW expansion in response to this increase in Southern Ocean sea ice extent as suggested for glacial climates (e.g., Ferrari et al., 2014). Our model results suggest that similar sea ice (Fig. 1) and SSW expansions (Fig. 4a), albeit muted compared to glacial changes, occurred in response to LIG orbital configuration changes and without continental ice sheet growth (not included in the model), indicating a relatively tight coupling between Antarctic climate, sea ice, and the deep Atlantic water mass geometry changes influencing ocean carbon storage.

The changes in ocean carbon storage simulated by our model are significant and demonstrate that warm (interglacial) ocean carbon content changes with climate forcing. While atmospheric CO_2 is fixed in our model, preventing a direct assessment of ocean carbon changes in atmospheric CO_2, the decrease in deep carbon storage and shoaling of the DIC pool during the warm 125 ka interval is generally consistent with higher atmospheric CO_2 levels at this time. Our estimated changes in ocean carbon budget are in the range of previous modeling studies that also suggest weaker ocean carbon storage during the beginning of the LIG (125 ka) relative to the glacial inception (115 ka). Schurgers et al. (2006) obtain a difference in atmospheric and terrestrial carbon storage of about 40 and 350 PgC, respectively, between the onset and end of the LIG. This potentially translates to a weaker ocean carbon storage of 310 PgC at the onset compared to the late LIG, which corresponds well in absolute magnitude with our findings of 314.1 PgC decrease at 125 ka. However, their simulated atmospheric CO_2 steadily increases over this period, which potentially points toward more carbon needing to be stored in land or ocean toward the end of the LIG.

In contrast, Brovkin et al. (2016) simulate more ocean DIC^{tot} at 125 ka than 115 ka using simpler EMIC models. This increase is mainly attributed to the shallow-water carbonate precipitation implemented in their model. This process is not included in our model and could explain the differences in the results. However, their simulated change in atmospheric CO_2 after 121 ka is in the opposite direction (an increase of roughly 20 ppm) of the atmospheric trend (a decrease of roughly 3 ppm) observed in the ice core data. This suggests that either (or both) the terrestrial or the oceanic carbon reservoir does not take up enough carbon toward the end of the LIG in order to simulate a decrease in atmospheric CO_2 content.

Concerning the modification in the upper-ocean productivity under warmer climatic conditions, our model study shows a heterogeneous response in phosphate availability and carbon export production especially between the Atlantic and Pacific basins. Moore et al. (2018) also highlight such a biogeochemical divide response for future projections under warmer climatic conditions. This implies that future anthropogenic CO_2 forcings may have a similar impact on the biogeochemical divide to that of past forcings. Therefore, reconstructing and understanding the large-scale productivity responses to past climate forcing are critical for assessing both global and regional sensitivity of the ocean carbon dynamic to climate change.

There are limitations to our study. Factors that could influence ocean carbon storage including sea level, riverine input of nutrients, and atmospheric dust loading are all set to preindustrial levels in our simulations but may be different in the LIG. Global sea level, for example, may be as much as 6–9 m above present levels (Kopp et al., 2009). In addition, our model does not include weathering fluxes, which might influence the carbon budget on such a long timescale. Further, we compare two quasi-equilibrated states, which is unrealistic and ignores transient forcings and shorter-term variability. This may explain differences between our model results and some proxy reconstructions. For example, proxy reconstructions suggest that both NSW and SSW ventilation may have varied considerable near 125 ka (Galaasen et al., 2014; Hayes et al., 2014). The changes suggested by these studies include reductions of NSW and expansions of SSW similar to our modeled 115–125 ka equilibrium difference, albeit occurring as short-lived (centennial-scale) transient events associated with freshwater input episodes during the final phase of northern deglaciation (Galaasen et al., 2014). Our quasi-equilibrated model simulations for 115 and 125 ka also lack ice sheet and the corresponding freshwater input variability, nor do they address such shorter-term changes that could affect the ocean carbon inventory (Stocker and Schmittner, 1997). However, short-lived changes would likely have less impact on the ocean carbon inventory than the longer-term (millennial-scale) changes we address, the latter allowing all carbon system components and ocean dynamics to adjust. Thus, we still expect our model simulations to provide insight into baseline changes and redistribution of ocean DIC forced by the different LIG orbital configurations, supported by the important role of deep Atlantic water mass geometry changes coupled with its similarity to the long-term (millennial-scale) evolution inferred from proxy reconstructions.

5 Conclusions

Ongoing anthropogenic warming raises questions about the oceanic carbon sink and its efficiency under warmer climate conditions. In this study, we use the fully coupled NorESM model to simulate two quasi-equilibrium states of the Last Interglacial: one period is globally colder (115 ka) and one is globally warmer (125 ka) than today. We focus on the differences in ocean carbon cycle that occur at 125 ka in comparison to 115 ka, specifically the differences at global and basin scales. We provide a detailed description of the biogeochemical and physical processes that are responsible for the ocean carbon inventory changes under warmer climate conditions during the LIG at the temporal and spatial scales discussed here.

We find that the global ocean carbon budget decreases during the warm (125 ka) period by 314.1 PgC and is related mainly to better ventilation in the interior ocean. The Pacific Ocean has the largest reduction and accounts for 57 % of the global DIC loss. The response of the Pacific ventilation in a warmer climate shown in this study is consistent with previous studies (Menviel et al., 2014, 2015). The Indian and Atlantic basins account for 28 % and 15 %, respectively. These quantities mostly reflect basin volumes. The SSWs are revealed to play an instrumental role for the DIC changes in the interior below 1000 m depth. In these waters, the Atlantic is highlighted to be the region where the strongest DIC loss occurs per unit volume and is characterized by a stronger ventilation and a DIC^{tot} decrease of about 37 % compared to its respective value at 115 ka.

The reduced DIC budget at 125 ka occurs mostly in the interior ocean, while there is a weak increase in the top 1000 to 1500 m depths. Two factors that contribute most to the drop in the DIC budget in the interior ocean are (1) a weaker biological component from both the soft-tissue and the carbonate pumps that dominates at the depth between 1000 and 3000 m, and (2) a stronger disequilibrium effect (i.e., more negative) of DIC in the bottom waters. However, the processes affecting the disequilibrium component can arise from different factors such as changes in the physical pump, overturning circulation, or biological pump. No general process could be attributed to its variation, which seems to be regionally affected. While the SSWs seem to become more undersaturated at 125 ka, the NSWs seem to be more saturated. Further experiments with for instance fixed biological productivity or overturning circulation could help to identify the sensitivity of this component to such factors, but they remain too expensive to perform with our model.

The weakening of the biological component at depth is driven by younger water masses simulated in the interior ocean. This decrease in residence time of the water masses is caused by the strong SST modifications that affect the ventilation at 125 ka as compared to 115 ka. Higher SST, especially at high latitudes, induces strong summer sea ice retreat in the Atlantic sector of the Southern Ocean and stratification in the Pacific Ocean. In the Atlantic basin, this results in a more southerly confined SSW and southward expansion of NSW in the deep ocean. These water masses are advected by the Antarctic circumpolar current into the Indian and the western Pacific basins. The eastern Pacific Ocean is influenced by water masses coming from the Pacific sector of the Southern Ocean, with a warmer SST that hinders the ventilation and increases the residence time of the interior water masses on the eastern side of the basin.

Concerning the modification in the upper-ocean productivity under warmer climatic conditions, our model study reveals clear yet heterogeneous changes in phosphate availability and carbon export production especially between the Atlantic and Pacific basins. Such inter-basinal response in the biogeochemical divide is also highlighted by Moore et al. (2018) for future projections under warmer climatic conditions. This implies that changes in the biogeochemical divide could be somewhat similarly impacted from past and future anthropogenic CO_2 forcings, although the basin-specific responses suggest that it may not be a priori simple to predict the pattern or sign of the response of large-scale productivity to a given common forcing. Given the economic importance of basin scale productivity and the sensitivity found in past and future simulations, reconstructing and understanding the pattern and validating the sign and (model) response of large scale productivity to climate forcing are therefore critical for assessing not only the sign but also the sensitivity of global productivity to climate change.

The remaining uncertainties include, among others, the use of preindustrial states for some boundary conditions and the absence of freshwater input, which could modify the spatial response, particularly during the early interglacial period, which might include the final episodes of continental deglaciation. This is due to the lack of knowledge on such forcing during past climate conditions. Additional model-based studies using different Earth system models would be useful to confirm the robustness of our finding and further improve our understanding of the carbon dynamics and the feedback in the ocean under warmer climate conditions. Finally, our model-based study suggests that past warm periods experienced considerable carbon cycle and ocean DIC changes, linked to the response of the interior-ocean ventilation and biological productivity to high-latitude warming and interglacial background climate differences. It also suggests that the Atlantic part of the Southern Ocean is most sensitive to past climate change and hence could be a potential indicator of similar large-scale circulation changes in the future. Close monitoring of this region could be critical to better understand climate feedback on the carbon cycle under future warmer climate conditions.

Data availability. The model data are available on the Norwegian Research Data Archive server (https://doi.org/10.11582/2018.00038; Kessler, 2018).

Author contributions. AK and JP designed and analyzed the simulations, and wrote the first the first draft of the paper. EVG and USN revised and provided input on the paper. All authors discussed the results.

Competing interests. The authors declare no competing interests.

Acknowledgements. We thank Victor Brovkin and the two anonymous referees for their positive and constructive comments, which helped to clarify the manuscript. We also thank the editor, Laurie Menviel, for the time she dedicated in processing our

manuscript and for her additional comments and suggestions. We thank Nadine Goris for her valuable feedback on the first draft of the manuscript. We are grateful to Chuncheng Guo for his technical assistance. This work was supported by the Research Council of Norway-funded projects THRESHOLDS (254964) and ORGANIC (239965) and the Bjerknes Centre for Climate Research project BIGCHANGE. We acknowledge the Norwegian Metacenter for Computational Science and Storage Infrastructure (Notur/Norstore) projects nn2345k, ns2345k, nn1002k, and ns1002k for providing the computing and storing resources essential for this study.

Edited by: Laurie Menviel
Reviewed by: Victor Brovkin and two anonymous referees

References

Bentsen, M., Bethke, I., Debernard, J. B., Iversen, T., Kirkevåg, A., Seland, Ø., Drange, H., Roelandt, C., Seierstad, I. A., Hoose, C., and Kristjánsson, J. E.: The Norwegian Earth System Model, NorESM1-M – Part 1: Description and basic evaluation of the physical climate, Geosci. Model Dev., 6, 687–720, https://doi.org/10.5194/gmd-6-687-2013, 2013.

Bernadello, R., Marinov, I., Palter, J. B., Sarmiento, J. L., Galbraith, E. D., and Slater, R. D.: Response of the Ocean Natural Carbon Storage to Projected Twenty–First–Century Climate Change, J. Climate, 27, 2033–2053, https://doi.org/10.1175/JCLI-D-13-00343.1, 2014.

Bleck, R., Rooth, C., Hu, D., and Smith, L. T.: Salinity-driven thermocline transients in a wind– and thermohaline–forced isopycnic coordinate model of the north Atlantic, J. Pys. Oceanogr., 22, 1486–1505, https://doi.org/10.1175/1520-0485(1992)022<1486:SDTTIA>2.0.CO;2, 1992.

Born, A., Nisancioglu, K. H., and Risebrobakken, B.: Late Eemian warming in the Nordic Seas as seen in proxy data and climate models, Paleoceanography, 26, PA2207, https://doi.org/10.1073/pnas.1322103111, 2011.

Broecker, W. S.: "NO", A conservative water-mass tracer, Earth Planet. Sc. Lett., 23, 100–107, https://doi.org/10.1016/0012-821X(74)90036-3, 1974.

Brovkin, V., Brücher, T., Kleinen, T., Zaehle, S., Joos, F., Roth, R., Spahni, R., Schmitt, J., Fischer, H., Leuenberger, M., Stone, E. J., Ridgwell, A., Chapellaz, J., Kehrwald, N., Barbante, C., Blunier, T., and Jensen, D. D.: Comparative carbon cycle dynamics of the present and last interglacial, Quaternary Sci. Rev., 137, 15–32, https://doi.org/10.1016/j.quascirev.2016.01.028, 2016.

Capron, E., Govin, A., Stone, E. J., Masson-Delmotte, V., Mulitza, S., Otto-Bliesner, B., Rasmussen, T. L., Sime, L. C., Waelbroeck, C., and Wolff, E. W.: Temporal and spatial structure of multi-millennial temperature changes at high latitudes during the Last Interglacial, J. Quaternary Sci., 103, 116–133, https://doi.org/10.1016/j.quascirev.2014.08.018, 2014.

Dickson, A. G. and Millero, F. J.: A comparison of the equilibrium constants for the dissociation of carbonic acid in seawater media, Deep-Sea Res., 34, 1733–1743, https://doi.org/10.1016/0198-0149(87)90021-5, 1987.

Dorthe Dahl-Jensen, Gogineni, P., and White, J. W. C.: Reconstruction of the last interglacial period from the NEEM ice core, Nature, 493, 489–489, 2013.

Duteil, O., Koeve, W., Oschlies, A., Aumont, O., Bianchi, D., Bopp, L., Galbraith, E., Matear, R., Moore, J. K., Sarmiento, J. L., and Segschneider, J.: Preformed and regenerated phosphate in ocean general circulation models: can right total concentrations be wrong?, Biogeosciences, 9, 1797–1807, https://doi.org/10.5194/bg-9-1797-2012, 2012.

Eide, M., Olsen, A., Ninnemann, U. S., and Johannessen, T.: A global ocean climatology of preindustrial and modern ocean δ^{13}C, Global Biogeochem. Cy., 31, 515–534, https://doi.org/10.1002/2016GB005473, 2017.

Eppley, R. W.: Temperature and phytoplankton growth in the sea, Fish. B.-NOAA, 70, 1063–1085, 1972.

Ferrari, R., Jansen, M. F., Adkins, J. F., Burke, A., Stewart, A. L., and Thompson, A. F.: Antarctic sea ice control on ocean circulation in present and glacial climates, P. Natl. Acad. Sci. USA, 111, 8753–8758, https://doi.org/10.1073/pnas.1323922111, 2014.

Follows, M. and Williams, R.: Mechanisms controlling the air–sea flux of CO_2 in the North Atlantic, The Ocean Carbon Cycle and Climate, edited by: Follows, M. and Oguz, T., Kluwer Academic, 217–249, https://doi.org/10.1007/978-1-4020-2087-2_7, 2004.

Galaasen, E. V., Ninnemann, U. S., Irvali, N., Kleiven, H. F., Rosenthal, Y., Kissel, C., and Hodell, D. A.: Rapid Reductions in North Atlantic Deep Water During the Peak of the Last Interglacial Period, Science, 343, 1129–1132, https://doi.org/10.1126/science.1248667, 2014.

Govin, A., Michel, E., Labeyrie, L., Waelbroeck, C., Dewilde, F., and Jansen, E.: Evidence for northward expansion of Antarctic Bottom Water mass in the Southern Ocean during the last glacial inception, Paleoceanography, 24, PA1202, https://doi.org/10.1029/2008PA001603, 2009.

Gu, D. and Philander, S. G. H.: Interdecadal climate fluctuations that depend on exchanges between the tropics and extratropics, Science, 275, 805–807, https://doi.org/10.1126/science.275.5301.805, 1997.

Guo, C., Bentsen, M., Bethke, I., Ilicak, M., Tjiputra, J., Toniazzo, T., Schwinger, J., and Otterå, O. H.: Description and evaluation of NorESM1-F: A fast version of the Norwegian Earth System Model (NorESM), Geosci. Model Dev. Discuss., https://doi.org/10.5194/gmd-2018-217, in review, 2018.

Hayes, C. T., Martinez-Garcia, A., Hasenfratz, A., Jaccard, S. L., Hodell, D. A., Sigman, D. M., Haug, G. H., and Anderson, R. F.: A stagnation event in the deep South Atlantic during the last interglacial period, Science, 346, 1514–1517, https://doi.org/10.1126/science.1256620, 2014.

Heinze, C., Maier-Reimer, E., Winguth, A. M. E., and Archer, D.: A global oceanic sediment model for long-term climate studies, Global Biogeochem. Cy., 13, 221–250, https://doi.org/10.1029/98GB02812, 1999.

Hoffman, J. S., Clark, P. U., Parnell, A. C., and He, F.: Regional and global sea-surface temperatures during the last interglaciation, Science, 355, 276–279, https://doi.org/10.1126/science.aai8464, 2017.

Kessler, A.: NorESM-F_LIG115_LIG125_year_4951-5000 [Data set], Norstore, https://doi.org/10.11582/2018.00038, 2018.

Kleinen, T., Brovkin, V., and Munhoven, G.: Modelled interglacial carbon cycle dynamics during the Holocene, the Eemian and Marine Isotope Stage (MIS) 11, Clim. Past, 12, 2145–2160, https://doi.org/10.5194/cp-12-2145-2016, 2016.

Kopp, R. E., Simons, F. J., Mitrovica, J. X., Maloof, A. C., and Oppenheimer, M.: Probabilistic assessment of sea level during the last interglacial stage, Nature, 462, 863–867, https://doi.org/10.1038/nature08686, 2009.

Lawrence, D. M., Oleson, K. W., Flanner, M. G., Fletcher, C. G., Lawrence, P. J., Levis, S., Swenson, S. C., and Bonan, G. B.: The CCSM4 land simulation, 1850–2005: assessment of surface climate and new capabilities, J. Climate, 25, 2240–2260, https://doi.org/10.1175/JCLI-D-11-00103.1, 2012a.

Lourantou, A., Chappellaz, J., Barnola, J. M., Masson-Delmotte, V., and Raynaud, D.: Changes in atmospheric CO_2 and its carbon isotopic ratio during the penultimate deglaciation, Quaternary Sci. Rev., 29, 1983–1992, https://doi.org/10.1016/j.quascirev.2010.05.002, 2010.

Luo, Y., Tjiputra, J. F., Guo, C., Zhang, Z., and Lippold, J.: Atlantic deep water circulation during the last interglacial, Sci. Rep.-UK, 8, 4401, https://doi.org/10.1038/s41598-018-22534-z, 2018.

Maier-Reimer, E.: Geochemical cycles in an ocean general circulation model, preindustrial tracer distributions, Global Biogeochem. Cy., 7, 645–677, https://doi.org/10.1029/93GB01355, 1993.

Maier-Reimer, E., Kriest, I., Segschneider, J., and Wetzel, P.: The HAMburg Ocean Carbon Cycle Model HAMOCC5.1 – Technical Description Release 1.1, Berichte zur Erdsystemforschung 14, ISSN 1614-1199, Max Planck Institute for Meteorology, Hamburg, Germany, 50 pp., 2005.

Marinov, I., Gnanadesikan, A., Toggweiler, R., and Sarmiento, J. L.: The Southern Ocean Biogeochemical Divide, Nature, 441, 946–967, https://doi.org/10.1038/nature04883, 2006.

Masson-Delmotte, V., Stenni, B., Pol, K., Braconnot, P., Cattani, O., Falourd, S., Kageyama, M., Jouzel, J., Landais, A., Minster, B., Barnola, J. M., Chappellaz, J., Krinner, G., Johnsen, S., Röthlisberger, R., Hansen, J., Mikolajewicz, U., and Otto-Bliesner, B.: EPICA Dome C record of glacial and interglacial intensities, Quaternary Sci. Rev., 29, 113–128, https://doi.org/10.1016/j.quascirev.2009.09.030, 2010.

McManus, J. F., Oppo, D. W., Keigwin, L. D., Cullen, J. L., and Bond, G. C.: Thermohaline circulation and prolonged interglacial warmth in the North Atlantic, Quaternary Res., 58, 17–21, https://doi.org/10.1006/qres.2002.2367, 2002.

Mehrbach, C., Culberson, C. H., Hawley, J. E., and Pytkwicz, R. M.: Measurement of the apparent dissociation constants of carbonic acid in seawater at atmospheric pressure, Limnol. Oceanogr., 18, 897–907, https://doi.org/10.4319/lo.1973.18.6.0897, 1973.

Menviel, L., Joos, F., and Ritz, S. P.: Simulating atmospheric CO_2, $\delta^{13}C$ and the marine carbon cycle during the Last Glaciale/Interglacial cycle: possible role for a deepening of the mean remineralization depth and an increase in the oceanic nutrient inventory, Quaternary Sci. Rev., 56, 46–68, https://doi.org/10.1016/j.quascirev.2012.09.012, 2012.

Menviel, L., England, M. H., Meissner, K. J., Mouchet, A., and Yu, J.: Atlantic-Pacific seesaw and its role in outgassing CO_2 during Heinrich events, Paleoceanography, 29, 58–70, https://doi.org/10.1002/2013PA002542, 2014.

Menviel, L., Mouchet, A., Meissner, K. J., Joos, F., and England, M. H.: Impact of oceanic circulation changes on atmospheric $\delta^{13}CO_2$, Global Biogeochem. Cy., 29, 1944–1961, https://doi.org/10.1002/2015GB005207, 2015.

Mokeddem, Z., McManus, J. F., and Oppo, D. W.: Oceanographic dynamics and the end of the last interglacial in the subpolar North Atlantic, P. Natl. Acad. Sci. USA, 111, 11253–11268, https://doi.org/10.1073/pnas.1322103111, 2014.

Moore, J. K., Fu, W., Primeau, F., Britten, G. L., Lindsay, K., Long, M., Doney, S. C., Mahowald, N., Hoffman, F., and Randerson, J. T.: Sustained climate warming drives declining marine biological productivity, Science, 359, 1139–1143, https://doi.org/10.1126/science.aao6379, 2018.

Ninnemann, U. S. and Charles, C. D.: Changes in the mode of Southern Ocean circulation over the last glacial cycle revealed by foraminiferal stable isotopic variability, Earth Planet. Sc. Lett., 201, 383–396, https://doi.org/10.1016/S0012-821X(02)00708-2, 2002.

Ninnemann, U. S., Charles, C. D., and Hodell, D. A.: Origin of global millennial scale climate events: constraints from the Southern Ocean deep sea sedimentary record, Geophysical Monograph-American Geophysical Union, 112, 99–112, 1999.

Otto-Bliesner, B. L., Marshall, S. J., Overpeck, J. T., Miller, G. H., Hu, A., and CAPE Last Interglacial Project members: Simulating Arctic Climate Warmth and Icefield Retreat in the Last Interglaciation, Science, 311, 1751–1753, https://doi.org/10.1126/science.1120808, 2006.

Otto-Bliesner, B., Rosenbloom, N., Stone, E., Mckay, N. P., Lunt, D. J., Brady, E. C., and Overpeck, J. T.: How warm was the Last Interglacial? New model-data comparisons, Philos. T. R. Soc. A, 371, 20130097, https://doi.org/10.1098/rsta.2013.0097, 2013.

Ridgwell, A.: Glaciale/Interglacial Perturbations in the Global Carbon Cycle, PhD thesis, University of East Anglia, Norwich, UK, 2001.

Röthlisberger, R., Mudelsee, M., Bigler, M., de Angelis, M., Fischer, H., Hansson, M., Lambert, F., Masson-Delmotte, V., Sime, L., Udisti, R., and Wolff, E. W.: The Southern Hemisphere at glacial terminations: insights from the Dome C ice core, Clim. Past, 4, 345–356, https://doi.org/10.5194/cp-4-345-2008, 2008.

Sarmiento, J. L., Slater, R., Barber, R., Bopp, L., Doney, S. C., Hirst, A. C., Kleypas, J., Matear, R., Mikolajewicz, U., Monfray, P., Soldatov, V., Spall, S. A., and Stouffer, R.: Response of ocean ecosystems to climate warming, Global Biogeochem. Cy., 18, GB3003, https://doi.org/10.1029/2003GB002134, 2004a.

Sarmiento, J. L., Gruber N., Brzezinski, M. A., and Dunne, J. P.: High-latitude controls of thermocline nutrients and low latitude biological productivity, Nature, 427, 56–60, https://doi.org/10.1038/nature02127, 2004b.

Schneider, R., Schmitt, J., Köhler, P., Joos, F., and Fischer, H.: A reconstruction of atmospheric carbon dioxide and its stable carbon isotopic composition from the penultimate glacial maximum to the last glacial inception, Clim. Past, 9, 2507–2523, https://doi.org/10.5194/cp-9-2507-2013, 2013.

Schurgers, G., Mikolajewicz, U., Gröger, M., Maier-Reimer, E., Vizcaíno, M., and Winguth, A.: Dynamics of the terrestrial biosphere, climate and atmospheric CO_2 concentration during interglacials: a comparison between Eemian and Holocene, Clim. Past, 2, 205–220, https://doi.org/10.5194/cp-2-205-2006, 2006.

Sigman, D. and Boyle, E.: Glacial/interglacial variations in atmospheric carbon dioxide, Nature, 407, 859–869, https://doi.org/10.1038/35038000, 2000.

Smith, E. L.: Photosynthesis in relation to light and carbon dioxide, P. Natl. Acad. Sci. USA, 22, 504–511, 1936.

Stocker, T. F. and Schmittner, A.: Influence of CO_2 emission rates on the stability of the thermohaline circulation, Nature, 388, 862–865, https://doi.org/10.1038/42224, 1997.

Tjiputra, J. F., Roelandt, C., Bentsen, M., Lawrence, D. M., Lorentzen, T., Schwinger, J., Seland, Ø., and Heinze, C.: Evaluation of the carbon cycle components in the Norwegian Earth System Model (NorESM), Geosci. Model Dev., 6, 301–325, https://doi.org/10.5194/gmd-6-301-2013, 2013.

Turney, C. S. M. and Jones, R. T.: Does the Agulhas Current amplify global temperatures during super-interglacials?, J. Quaternary Sci., 25, 839–843, https://doi.org/10.1002/jqs.1423, 2010.

van Heuven, S., Pierrot, D., Rae, J. W. B., Lewis, E., and Wallace, D. W. R.: Matlab program developed for CO_2 system calculations. ornl/cdiac-105b., Carbon Dioxide Information Analysis Center, Oak Ridge National Laboratory, US Department of Energy, Oak Ridge, Tennessee, available at: http://cdiac.ornl.gov/ftp/co2sys/CO2SYS_calc_MATLAB_v1.1/ (last access: 5 December 2018), 2011.

Wang Z. and Mysak, L. A.: Simulation of the last glacial inception and rapid ice sheet growth in the McGill Paleoclimate Model, Geophys. Res. Lett., 29, 2102, https://doi.org/10.1029/2002GL015120, 2002.

Wanninkhof, R.: Relationship between wind speed and gas exchange over the ocean, J. Geophys. Res., 97, 7373–7382, https://doi.org/10.1029/92JC00188, 1992.

Weiss, R. F.: The solubility of nitrogen, oxygen and argon in water and sea water, Deep-Sea Res., 17, 721–735, https://doi.org/10.1016/0011-7471(70)90037-9, 1970.

Weiss, R. F.: Carbon dioxide in water and seawater: the solubility of a non–ideal gas, Mar. Chem., 2, 203–215, https://doi.org/10.1016/0304-4203(74)90015-2, 1974.

Wolff, E. W., Fischer, H., Fundel, F., Ruth, U., Twarloh, B., Littot, G. C., Mulvaney, R., Röthlisberger, R., de Angelis, M., Boutron, C. F., Hansson, M., Jonsell, U., Hutterli, M. A., Lambert, F., Kaufmann, P., Stauffer, B., Stocker, T. F., Steffensen, J. P., Bigler, M., Siggaard-Andersen, M. L., Udisti, R., Becagli, S., Castellano, E., Severi, M., Wagenbach, D., Barbante, C., Gabrielli P., and Gaspari, V.: Southern Ocean sea-ice extent, productivity and iron flux over the past eight glacial cycles, Nature, 440, 491–496, https://doi.org/10.1038/nature04614, 2006.

Paper II

4.2 Atlantic Meridional Overturning Circulation and $\delta^{13}C$ variability during the Last Interglacial

Augustin Kessler, Nathaelle Bouttes, Didier M. Roche, Ulysses S. Ninnemann, Eirik V. Galaasen and Jerry F. Tjiputra

in revision: Paleoceanography and Paleoclimatology.

Atlantic Meridional Overturning Circulation and $\delta^{13}C$ variability during the Last Interglacial

A. Kessler [1], N. Bouttes [2], D. M. Roche [2,3], U. S. Ninnemann [4], E. V. Galaasen [4], J. Tjiputra [1]

[1]NORCE Norwegian Research Centre, Bjerknes Centre for Climate Research, P.O. Box 22, 5838 Bergen, Norway
[2]Laboratoire des Sciences du Climat et de l'Environnement, LSCE/IPSL, CEA-CNRS-UVSQ, Université Paris-Saclay, F-91190 Gif-sur-Yvette, France
[3]Department of Earth Sciences, VU University Amsterdam, De Boelelaan 1085, 1081 HV Amsterdam, The Netherlands
[4]Department of Earth Science, University of Bergen and Bjerknes Centre for Climate Research, Bergen, Norway

Key Points:

- Comparable variations of simulated North Atlantic bottom water $\delta^{13}C_{DIC}$ to that found in high-resolution data $\delta^{13}C$ reconstructions.
- Changes in AMOC strength may be a key process in distributing $\delta^{13}C$ in the ocean interior.
- Magnitude of local bottom water $\delta^{13}C_{DIC}$ response depends on position relative to water mass geometry.

Corresponding author: Augustin Kessler, auke@norceresearch.no

Abstract

The Atlantic meridional overturning circulation (AMOC) is thought to be relatively vigorous and stable during Interglacial periods on multi-millennial (equilibrium) timescales. However, recent proxy ($\delta^{13}C$ benthic) reconstructions suggest that higher frequency variability in deep water circulation may have been common during some interglacial periods, including the Last Interglacial (LIG, 130ka - 115ka). The origin of these isotope variations and their implications for past AMOC remain poorly understood. Using iLOVECLIM, an Earth system model of intermediate complexity (EMIC) allowing the computation of $\delta^{13}C_{DIC}$ and direct comparison to proxy reconstructions, we perform a transient experiment of the LIG (125ka -115ka) forced only by boundary conditions of greenhouse gases and orbital forcings. The model simulates large centennial-scale variations in the interior $\delta^{13}C_{DIC}$ of the North Atlantic similar in timescale and amplitude to changes resolved by high-resolution reconstructions from the LIG. In the model, these variations are caused by changes in the relative influence of North Atlantic Deep water (NADW) and southern source water (SSW), and are closely linked to large ($\sim$50 %) changes in AMOC strength provoked by saline input and associated deep convection areas south of Greenland. We identify regions within the subpolar North Atlantic with different sensitivity and response to changes in preformed $\delta^{13}C_{DIC}$ of NADW and to changes in NADW versus SSW influence, which is useful for proxy record interpretation. This could explain the relatively large $\delta^{13}C$ gradient ($\sim$0.4 ‰) observed at $\sim$3 km water depth in the subpolar North Atlantic at the inception of the last glacial.

1 Introduction

Variation in the Atlantic meridional overturning circulation (AMOC) is one of the major driving force controlling climate changes as it affects the distribution of heat and carbon in the ocean, thus influencing regional climate and atmospheric CO_2 concentrations (Ganachaud & Wunsch, 2000). This has made AMOC changes a key concern in future projections, with models suggesting it will likely decrease in response to buoyancy gain in the deep-water formation regions but the extent to which remains highly uncertain (Stocker et al., 2014; Bakker et al., 2016). Meanwhile, recent observations hint that the ocean circulation may have already started changing (Smeed et al., 2014; Caesar et al., 2018).

Analyzing past variability of AMOC can inform us on its stability and tendency to change. The Interglacial periods of the late Pleistocene are particularly interesting in this regard as they shared overall similar boundary conditions with the modern climate (Berger et al., 2015). The climate of the Last Interglacial (LIG), or Marine Isotope Stage (MIS) 5e in isotopic marine series, also shared similar features with the model projections of our future climate if anthropogenic greenhouse gas emissions continue unabated: high-latitudes warming (Otto-Bliesner et al., 2013; Hoffman et al., 2017), reduction of Greenland ice-sheet and higher sea level (Otto-Bliesner et al., 2006; Kopp et al., 2009). Hence, the high-latitude changes occurring during the warm MIS 5e could provide additional insight on AMOC variability. Data reconstructions from this period (130ka - 115ka) characterize this circulation with a periodically warmer and fresher than today North Atlantic water (Otto-Bliesner et al., 2006; Hoffman et al., 2017). Reconstructions of millennial-timescale variability indicate that vigorous North Atlantic Deep Water (NADW) production persisted on millennial-timescales (Adkins et al., 1997; Oppo et al., 1997), simultaneously as southern source waters (SSW) expanded northward at depth towards 115ka and the last glacial inception (Govin et al., 2009). The influence of Atlantic surface water into the Nordic Seas and farther north into the Arctic ocean is also suggested to have occurred during the late MIS 5e (Van Nieuwenhove et al., 2011).

The shorter-term transient behavior of the ocean circulation during this warmer period remains, however, poorly constrained as is it difficult to robustly identify and as-

sess such short-timescale variability in the marine record. Nevertheless, new generations of high resolution (down to multi-decadal) proxy reconstructions, more appropriate to resolve multi-centennial variability, suggest the existence of centennial short-lived large perturbations of the NADW during previous interglacial periods (McManus et al., 1999; Ninnemann & Charles, 2002; Hodell et al., 2009; Galaasen et al., 2014). Data reconstructions of $\delta^{13}C$ - an ocean circulation and carbon cycle tracer – from sediment cores in the North Atlantic depict abrupt centennial-scale variations on the order of 0.7‰, comparable to the deep Atlantic $\delta^{13}C$ changes observed during glacial periods and associated with changes in the distribution and ventilation of NADW (McManus et al., 1999, 2004; Henry et al., 2016; Menviel et al., 2017). This suggests possibly large and abrupt variations in ocean ventilation, which challenges the paradigm of the stability of interglacial thermohaline circulation at short timescales (Hodell et al., 2009; Galaasen et al., 2014). While the existence of such AMOC change is consistent with some observed climate variability (Bauch et al., 2011; Mokeddem et al., 2014; Galaasen et al., 2015; Tzedakis et al., 2018; Zhuravleva & Bauch, 2018), the relationship between benthic $\delta^{13}C$ and ocean circulation is not straightforward and requires additional tool such as model simulations to evaluate their degree of interactions (Bakker et al., 2015).

With respect to the model-data comparison, numerous studies have analyzed the $\delta^{13}C$ distribution variations under various boundary conditions using, for example, two-dimensional ocean models (Bouttes et al., 2009, 2010, 2012; Brovkin et al., 2007) and more complex three-dimensional models (Bakker et al., 2015; Menviel et al., 2017). These studies propose linkages between the millennial-scale variations of $\delta^{13}C$ and changes in a number of processes such as water mass distribution changes (which can be due to interaction with sea-ice formation), biological activity changes (for example due to iron fertilization) and land vegetation modification. However, to the authors' knowledge, there is no modeling studies, which simulate abrupt and large modification in the bottom water $\delta^{13}C$ with the amplitude and timescale depicted by the high-resolution reconstruction data (Hodell et al., 2009; Galaasen et al., 2014), such as shown here. Such constraints are needed to assess, for example, whether it is mechanistically plausible for changes in water mass distribution to have driven abrupt centennial-scale variability in bottom water $\delta^{13}C$ and, furthermore, whether such tracer field adjustments could be linked to AMOC variability. Determining the characteristic pattern or fingerprint in interior ocean $\delta^{13}C$ related to AMOC changes would provide a more realistic and physically consistent framework for interpreting past circulation variability and its implication for the carbon cycling, but also in understanding its recent (Caesar et al., 2018) and potential future changes (Weijer et al., 2019). Here we span this knowledge gap by using iLOVECLIM, an Earth system model of intermediate complexity (EMIC), to perform a transient simulation of the LIG (125ka to 115ka) under past natural variations in natural greenhouse gases and transient orbital forcings.

The paper is organized as follows: in Sect. 2, we describe the model, the experiment design, and the terms and metrics used to analyze the water mass geometry in the interior ocean during the transient simulation. Section 3 presents the results of the model simulations, while discussions and comparison with previous studies are presented in Sect. 4. Finally, the study is summarized in Sect. 5.

2 Method

2.1 Model description

This study uses the Earth system model of intermediate complexity iLOVECLIM, a LOVECLIM model branch which also includes carbon isotopes. The atmosphere, ocean and vegetation components are similar to that in LOVECLIM version 1.2 (Roche et al., 2007; Goosse et al., 2010). The atmospheric component ECBilt was developed at the Dutch Royal Meteorological Institute (Opsteegh et al., 1998) and is composed of three verti-

cal layers at 800, 500 and 200 hPa and has a horizontal resolution of 5.6°. To better represent the dynamics of the Hadley cell, ageostrophic terms are added to the quasi-geostrophic approximation dynamical core. The oceanic component CLIO has a horizontal resolution of approximately 3° and adopts 20 levels on the vertical coordinate including a realistic bathymetry. The oceanic general circulation model (Goosse & Fichefet, 1999) is based on Navier-stokes equations and includes a parametrization for down-sloping currents (Campin & Goosse, 1999) and an updated version of the thermodynamical sea-ice component of Fichefet and Maqueda (1997, 1999). The terrestrial biosphere model (VECODE) is composed of three sub-models that exchange heat, stress, water and carbon and are designed for long term simulations (Brovkin et al., 1997). In addition to desert, the dynamic vegetation model simulates two types of plants – trees and grass – which are subdivided into four compartments (leaves, wood, litter and soil) that exchange carbon in the biogeochemical model. The model of vegetation structure computes the fraction of plant functional type (PFT) in equilibrium with the climate where photosynthesis depends on precipitation, temperature and atmospheric CO_2.

The ocean carbon cycle model is divided into organic and inorganic parts which are based on the nutrient-phytoplankton-zooplankton-detritus (NPZD) model described in Six and Maier-Reimer (1996). The inorganic carbon is represented by the dissolved inorganic carbon (DIC) and alkalinity (ALK), while the organic part includes phytoplankton, zooplankton, dissolved organic carbon (DOC), slow dissolved organic carbon (DOCs), particulate organic carbon (POC) and calcium carbonate ($CaCO_3$). The plankton is partially remineralized as it sinks through the water column, while all the POC and $CaCO_3$ is remineralized at depth. The remineralization profile follows an exponential law, however, it is adjusted to have less remineralization in the upper layers and more at depth. At the air-sea interface the carbon flux is computed from the CO_2 partial pressure (pCO_2) difference between the atmosphere and the ocean at a constant gas exchange coefficient of 0.06 $mol.m^{-2}.yr^{-1}$. The sea surface pCO_2 is a function of temperature, salinity, DIC and ALK following Millero (1995). The iLOVECLIM model is using a similar carbon cycle as in CLIMBER-2 where the ^{13}C is computed in the ocean and terrestrial biosphere as in (Brovkin et al., 2007) and is fully described in (Bouttes et al., 2015).

2.2 Experiment set up

We have performed a transient experiment over the 125ka-115ka period of the Last Interglacial by prescribing yearly interpolated values of greenhouse gases (CO_2, CH_4 and N_2O) and orbital forcings from the third phase of the Paleoclimate Modelling Intercomparison Project (PMIP3; $URL = https://pmip3.lsce.ipsl.fr/$). This experiment is branched off after two consecutive runs in order to set the initial conditions: (1) a preindustrial spin up followed by (2) an equilibrium experiment using 125ka boundary conditions. Both experiments (1) and (2) are simulated over 5,000 model years. The preindustrial spin-up reproduces well the main ocean carbon cycle characteristics and is similar to that described in (Bouttes et al., 2015). The atmospheric $\delta^{13}C$ and CO_2 concentrations are -6.5 ‰ and 282 ppm, respectively, while the ocean and terrestrial biosphere carbon content are 38 952 and 2 094 PgC. The most important features of the different water masses are reproduced and the oceanic $\delta^{13}C$ ($\delta^{13}C_{DIC}$) is relatively well simulated as compared to the data (Schmittner et al., 2013; Eide et al., 2017), with higher $\delta^{13}C$ at the surface due to photosynthesis and lower $\delta^{13}C$ in the deeper ocean where remineralization takes place (Fig. 1a). It also depicts the water mass characteristics of NADW (high-$\delta^{13}C$) and Antarctic Bottom Water (AABW, low-$\delta^{13}C$) and the Equatorial subsurface minimum induced by strong remineralization. However, the high $\delta^{13}C$ values from the NADW penetrate further south in the data reconstruction (Fig. 1b) than that simulated in our model, which is likely the result of too strong diffusion in the model (Bouttes et al., 2015). In other regions, the magnitude and the large-scale spatial pattern of the $\delta^{13}C_{DIC}$ tracer are fairly comparable to the observations.

In the 125ka equilibrium run, i.e., experiment (2), the model simulation reaches equilibrium after 3 000 model years where the ocean and land vegetation carbon content stabilize at 38 857 ± 1 PgC and 23 235 ± 4 PgC, respectively over the proceeding 2 000 simulation years. The atmospheric CO_2 and the other greenhouse gases are kept constant (CO_2 = 276 ppmv; CH_4 = 640 ppb and N_2O = 263 ppb). The end of the 125ka equilibrium run is used as starting point for the 125ka-115ka transient simulation. Changes into the carbon reservoirs are simulated during this period corresponding into a reduction of the ocean carbon content at 125ka as compared to 115ka of about 360 PgC. This value is of the same order of magnitude with that suggested by previous studies analyzing the ocean carbon system during the LIG, e.g., Schurgers et al. (2006) and Kessler et al. (2018) with 310 and 314 PgC, respectively. However, contrary to the data reconstruction that shows relative stable atmospheric CO_2 concentration around 270-280 ppm throughout the LIG (Lourantou et al., 2010; Schneider et al., 2013), our model simulates an increase after 123.5ka until it stabilizes again around 116ka to 305 ppm (nearly 30 ppm above the data reconstruction). This increase is attributed to the strong reduction in land vegetation carbon content (∼420 PgC) induced by gradual cooling of the northern Hemisphere ($\sim 2°C$) and potentially the absence of permafrost in the model.

We note that this experiment has also been used in Galaasen et al. (2020) to illustrate the similarity between simulated and reconstructed bottom water $\delta^{13}C$ changes in recent interglacials. Hereafter we provide a detailed analysis of this simulation defining the cause of the simulated $\delta^{13}C_{DIC}$ anomalies, their spatial patterns in the deep North Atlantic, and potential drivers of $\delta^{13}C_{DIC}$ variability.

2.3 $\delta^{13}C$ tracer

The $\delta^{13}C$ represents the standardized $^{13}C/^{12}C$ ratio (Zeebe & Wolf-Gladrow, 2001) and is expressed in permil units as follows:

$$\delta^{13}C = \left(\frac{(^{13}C/^{12}C)}{(^{13}C/^{12}C)_{standard}} - 1\right) \times 1000 \quad (1)$$

where, $(^{13}C/^{12}C)_{standard}$ is the Pee Dee Belemnite carbon isotope standard (Craig, 1957). Hereafter we consider the $\delta^{13}C$ of DIC in the ocean, noted $\delta^{13}C_{DIC}$. During the photosynthesis marine and terrestrial biology preferentially use the lighter ^{12}C over ^{13}C. When organic matter is remineralized at depth, more ^{12}C is released as compared to ^{13}C, therefore producing low $\delta^{13}C_{DIC}$. On the opposite, at the surface ocean, the excess sequestration of ^{12}C, relative to ^{13}C, during photosynthesis drives an increase in $\delta^{13}C_{DIC}$. Thus, the distribution of $\delta^{13}C_{DIC}$ is affected by air-sea gas exchange and marine biological fractionation (Lynch-Stieglitz et al., 1995; Zhang et al., 1995; Schmittner et al., 2013; Eide et al., 2017) and as other oceanic tracers, is transported by the advection-diffusion scheme in the oceanic model. The analysis of $\delta^{13}C_{DIC}$ is often used to reconstruct the variations in ocean circulation (Duplessy et al., 1988) and strength of biological pump (Curry & Oppo, 2005; Crucifix, 2005; Eide et al., 2017; Morée et al., 2018).

2.4 Phosphate Oxygen tracer (PO)

The phosphate oxygen tracer (PO) as defined by Broecker (1974) is a measure for identifying water masses. It is computed using the simulated phosphate and oxygen fields following

$$PO = O_2 + r_{O:P} PO_4 \quad (2)$$

where $r_{O:P}$ is the oxygen-to-phosphate stoichiometric ratio, which is varying from 138 (surface) to 170 (bottom), in the model. For a given water mass, this tracer is presumed to be approximately constant and is based on the principle that phosphate is released while oxygen is used during remineralization, and vice versa during biological production. The distinction of water masses using PO is useful for contrasting interior water

masses with very different surface PO values. Here, we mainly use PO to identify northern source water (NSW) and SSW masses in the deep ocean below 1000 m depth characterized by low and high PO values, respectively.

2.5 Apparent Oxygen Utilization (AOU)

The Apparent Oxygen Utilization (AOU) is a diagnostic biogeochemical tracer that provides an estimate of the amount of oxygen used since a water parcel was last at the surface and hypothetically fully saturated. It is computed according to:

$$AOU = O_2^{sat} - O_2 \tag{3}$$

where O_2^{sat} is the saturation value and O_2 is the *in situ* oxygen value calculated by the model. When a water parcel is advected to the interior, remineralization processes starts and consumes the oxygen. The older a water parcel, the more oxygen has been consumed by remineralization, hence AOU increases.

3 Results

Section 3.1 describes the simulated variability in $\delta^{13}C_{DIC}$ and AMOC strength, while a composite analysis opposing strong versus weak AMOC is discussed in Sect. 3.2. The mechanisms associated with the variability of the meridional overturning circulation are addressed in Sect. 3.3. In order to compare and contrast our simulation with data records, we focus our discussion to the locations of the two high-resolution proxy records MD03-2664 (Galaasen et al., 2014) and Integrated Ocean Drilling Program (IODP) Site U1304 (Hodell et al., 2009), which depict centennial-scale $\delta^{13}C$ perturbations during the LIG. The location of these two sites is shown for instance in Fig. 2a.

3.1 AMOC and $\delta^{13}C$ transient variability

The time series of simulated $\delta^{13}C_{DIC}$ at the two sediment core locations are shown in Fig. 2a. The absolute values of $\delta^{13}C_{DIC}$ generally differ from one location to the other by about 0.4 ‰, but converge during peaks in maximum values to a relative similar value (e.g., 116.8 and 117.8 ka). In addition, both MD03-2664 and U1304 sites show similar evolution during the transient simulation. While $\delta^{13}C_{DIC}$ is relatively stable from 125ka to 122ka (1.28 ± 0.05 ‰ at MD03-2664 and 0.96 ± 0.04 ‰ at U1304), stronger variations are simulated during the second half of the experiment where the standard deviation is increased by a factor of three at U1304 and two at MD03-2664. These abrupt changes in bottom $\delta^{13}C_{DIC}$ are simulated at centennial timescale for both locations and show a maximum amplitude of variation of about 0.65 and 0.43 ‰ around 119ka. This is comparable to the changes depicted by the proxy reconstruction at MD03-2664 (Galaasen et al., 2014), which also highlights similar centennial variations of about 0.7 ‰ of magnitude. In addition, small decreasing trend are simulated at MD03-2664 (3.2 10^{-5} ‰.yr^{-1}) and U1304 (3.5 10^{-5} ‰.yr^{-1}), which is attributed to the long-term decreasing trend of the atmospheric $\delta^{13}C$ and the decreasing land vegetation carbon reservoir.

The variations in bottom water $\delta^{13}C_{DIC}$ at both locations follows the same variations as depicted by AOU (Fig. 2b). Site U1304 simulates in general higher AOU (∼40%) than that at MD03-2664 suggesting that the water mass affecting Site U1304 is more remineralized than at MD03-2664. However, during the abrupt transitions the difference between both sites is reduced meaning that both sites are affected by a water mass which has been similarly ventilated (i.e., similar water mass).

Figure 2c shows the evolution of maximum overturning stream function at $27°N$ in the Atlantic basin with an averaged value of 12.2 ± 1.8 (one standard deviation) Sv and shows similar variations to those depicted with $\delta^{13}C_{DIC}$ and AOU. High values of overturning stream function coincide with high bottom water values of $\delta^{13}C_{DIC}$ at both

sediment core sites, which seem to converge toward the same $\delta^{13}C_{DIC}$ value. Conversely, a weak overturning stream function corresponds to lower values of $\delta^{13}C_{DIC}$ and lead to a divergence of $\delta^{13}C_{DIC}$ values between the two core locations. This suggests that the temporal variation of $\delta^{13}C_{DIC}$ in the North Atlantic is related mechanistically to, or even directly modulated by the strength of the AMOC in our model.

In order to further analyze the impact differences in AMOC strength have on the biogeochemistry and ocean $\delta^{13}C_{DIC}$ we show a composite analysis of two contrasting states of AMOC, i.e., weak versus strong AMOC. For this, we average all years where AMOC strength is two standard deviations above or below the long-term mean. The selected years with strong AMOC states are represented by the purple points (Fig. 2c; number of point "n" = 460), while the selected years with weak AMOC states are shown by the purple stars (n=63).

3.2 Composite analysis: weak vs strong AMOC

Figure 3 depicts the vertical structure of the AMOC, PO and $\delta^{13}C_{DIC}$ distribution along the Atlantic section. The left panels (Fig. 3a, c, e) correspond to the average values over weak AMOC years, whereas the right panels (Fig. 3b,d,f) correspond to the average over strong AMOC years. Under weak AMOC, the separation between the top and bottom cells of the overturning stream function reaches approximately 3000 m depth around the sediment core locations (Fig. 3a, black dashed-line). The maximum of the upper cell reaches 13.8 Sv, while the minimum of the bottom cell is about -8.1 Sv. During strong AMOC state, the upper cell is increased as high as 20.5 Sv and deepens by about 400 m depth down to 3400 m (Fig. 3b, black dashed-line), while the bottom cell contracts and becomes less vigorous. The blue (red) shade of the PO tracer illustrates the signature of NSW (SSW). NSW affects the region of the sediment cores more strongly when the AMOC is strong (Fig. 3c,d). This result is in good agreement with the deepening of the upper cell of the AMOC previously mentioned. We note that in both cases the NADW (NSW) is sustained depicting its relative PO signature down to 2300 (3000) m depth under weak (strong) AMOC state. In addition, because NSW has higher $\delta^{13}C_{DIC}$ values than SSW, $\delta^{13}C_{DIC}$-rich water masses dominate MD03-2664 and U1304 locations when the AMOC is strong (Fig. 3f), which is consistent with the convergence of $\delta^{13}C_{DIC}$ values at both core sites previously mentioned (Sect. 3.1). On the other hand, more low $\delta^{13}C_{DIC}$ water masses, resulting from the mixing of SSW and NSW, are affecting the sediment cores during periods of weaker AMOC (Fig. 3e).

These two AMOC states are characterized by distinct differences in the location, area and depth of convection in the North Atlantic. In the case of weak AMOC, deep convection is simulated in the Norwegian sea (>400 m depth, Fig. 4a), while an area of shallower convection extends further south into the North Atlantic. Conversely, under strong AMOC periods, the Irminger Sea region including the southeast Labrador Sea also experiences deep convection down to 150 m depth (Fig. 4b), while the convection depth in the Norwegian Sea slightly weakens to 300 m and extends further north under the sea-ice limit. The strongest sea-ice retreat (up to 10° northward) is simulated in the Irminger sea and coincides with the activation of convection in this region (Fig. 4, light blue dashed-lines). The changes depicted by the density field (Fig. 4c,d) correspond to the changes in convection depth. Under simulated weak AMOC, the densest water masses are in the Norwegian Sea with values of neutral density up to 27.8 kg.m^{-3} where the convection occurs. When the AMOC strengthens the surface density increases south of Greenland and in the Irminger Sea leading to similar density values with that in the Norwegian Sea (27.8 kg.m^{-3}, Fig. 4d). Thus, the total area of dense water formation in these regions increases during the AMOC strong composite state.

Figure 5 shows the annual mean surface temperature and salinity fields during both strong and weak AMOC states. It reveals that lower SSTs are simulated in the regions

corresponding to the subpolar gyre (Irminger Sea and southeast of the Labrador Sea) and in the Norwegian Sea when the AMOC weakens (Fig. 5a,b). For example, the 0°C isotherm shifts north by about 10° between Greenland and Norway while it only moves north by about 2° in southeastern Labrador Sea (Fig. 5b). On the other hand, the warmest waters expand westward (i.e., isotherm 8°C) when AMOC strengthens and onset/increase of convection in the Labrador/Irminger Seas. This suggests strong negative buoyancy flux in these regions due to the heat loss. The SSS field also depicts strong modification in the North Atlantic, especially in the region where the convection turns off and on (Fig. 5c,d). Under weak AMOC, the strongest SSS (>35.5 psu) are simulated around the Celtic Sea and extend northward toward the Norwegian Sea (Fig. 5c), while fresher polar surface waters (<33.6 psu) are being transported along the eastern Greenland coastline following the sea-ice extent. When the AMOC strengthens, the high surface salinity spreads further north into the Norwegian Sea and west toward the Irminger Sea and the entrance of the Labrador Sea (Fig. 5d). This suggests that more warm and salty surface Atlantic water is entering the Norwegian Sea under stronger ocean circulation and recirculates to the northwestern basin following the northward shift of the sea-ice edge between Greenland and Iceland (Fig. 5d). These increases in SSS cause the surface density to increase, reducing the stratification of the ocean and establishing favorable conditions for deep convection to occur.

While changes in AMOC are expressed clearly in $\delta^{13}C_{DIC}$ at both locations (Fig. 2a,c), the model predicts slightly different responses at these locations due to the position of the sites relative to major water mass pathways. MD03-2664 is located further North and West and is more influenced by NSW during both strong and weak AMOC composite states (Fig. 6e,f). Thus, during weak composite states bottom water $\delta^{13}C_{DIC}$ at MD03-2664 does not drop as low as at U1304, which has much greater influence of SSW than MD03-2664. Figure 6 reveals these differences by depicting the changes in $\delta^{13}C_{DIC}$, AOU and PO tracers at the sea floor. The pattern of these three tracers are strongly similar showing that $\delta^{13}C_{DIC}$ changes are related to water mass geometry. Under weak AMOC states, MD03-2664 depicts 105.0 μmol.kg^{-1} of AOU when U1304 has 146.1 μmol.kg^{-1} (Fig. 6c), corresponding to 28% of difference. This difference is reduced to 13% when the AMOC strengthens (Fig. 6d), i.e., the AOU values in MD03-2664 and U1304 depict 82.5 and 94.6 μmol.kg^{-1}, respectively. However, U1304 AOU values are generally higher than at MD03-2664, which suggests that the water mass affecting U1304 contains more remineralized carbon than at MD03-2664 during both strong/weak AMOC states. Consequently, the bottom water $\delta^{13}C_{DIC}$ values simulated at U1304 are lower compared to MD03-2664 and this difference is even more pronounced when the AMOC weakens (Fig. 2a). Finally, the PO tracer confirms that both sites are affected by different water masses under weak AMOC, while this difference strongly decreases when the ocean circulation strengthens. Thus, under weak AMOC, the MD03-2664 location depicts weaker PO value than at U1304 (Fig. 6e, 0.35 against 0.42 mol.m^{-3}, respectively), while almost the same values are depicted under strong AMOC (Fig. 6f, 0.32 against 0.34 mol.m^{-3}, respectively).

3.3 AMOC oscillations

Figure 7 shows the time series of the vertical density gradient for the region where the deep convection turns on and off. The oscillations of the density gradient south of Greenland covary with the AMOC strength during the centennial peak events. As the stratification decreases (density gradient weakens) the AMOC strength increases. In the model, this suggests that the stratification of the ocean south of Greenland is at least partially linked to the AMOC strength during these centennial peaks. The salinity field is the main driver for the changes in density at the surface. The amplitude of oscillations are weaker at the beginning of the simulation than toward 115ka. The lower values remain relatively constant around 0.5 10^{-3} kg.m^{-4} but the maximum values increase toward 115ka (up to 3.6.10^{-3} kg.m^{-4}), especially after 122 ka. This increasing trend in maximum of density gradient is attributed to fresher surface ocean simulated toward 115ka

in that area potentially induced by stronger variability in the growing-melting of sea-ice. Hence, the surface salinity in this region is in averaged 2 psu lower in the late LIG (116ka-115ka) than at the beginning (125ka-124ka). The variation of surface density are more than 6 times greater at the surface (27.86 $\pm$ 0.33 kg.m^{-3}) than at 600 m depth (27.12 $\pm$ 0.05 kg.m^{-3}) and are most likely also due to the sea-ice growth and retreat in this area.

In order to identify the mechanisms behind the changes in surface density, we analyze the onset and offset of the AMOC peak events. We focus on the event occurring around 116.7ka as an example because it corresponds to the strongest variation of both AMOC and $\delta^{13}C_{DIC}$, however, every oscillation depicted by Fig. 2c shows similar characteristics. We note yr_{min} as the year when the AMOC reaches its last minimum value before increasing ($\mathrm{yr}_{min} = 116.799$). Similarly, we note yr_{max} as the year when the AMOC reaches its last maximum value before decreasing and ending the strong AMOC peak event ($\mathrm{yr}_{max} = 116.657$, 142 years after yr_{min}).

Figure 8 depicts the salinity in latitudinal (left panels) and longitudinal (right panels) sections of the North Atlantic ocean. The first row represents the salinity of the first 1000 m depth in the North Atlantic ocean at yr_{min}. The second row represents the same sections at yr_{min}+11 years of simulation and the last row corresponds to the end of the onset peak at yr_{min}+18 years. These years represent well the changes in the water mass distribution associated to the multi-decadal initiation (and offset) of the abrupt transition. Showing any other years within this interval would provide similar results. At the onset of the AMOC peak (yr_{min}) the AMOC is at the minimum of 9.2 Sv. A 100 to 200 m layer of fresh water extends from the high latitudes down to almost $45°N$ and spreads from the Greenland coast eastward to $25°W$ leading to a stratified ocean surface (Fig. 8, first row panels). This fresh water is associated to sea-ice cover. The Atlantic water corresponds to the higher salinity at $45°N$ below 200 m depth (Fig. 8). It extents northward along the Norwegian coast and depicts salinity >35.75 psu. At yr_{min}+11 (panels on the second row), the volume of fresh water east of the Greenland coast reduces and starts retreating northward. Similarly the salinity increases from the eastern side and traces of convection begin to appear around $25°W$, mixing the salinity through the water column. Hence, the AMOC slightly speeds up and increases by +1.7 Sv to reach 10.9 Sv. At the end of the onset (yr_{min}+18), the AMOC is near its maximum (16.7 Sv) and the salinity north of $60°N$ increases. By contrast, between 50-55$°N$ the surface water is simulated fresher and may be associated to the transport of the fresh water from the sea-ice melt. The intrusion of salty water mass seems to originate from the eastern side of the basin where the saline Atlantic waters expand from the Norwegian coast toward the Greenland coastline. As a result, saline Atlantic waters fill up the basin along the $61.5°N$ latitude band creating favorable conditions for convection south of Greenland. The same ocean structure is simulated during the time of the maximum AMOC, which corresponds to a 124 years window. Figure 9 is similar to Fig. 8, but represents the offset of the AMOC peak, from yr_{max} to the next minimum (yr_{max}+14). This decreasing AMOC phase (increasing stability) mirrors the phase of increasing AMOC (decreasing stability) and shows a gradual establishment of the freshwater layer associated with sea-ice growth. No significant differences compared to the onset could be identified.

4 Discussion

The Ocean circulation is one of the key processes affecting the ocean carbon storage, hence regulating the atmospheric CO_2 levels on millennial timescale. The production of NADW during the Last Interglacial is vigorous and appears relatively robust at (multi)millennial timescales, i.e., suggested by numerous of studies. However new high-resolution proxy records reveal that abrupt changes in bottom water chemistry ($\delta^{13}C$) occurred on centennial timescales during the previous interglacial and are postulated to represent ocean circulation changes. Yet, it is less clear how these circulation changes relate to AMOC or, indeed, even if deep circulation changes could explain such rapid changes

in deep Atlantic $\delta^{13}C$ — onset and terminated in decade(s) and generally persisting for one or few centuries (Galaasen et al., 2014). In this study, we simulate a transient experiment from the last interglacial period (125ka – 115ka) using an Earth system model of intermediate complexity (EMIC) allowing the computation of $\delta^{13}C_{DIC}$, an oceanic tracer for the ocean circulation and biogeochemical processes used in paleoclimate reconstruction. Significant changes of $\delta^{13}C_{DIC}$ are simulated in the North Atlantic at short timescale (centennial), which approach in magnitude those depicted in the data reconstruction. Likewise, the transitions (increases and decreases) also occur quickly, consistent with the rapid onset and demise observed in the proxy reconstruction. The variability in bottom water $\delta^{13}C_{DIC}$ is found to be positively correlated to the AMOC strength, which oscillates between 6.3 to 19.3 Sv. These AMOC oscillations are mainly controlled by the convection south of Greenland (Labrador and Irminger Seas) which turns off and on with the northward and westward expansion of highly saline Atlantic waters from the Norwegian coast to Greenland around $60°N$, associated with the northward retreat of sea-ice and fresh surface waters.

The representation of the North Atlantic ventilation is coherent with that suggested by previous studies. The mid-depth North Atlantic water remains relatively well ventilated during the entire period of simulation, even during the simulated weak AMOC events (Fig. 3c). This persistent production of NSW at mid-depth from 125ka to 115ka is also suggested by other studies based on proxy reconstructions (McManus et al., 2002; Mokeddem et al., 2014) and previous independent model simulations (Wang & Mysak, 2002; Born et al., 2011). Moreover, our results also support previous interpretations of proxy data concerning the deep North Atlantic water (Hodell et al., 2009; Galaasen et al., 2014), i.e., that ventilation of the deep Atlantic was intermittently disturbed during the LIG and that AMOC strength and NSW-SSW shifts could plausibly explain North Atlantic deep water $\delta^{13}C$ changes during interglacials. Thereby, as shown in Galaasen et al. (2020), the simulated deep Atlantic $\delta^{13}C_{DIC}$ anomalies are strongly similar in magnitude (0.5-0.7 ‰) and temporal characteristics (decadal scale at onset and persisting for centuries) to the variability in high-resolution $\delta^{13}C$ reconstructions. Assuming that the reconstructed proxies reasonably capture the core top $\delta^{13}C$ values, our model simulation suggests that the region south of Greenland would be most suitable to capture any apparent variations in the watermass properties over the LIG period while regions located further North and East (e.g., in the Nordic Seas) remains more stable. Figure 10 highlights this point by showing higher bottom water $\delta^{13}C_{DIC}$ standard deviation south of Greenland as compared to any other regions of the North Atlantic. In our simulation, when AMOC is strong, both sediment core sites are affected by the same water mass (NSW) with similar biophysical properties leading to similar $\delta^{13}C_{DIC}$ values. Conversely, when AMOC weakens the influence of SSW at Site U1304 increases, hence the $\delta^{13}C_{DIC}$ values of both locations diverge. This suggests that relatively large differences in tracer ($\delta^{13}C$) signals between two cores located in relatively close proximity can occur due to the changes in water mass distributions (NSW vs SSW). Using the same model for the period 132ka-120ka, Bakker et al. (2015) have also shown a close correlation between North Atlantic bottom water $\delta^{13}C_{DIC}$ and AMOC strength on multi-millennial timescale. Our study further support this result on (multi)centennial timescale.

In addition to those rapid shifts, the proxy data records from MD03-2664 and Site U1304 show markedly different long-term trends in bottom water $\delta^{13}C$ from 122ka to 115ka (see figure 3 in Galaasen et al., (2014)). While bottom water $\delta^{13}C$ at MD03-2664 increases through the late LIG, it decreases at Site U1304 resulting in a gradient of $\sim$ 0.4 ‰ between the western (MD03-2664) and eastern subpolar basins (Site U1304) near 115ka and the last glacial inception. In our model simulation, the long-term transient trends deviate somewhat from the actual sites and show at both location a small decreasing trend. This discrepancy with data reconstruction can be attributed, at least in part, to the coarse spatial resolution of the model and the difficulty to properly simulate overflows in this region. However, much of our model simulation shows deep North Atlantic

$\delta^{13}C_{DIC}$ gradient of ~ 0.4 ‰ between MD03-2664 and Site U1304 (Fig. 2a) similar to the proxy records toward 115ka. In the model, this difference is caused by relatively higher influence of SSW in the eastern basin and Site U1304 (Fig. 6e), which is restricted by the bathymetry from entering the western basin. Therefore, we suggest that the observed ~ 0.4 ‰ $\delta^{13}C$ gradient for the late LIG could be explained from such water mass geometry state, i.e., the expansion of the SSW into the subpolar North Atlantic in the late LIG (Govin et al., 2009).

While similar in character, the forcing of the centennial-scale LIG variability likely differs between the simulated and reconstructed events. The reconstructed variability focuses around the early phase of the LIG and appears closely associated with discharge of freshwater and icebergs, including a freshwater outburst flood event associated with the final retreat of the Laurentide ice sheet (Hodell et al., 2009; Nicholl et al., 2012; Galaasen et al., 2014). In the model, the variability occurs in the mid to late LIG and is associated with changes in the distribution of sea ice and freshwater within the subpolar North Atlantic and Nordic Seas. This discrepancy from the proxy data arises mainly from the initial conditions used to begin the transient simulation — equilibrium state at 125ka — which removes potential effects from reminiscent glacial conditions especially at the beginning of the simulation. Hence, the simulated absolute values of $\delta^{13}C_{DIC}$ may not correspond to the reality from that period. However, the climate response to orbital and greenhouse gases forcings remain sufficient to create large modifications in the interior ocean carbon distribution and water mass geometry, which comes to support the short-lived large perturbations of the climate system under warmer climate conditions than today. These rapid shifts in deep water occur as the internal ocean adjusts to switches in AMOC strength. These shifts in AMOC strength are due to changes in surface ocean convection sites and in particular involve turning on and off convection in the Nordic Seas. Similar variations in overturning geometry and strength tied to the location and strength of deep convection have been invoked previously in particular to explain abrupt, millennial-scale ocean-climate changes observed during the last glacial cycle (Rahmstorf, 2002). Our simulation provides an example of how similar shifts in convection-AMOC strength could explain centennial scale variability seen in proxy records during interglacial boundary conditions.

The multi-centennial scale variability of AMOC simulated by our model is closely linked to the occurrence of deep convection events south of Greenland. Here, transport of anomalously saline subsurface water mass leads to a strong AMOC strength while fresher water leads to weaker AMOC. The importance of salinity as well as the magnitude and timescale of the AMOC changes shown here are consistent with previous studies applying ECBilt-CLIO coupled model (Jongma et al., 2007) and LOVECLIM (Friedrich et al., 2010), albeit they use slightly different boundary conditions. Furthermore, our simulation shares some important features with Friedrich et al. (2010) regarding the behaviour of AMOC oscillations and the mechanisms involved in it. Among them is the AMOC preferentially operating at weak state toward 115ka when the obliquity reduces to 22.4 and its related increase of large abrupt AMOC change occurrences during the second half of the LIG, but also changes of the Greenland Iceland Norwegian (GIN) sea overturning circulations (not shown here) ahead of the total AMOC changes. However, our simulation do not show any deep-decoupling from subsurface temperature increase responsible for the AMOC increase, as shown in Friedrich et al. (2010), but rather atmospheric temperature anomalies above the sea level (up to 10 K, not shown here) inducing wind stress anomalies favorable to transporting anomalously saline water south of Greenland as mentioned in Schulz et al. (2007). Here the origin of density changes and the subsequent activation of deep convection comes rather from a surface salinity change. Hence the salinity remains to be one of the key factor in triggering the deep convection areas that switches the AMOC from weak to stronger states, the mechanisms behind their origin remain however partially unclear. Further sensitivity experiments are needed in or-

der to fully diagnose the mechanisms responsible for the fresh versus saline water shifts south of Greenland.

5 Conclusion

Recent high-resolution proxy records reveal that abrupt changes in bottom water chemistry ($\delta^{13}C$) occurred on centennial timescales during the previous interglacial and are postulated to represent ocean circulation changes, thus challenging the paradigm of interglacial thermohaline circulation stability at short timescale (Hodell et al., 2009; Galaasen et al., 2014). In this study, we use the iLOVECLIM Earth system model of intermediate complexity to simulate a transient experiment of the Last Interglacial period from 125ka to 115ka to analyze possible mechanisms behind these short-lived disturbances depicted by the $\delta^{13}C$ data reconstruction from that period.

Our simulation depicts large perturbations of bottom water $\delta^{13}C_{DIC}$ up to 0.43 ‰ and 0.65 ‰ in the North Atlantic at the locations corresponding to the sediment core sites MD03-2664 (Eirik Drift) and U1304 Site (Gardar Drift), respectively. These variations are strongly similar in magnitude (0.5-0.7 ‰) and temporal characteristics (multi-decadal scale at onset and persisting for centuries) to the variability in high-resolution $\delta^{13}C$ reconstruction. The simulated $\delta^{13}C_{DIC}$ at both sites generally differ by about 0.4 ‰, similar to the $\delta^{13}C$ gradient observed in the subpolar North Atlantic during the late LIG. In the model, this gradient is attributed to the relative influence of northern source water (NADW) versus southern source water (SSW) to the sediment core locations. However, during the centennial scales perturbations the simulated bottom water $\delta^{13}C_{DIC}$ values converge toward the same values, suggesting that similar water mass properties could potentially be affecting both sites, which is confirmed by our PO analysis.

The simulated variations in $\delta^{13}C_{DIC}$ at MD03-2664 and U1304 Site are correlated to the variations in AMOC strength, which ranges from 6.3 to 19.3 Sv. High values of bottom $\delta^{13}C_{DIC}$ correspond to strong AMOC and vice versa. Consequently, a simulated strong AMOC state leads to similar bottom water $\delta^{13}C_{DIC}$ values at both locations (i.e., affected by the same water mass — NADW), while when the AMOC decreases the influence of SSW at U1304 Site increases. These large AMOC differences are linked to the activation and deactivation of convection areas south of Greenland, highlighting the importance of NADW production in this region and its role in redistributing $\delta^{13}C_{DIC}$ in the interior ocean.

In our model simulation, the mechanism associated to the activation and deactivation of the convection south of Greenland and therefore the AMOC strength is related to a weakening of the vertical density gradient mainly induced by the surface salinity in this region, which increases and decreases along with the sea-ice and associated freshwater extension. Northward intrusions of warm and saline Atlantic water into the Nordic Seas also gradually expand westward from $25°W$ toward the Greenland coast. In turn, the sea-ice and associated freshwater surface layer retreats (up to $\sim 10°$ northward) and the advected saline surface water increases the surface density. This sets favorable conditions for deep convection to occur, initiating the AMOC increase.

While the deep Atlantic $\delta^{13}C_{DIC}$ changes seen in our model simulation and the proxy data are similar in magnitude and temporal characteristics, several discrepancies and differences can be mentioned. The use as initial conditions of the equilibrium at 125ka state sets different climate background than it may have been in reality. Consequently, (1) the absolute values of bottom water $\delta^{13}C_{DIC}$ are generally simulated higher than that depicted by the data reconstructions, and (2) the simulation does not reproduce the abrupt variations during the early LIG, potentially due to the lack effects from the final retreat of glacial ice sheet remnants (Nicholl et al., 2012). In addition, our model simulates similar decreasing long-term trends at both sediment core locations which do not correspond

to what is observed in the data records depicting different trends at both locations. This is attributed to the simulated strong decline of the land vegetation carbon content (∼420 PgC) towards 115ka and the associated decrease in atmospheric $\delta^{13}C$. Hence, terrestrial vegetation content seems to play an important role in setting the ocean $\delta^{13}C_{DIC}$ absolute values, which has also been highlighted for glacial periods (Menviel et al., 2017). Finally, the abrupt transitions occur when the model switches from a strong AMOC state (early LIG) to a weak state (late LIG) and are likely associated to the cooling (i.e., sea-ice/freshwater forcings) towards the glacial inception at 115ka, which differs from future projected climate. Additional experiments need to be performed in order to properly address the internal mechanisms shaping the frequency and occurrence of these abrupt transitions. In the model, the typical changes in atmospheric CO_2 associated with these abrupt transitions are approximately of 7 ppm, which is in the range of the CO_2 variation observed in the data reconstruction from that period (Lourantou et al., 2010; Schneider et al., 2013), while the changes in ocean DIC are of about 15 PgC and compensated by a 30 PgC increase in the land vegetation carbon.

This study underlines that during the LIG the Labrador and Irminger Seas may have been sensitive to density changes altering the strength of the AMOC over several decades by simple natural greenhouse gases and orbital forcings, hence affecting the distribution of bottom water $\delta^{13}C_{DIC}$. These unforced oscillations may be specific to our simulation and do not exclude other potential mechanism that may be responsible for abrupt and large changes of bottom water $\delta^{13}C$ depicted in some marine records. The stronger amplitude of change in $\delta^{13}C_{DIC}$ at U1304 Site as compared to MD03-2664 potentially reveals this location at a better indicator for AMOC structure and/or strength change. In addition, we highlight the need for more isotope enabled model simulations over interglacial periods in order to better constrain and link changes observed in the marine records and potential changes in overturning circulation.

Acknowledgments

We thanks the two anonymous referees for their positive and constructive comments, which helped to clarify the manuscript. We also thanks the Editor Stephen Barker for the time he dedicated in processing our manuscript and his additional feedback. This work was supported by the Research Council of Norway funded project THRESHOLDS (254964) and ORGANIC (239965) and Bjerknes Centre for Climate Research project BIGCHANGE. We acknowledge the Norwegian Metacenter for Computational Science and Storage Infrastructure (Notur/Norstore) projects nn1002k, and ns1002k for providing the computing and storing resources essential for this study. The authors declare no conflict of interest.The model data are available on the Norwegian Research Data Archive server (https://doi.org/10.11582/201
Kessler (2019)).

References

Adkins, J. F., Boyle, E. A., Keigwin, L., & Cortijo, E. (1997). Variability of the north atlantic thermohaline circulation during the last interglacial period. *Nature*, *390*(6656), 154. doi: 10.1038/36540

Bakker, P., Govin, A., Thornalley, D. J., Roche, D. M., & Renssen, H. (2015). The evolution of deep-ocean flow speeds and δ13c under large changes in the atlantic overturning circulation: Toward a more direct model-data comparison. *Paleoceanography*, *30*(2), 95–117.

Bakker, P., Schmittner, A., Lenaerts, J., Abe-Ouchi, A., Bi, D., van den Broeke, M., ... others (2016). Fate of the atlantic meridional overturning circulation: Strong decline under continued warming and greenland melting. *Geophysical Research Letters*, *43*(23), 12–252. doi: 10.1002/2016GL070457

Bauch, H. A., Kandiano, E. S., Helmke, J., Andersen, N., Rosell-Mele, A., & Erlenkeuser, H. (2011). Climatic bisection of the last interglacial warm period in

the polar north atlantic. *Quaternary Science Reviews*, *30*(15-16), 1813–1818. doi: 10.1016/j.quascirev.2011.05.012

Berger, A., Crucifix, M., Hodell, D., Mangili, C., J.F.McManus, Otto-Blisner, B., ... Vázquez Riveiros, N. (2015, 11). Interglacials of the last 800,000 years. *Reviews of Geophysics*. doi: 10.1002/2015RG000482

Born, A., Nisancioglu, K. H., & Risebrobakken, B. (2011). Late eemian warming in the nordic seas as seen in proxy data and climate models. *Paleoceanography*, *26*(2). doi: 10.1073/pnas.1322103111

Bouttes, N., Paillard, D., & Roche, D. (2010). Impact of brine-induced stratification on the glacial carbon cycle, clim. past, 6, 575–589. *Clim. Past*, *6*, 575–589. doi: 10.5194/cp-6-575-2010

Bouttes, N., Paillard, D., Roche, D., Waelbroeck, C., Kageyama, M., Lourantou, A., ... Bopp, L. (2012). Impact of oceanic processes on the carbon cycle during the last termination. *Clim. Past*, *8*, 149–170.

Bouttes, N., Roche, D., Mariotti, V., & Bopp, L. (2015). Including an ocean carbon cycle model into iloveclim (v1. 0),. *Geosci. Model Dev.*, *8*, 1563–1576. doi: 10.5194/gmd-8-1563-2015

Bouttes, N., Roche, D., & Paillard, D. (2009). Impact of strong deep ocean stratification on teh glacial carbon cycle, paleooceanography, 24, pa3202. *Paleoceanography*, *24*(3). doi: 10.1029/2008PA001707

Broecker, W. S. (1974). "no", a conservative water-mass tracer. *Erath. Planet. Sc. Lett.*, *23*, 100–107. doi: 10.1016/0012821X(74)90036-3

Brovkin, V., Ganopolski, A., Archer, D., & Rahmstorf, S. (2007). Lowering of glacial atmospheric co2 in response to changes in oceanic circulation and marine biogeochemistry. *Paleoceanography*, *22*(4). doi: 10.1029/2006PA001380

Brovkin, V., Ganopolski, A., & Svirezhev, Y. (1997). A continuous climate-vegetation classification for use in climate-biosphere studies. *Ecological Modelling*, *101*(2-3), 251–261. doi: 10.1016/S0304-3800(97)00049-5

Caesar, L., Rahmstorf, S., Robinson, A., Feulner, G., & Saba, V. (2018). Observed fingerprint of a weakening atlantic ocean overturning circulation. *Nature*, *556*(7700), 191. doi: 10.1038/s41586-018-0006-5

Campin, J.-M., & Goosse, H. (1999). Parameterization of density-driven downsloping flow for a coarse-resolution ocean model in z-coordinate. *Tellus A*, *51*(3), 412–430. doi: 10.1034/j.1600-0870.1999.t01-3-00006.x

Craig, H. (1957). Isotopic standards for carbon and oxygen and correction factors for mass-spectrometric analysis of carbon dioxide. *Geochimica et cosmochimica acta*, *12*(1-2), 133–149. doi: 10.1016/0016-7037(57)90024-8

Crucifix, M. (2005). Distribution of carbon isotopes in the glacial ocean: a model study. *Paleoceanography*, *20*(4). doi: 10.1029/2005PA001131

Curry, W. B., & Oppo, D. W. (2005). Glacial water mass geometry and the distribution of δ13c of σco2 in the western atlantic ocean. *Paleoceanography*, *20*(1). doi: 10.1029/2004PA001021

Duplessy, J., Shackleton, N., Fairbanks, R., Labeyrie, L., Oppo, D., & Kallel, N. (1988). Deepwater source variations during the last climatic cycle and their impact on the global deepwater circulation. *Paleoceanography*, *3*(3), 343–360. doi: 10.1029/PA003i003p00343

Eide, M., Olsen, A., Ninnemann, U. S., & Johannessen, T. (2017). A global ocean climatology of preindustrial and modern ocean δ13c. *Global Biogeochemical Cycles*, *31*(3), 515–534. doi: 10.1002/2016GB005473

Fichefet, T., & Maqueda, M. M. (1997). Sensitivity of a global sea ice model to the treatment of ice thermodynamics and dynamics. *Journal of Geophysical Research: Oceans*, *102*(C6), 12609–12646. doi: 10.1029/97JC00480

Fichefet, T., & Maqueda, M. M. (1999). Modelling the influence of snow accumulation and snow-ice formation on the seasonal cycle of the antarctic sea-ice cover. *Climate Dynamics*, *15*(4), 251–268. doi: 10.1007/s003820050280

Friedrich, T., Timmermann, A., Menviel, L., Elison Timm, O., Mouchet, A., & Roche, D. (2010). The mechanism behind internally generated centennial-to-millennial scale climate variability in an earth system model of intermediate complexity. *Geoscientific Model Development*, *3*(2), 377–389. doi: 10.5194/gmd-3-377-2010

Galaasen, E. V., Ninnemann, U., Irvalı, N., Kleiven, H., & Kissel, C. (2015). deep atlantic variability during the last interglacial period. *GLACIAL TERMINATIONS AND INTERGLACIALS*, *328*, 20.

Galaasen, E. V., Ninnemann, U. S., Irvalı, N., Kleiven, H. K. F., Rosenthal, Y., Kissel, C., & Hodell, D. A. (2014). Rapid reductions in north atlantic deep water during the peak of the last interglacial period. *Science*, *343*(6175), 1129–1132. doi: 10.1126/science.1248667

Galaasen, E. V., Ninnemann, U. S., Kessler, A., Irvalı, N., Rosenthal, Y., Tjiputra, J., ... Hodell, D. A. (2020). Interglacial instability of north atlantic deep water ventilation. *Science*, *367*(6485), 1485–1489. doi: 10.1126/science.aay6381

Ganachaud, A., & Wunsch, C. (2000). Improved estimates of global ocean circulation, heat transport and mixing from hydrographic data. *Nature*, *408*(6811), 453. doi: 10.1038/35044048

Goosse, H., Brovkin, V., Fichefet, T., Haarsma, R., Huybrechts, P., Jongma, J., ... others (2010). Description of the earth system model of intermediate complexity loveclim version 1.2. *Geoscientific Model Development*, *3*, 603–633. doi: 10.5194/gmd-3-603-2010

Goosse, H., & Fichefet, T. (1999). Importance of ice-ocean interactions for the global ocean circulation: A model study. *Journal of Geophysical Research: Oceans*, *104*(C10), 23337–23355. doi: 10.1029/1999JC900215

Govin, A., Michel, E., Labeyrie, L., Waelbroeck, C., Dewilde, F., & Jansen, E. (2009). Evidence for northward expansion of antarctic bottom water mass in the southern ocean during the last glacial inception. *Paleoceanography*, *24*(1). doi: 10.1029/2008PA001603

Henry, L., McManus, J., Curry, W., Roberts, N., Piotrowski, A., & Keigwin, L. (2016). North atlantic ocean circulation and abrupt climate change during the last glaciation. *Science*, *353*(6298), 470–474. doi: 10.1126/science.aaf5529

Hodell, D. A., Minth, E. K., Curtis, J. H., McCave, I. N., Hall, I. R., Channell, J. E., & Xuan, C. (2009). Surface and deep-water hydrography on gardar drift (iceland basin) during the last interglacial period. *Earth and Planetary Science Letters*, *288*(1-2), 10–19. doi: 10.1016/j.epsl.2009.08.040

Hoffman, J. S., Clark, P. U., Parnell, A. C., & He, F. (2017). Regional and global sea-surface temperatures during the last interglaciation. *Science*, *355*(6322), 276–279. doi: 10.1126/science.aai8464

Jongma, J., Prange, M., Renssen, H., & Schulz, M. (2007). Amplification of holocene multicentennial climate forcing by mode transitions in north atlantic overturning circulation. *Geophysical Research Letters*, *34*(15). doi: 10.1029/2007GL030642

Kessler, A. (2019). Lig_transient_125ka-115ka [data set]. *Norstore*. doi: 10.11582/2019.00037

Kessler, A., Galaasen, E. V., Ninnemann, U. S., & Tjiputra, J. (2018). Ocean carbon inventory under warmer climate conditions–the case of the last interglacial. *Climate of the Past*, *14*(12), 1961–1976. doi: 10.5194/cp-14-1961-2018

Kopp, R. E., Simons, F. J., Mitrovica, J. X., Maloof, A. C., & Oppenheimer, M. (2009). Probabilistic assessment of sea level during the last interglacial stage. *Nature*, *462*(7275), 863. doi: 10.1038/nature08686

Lourantou, A., Chappellaz, J., Barnola, J.-M., Masson-Delmotte, V., & Raynaud, D. (2010). Changes in atmospheric co2 and its carbon isotopic ratio during the penultimate deglaciation. *Quaternary Science Reviews*, *29*(17-18), 1983–1992.

doi: 10.1016/j.quascirev.2010.05.002

Lynch-Stieglitz, J., Stocker, T. F., Broecker, W. S., & Fairbanks, R. G. (1995). The influence of air-sea exchange on the isotopic composition of oceanic carbon: Observations and modeling. *Global Biogeochemical Cycles*, *9*(4), 653–665. doi: 10.1029/95GB02574

McManus, J. F., Francois, R., Gherardi, J.-M., Keigwin, L. D., & Brown-Leger, S. (2004). Collapse and rapid resumption of atlantic meridional circulation linked to deglacial climate changes. *Nature*, *428*(6985), 834–837. doi: 10.1038/nature02494

McManus, J. F., Oppo, D. W., & Cullen, J. L. (1999). A 0.5-million-year record of millennial-scale climate variability in the north atlantic. *science*, *283*(5404), 971–975. doi: 10.1126/science.283.5404.971

McManus, J. F., Oppo, D. W., Keigwin, L. D., Cullen, J. L., & Bond, G. C. (2002). Thermohaline circulation and prolonged interglacial warmth in the north atlantic. *Quaternary Research*, *58*(1), 17–21. doi: 10.1006/qres.2002.2367

Menviel, L., Yu, J., Joos, F., Mouchet, A., Meissner, K., & England, M. (2017). Poorly ventilated deep ocean at the last glacial maximum inferred from carbon isotopes: A data-model comparison study. *Paleoceanography*, *32*(1), 2–17. doi: 10.1002/2016PA003024

Millero, F. J. (1995). Thermodynamics of the carbon dioxide system in the oceans. *Geochimica et Cosmochimica Acta*, *59*(4), 661–677. doi: 10.1016/0016-7037(94)00354-O

Mokeddem, Z., McManus, J. F., & Oppo, D. W. (2014). Oceanographic dynamics and the end of the last interglacial in the subpolar north atlantic. *Proceedings of the National Academy of Sciences*, *111*(31), 11263–11268. doi: 10.1073/pnas.1322103111

Morée, A. L., Schwinger, J., & Heinze, C. (2018). Southern ocean controls of the vertical marine δ 13 c gradient–a modelling study. *Biogeosciences*, *15*(23), 7205–7223. doi: 10.5194/bg-15-7205-2018

Nicholl, J. A., Hodell, D. A., Naafs, B. D. A., Hillaire-Marcel, C., Channell, J. E., & Romero, O. E. (2012). A laurentide outburst flooding event during the last interglacial period. *Nature Geoscience*, *5*(12), 901. doi: 10.1038/ngeo1622

Ninnemann, U. S., & Charles, C. D. (2002). Changes in the mode of southern ocean circulation over the last glacial cycle revealed by foraminiferal stable isotopic variability. *Earth and Planetary Science Letters*, *201*(2), 383–396. doi: 10.1016/S0012-821X(02)00708-2

Oppo, D. W., Horowitz, M., & Lehman, S. J. (1997). Marine core evidence for reduced deep water production during termination ii followed by a relatively stable substage 5e (eemian). *Paleoceanography*, *12*(1), 51–63. doi: 10.1029/96PA03133

Opsteegh, J., Haarsma, R., Selten, F., & Kattenberg, A. (1998). Ecbilt: A dynamic alternative to mixed boundary conditions in ocean models. *Tellus A: Dynamic Meteorology and Oceanography*, *50*(3), 348–367. doi: 10.3402/tellusa.v50i3.14524

Otto-Bliesner, B. L., Marshall, S. J., Overpeck, J. T., Miller, G. H., Hu, A., et al. (2006). Simulating arctic climate warmth and icefield retreat in the last interglaciation. *science*, *311*(5768), 1751–1753. doi: 10.1126/science.1120808

Otto-Bliesner, B. L., Rosenbloom, N., Stone, E. J., McKay, N. P., Lunt, D. J., Brady, E. C., & Overpeck, J. T. (2013). How warm was the last interglacial? new model–data comparisons. *Philosophical Transactions of the Royal Society A: Mathematical, Physical and Engineering Sciences*, *371*(2001), 20130097. doi: 10.1098/rsta.2013.0097

Rahmstorf, S. (2002). Ocean circulation and climate during the past 120,000 years. *Nature*, *419*(6903), 207. doi: 10.1038/nature01090

Roche, D., Dokken, T., Goosse, H., Renssen, H., & Weber, S. (2007). Climate of the

last glacial maximum: sensitivity studies and model-data comparison with the loveclim coupled model. *Clim. Past*(3), 205–224. doi: 10.5194/cp-3-205-2007

Schmittner, A., Gruber, N., Mix, A. C., Key, R. M., Tagliabue, A., & Westberry, T. K. (2013). Biology and air-sea gas exchange controls on the distribution of carbon isotope ratios (delta c-13) in the ocean. *Biogeosciences*, *10*(9), 5793–5816. doi: 10.5194/bg-10-5793-2013

Schneider, R., Schmitt, J., Köhler, P., Joos, F., & Fischer, H. (2013). A reconstruction of atmospheric carbon dioxide and its stable carbon isotopic composition from the penultimate glacial maximum to the last glacial inception. *Climate of the Past*, *9*(6), 2507–2523. doi: 10.5194/cp-9-2507-2013

Schulz, M., Prange, M., & Klocker, A. (2007). Low-frequency oscillations of the atlantic ocean meridional overturning circulation in a coupled climate model. *Climate of the Past*, *3*(1), 97–107. doi: 10.5194/cp-3-97-2007

Schurgers, G., Mikolajewicz, U., Gröger, M., Maier-Reimer, E., Vizcaíno, M., & Winguth, A. (2006). Dynamics of the terrestrial biosphere, climate and atmospheric co 2 concentration during interglacials: a comparison between eemian and holocene. *Climate of the Past*, *2*(2), 205–220. doi: 10.5194/cp-2-205-2006

Six, K. D., & Maier-Reimer, E. (1996). Effects of plankton dynamics on seasonal carbon fluxes in an ocean general circulation model. *Global Biogeochemical Cycles*, *10*(4), 559–583. doi: 10.1029/96GB02561

Smeed, D., McCarthy, G., Cunningham, S., Frajka-Williams, E., Rayner, D., Johns, W. E., ... others (2014). Observed decline of the atlantic meridional overturning circulation 2004–2012. *Ocean Science*, *10*(1), 29–38. doi: 10.5194/os-10-29-2014

Stocker, T. F., Qin, D., Plattner, G.-K., Tignor, M. M., Allen, S. K., Boschung, J., ... Midgley, P. M. (2014). *Climate change 2013: The physical science basis. contribution of working group i to the fifth assessment report of ipcc the intergovernmental panel on climate change.* Cambridge University Press. doi: 10.1017/CBO9781107415324

Tzedakis, P., Drysdale, R. N., Margari, V., Skinner, L. C., Menviel, L., Rhodes, R. H., ... others (2018). Enhanced climate instability in the north atlantic and southern europe during the last interglacial. *Nature communications*, *9*(1), 1–14. doi: 10.1038/s41467-018-06683-3

Van Nieuwenhove, N., Bauch, H. A., Eynaud, F., Kandiano, E., Cortijo, E., & Turon, J.-L. (2011). Evidence for delayed poleward expansion of north atlantic surface waters during the last interglacial (mis 5e). *Quaternary Science Reviews*, *30*(7-8), 934–946. doi: 10.1016/j.quascirev.2011.01.013

Wang, Z., & Mysak, L. A. (2002). Simulation of the last glacial inception and rapid ice sheet growth in the mcgill paleoclimate model. *Geophysical Research Letters*, *29*(23), 17–1. doi: 10.1029/2002GL015120

Weijer, W., Cheng, W., Drijfhout, S., Fedorov, A., Hu, A., Jackson, L., ... Zhang, J. (2019). Stability of the atlantic meridional overturning circulation: A review and synthesis. *Journal of Geophysical Research: Oceans*. doi: 10.1029/2019JC015083

Zeebe, R. E., & Wolf-Gladrow, D. (2001). *Co2 in seawater: equilibrium, kinetics, isotopes* (No. 65). Gulf Professional Publishing.

Zhang, J., Quay, P., & Wilbur, D. (1995). Carbon isotope fractionation during gas-water exchange and dissolution of co2. *Geochimica et Cosmochimica Acta*, *59*(1), 107–114. doi: 10.1016/0016-7037(95)91550-D

Zhuravleva, A., & Bauch, H. A. (2018). Last interglacial ocean changes in the bahamas: climate teleconnections between low and high latitudes. *Climate of the Past*, *14*(10), 1361–1375. doi: 10.5194/cp-14-1361-2018

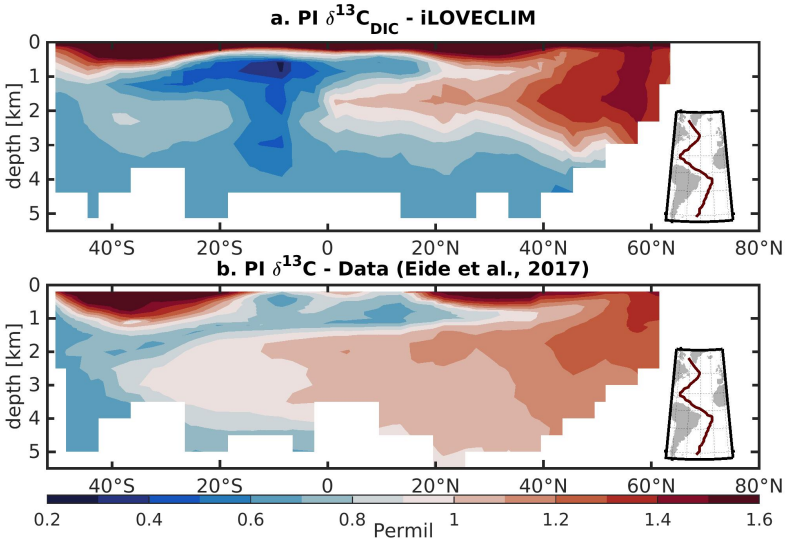

Figure 1. Atlantic section of preindustrial $\delta^{13}C$ (a) simulated by iLOVECLIM ($\delta^{13}C_{DIC}$) and (b) data reconstruction (Eide et al., 2017)

847

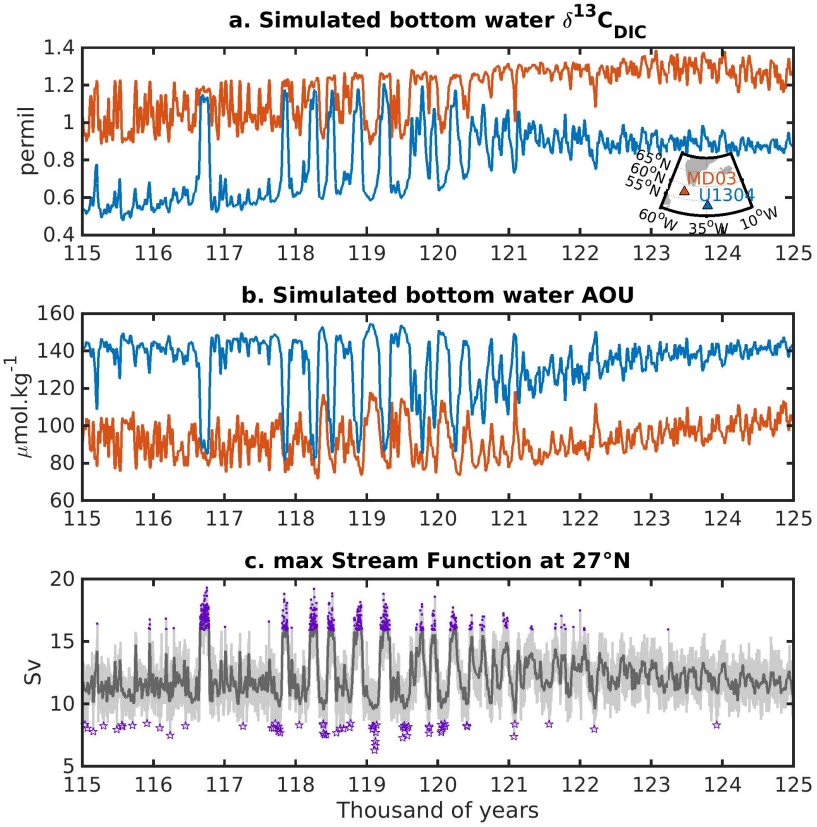

Figure 2. MD03 and U1304 sediment core locations time series of (a) bottom water $\delta^{13}C_{DIC}$, (b) AOU, and (c) maximum overturning stream function at $27°N$ of the North Atlantic. The locations of both sediment cores is shown on the map panel (a). The purple points (stars) represent the years where the maximum stream function is two standard deviations above (below) the long-term mean. A locally weighted linear regression over 40 years is used and shown by the thick lines.

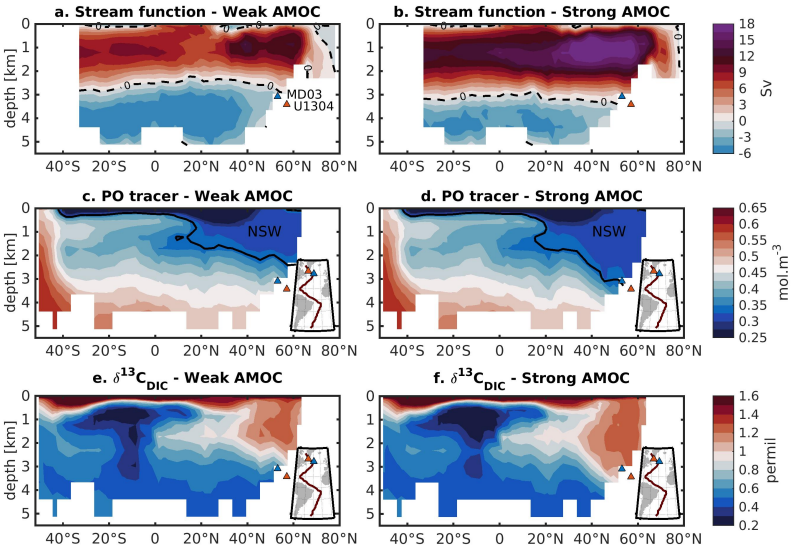

Figure 3. Atlantic section of (a, b) overturning stream function, (c, d) PO tracer and (d, e) $\delta^{13}C_{DIC}$. The panels on the left (a, c and e) correspond to the average over all the years of weak AMOC (i.e., two standard deviations below the long-term mean). The right side panels (b, d and f) correspond to the strong AMOC points average (i.e., two standard deviations above the long-term mean). The black dashed- lines on the top panels represent the zero line and symbolize the separation between the upper to bottom cells. In the middle panels the region above the black solid lines show the approximate area that is predominantly occupied by NSW. The value ($\sim$0.36 mol m^{-3}) represents the averaged surface PO over the sinking region south of Greenland.

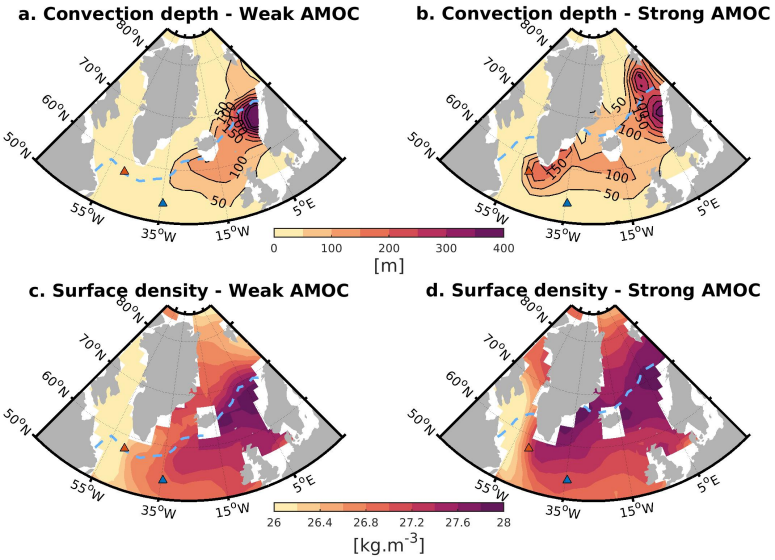

Figure 4. Convection (top panels) and neutral density (bottom panels) at the surface averaged over weak (a,c) and strong (b,d) AMOC years. The light blue dashed lines represent the 15 cm sea-ice thickness limit, as a proxy for sea-ice cover.

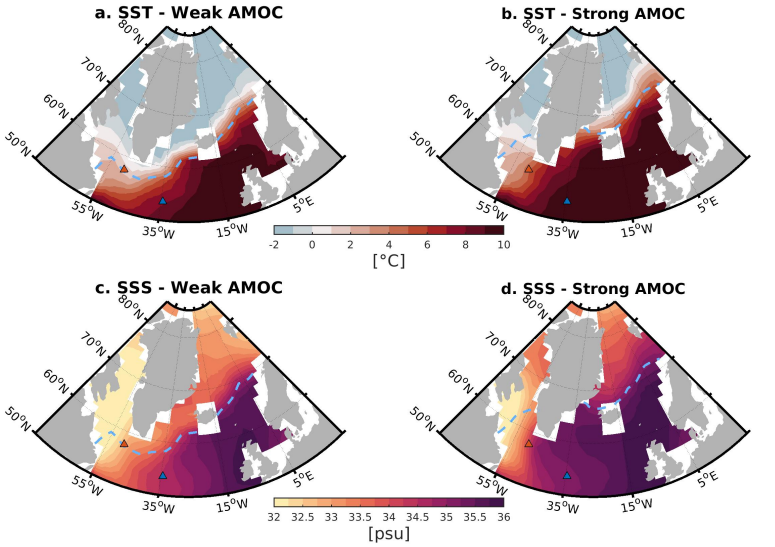

Figure 5. Sea surface temperature (SST, top panels) and salinity (SSS, bottom panels) averaged over the weak (a,c) and strong (b,d) AMOC years. The light blue dashed lines represent the 15 cm sea-ice thickness limit.

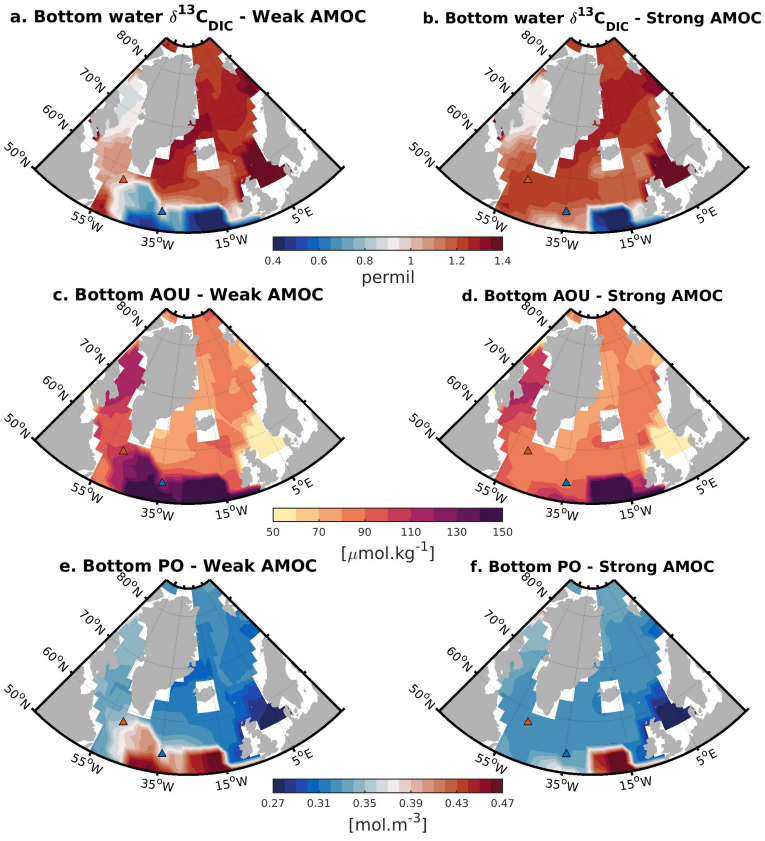

Figure 6. $\delta^{13}C_{DIC}$ (top panels), AOU (middle panels) and PO (bottom panels) averaged fields at the sea floor during the weak (left hand side) and strong (right hand side) AMOC years.

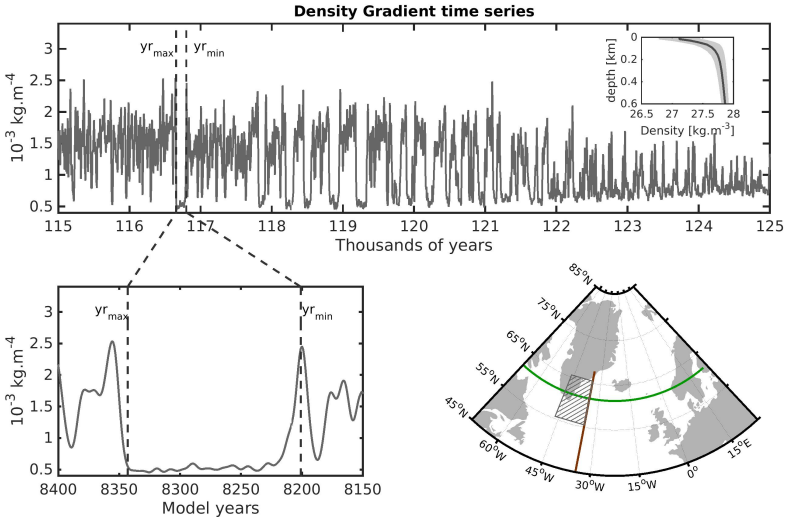

Figure 7. Time series of the vertical density gradient averaged over the first 600 m depth at the location where the convection activates and deactivates south of Greenland (top panel). The sub-panel shows the averaged density profile for this area in dark gray thick line, while the standard deviation is depicted by the shaded area. The bottom left panel represents a zoom in on the positive peak of AMOC around 116.7ka, which corresponds to a negative peak of vertical density gradient. We note yr_{min} (116.799ka) the initial year of the upward (downward) trend of the AMOC (vertical density gradient) and yr_{max} (116.657ka) the last maximum (minimum) value of the AMOC (vertical density gradient). The area where the convection activates and deactivates is represented in the bottom right panel by the hatched area. The longitudinal and latitudinal sections shown in Fig. 8 and Fig. 9 are represented by the green and brown solid lines.

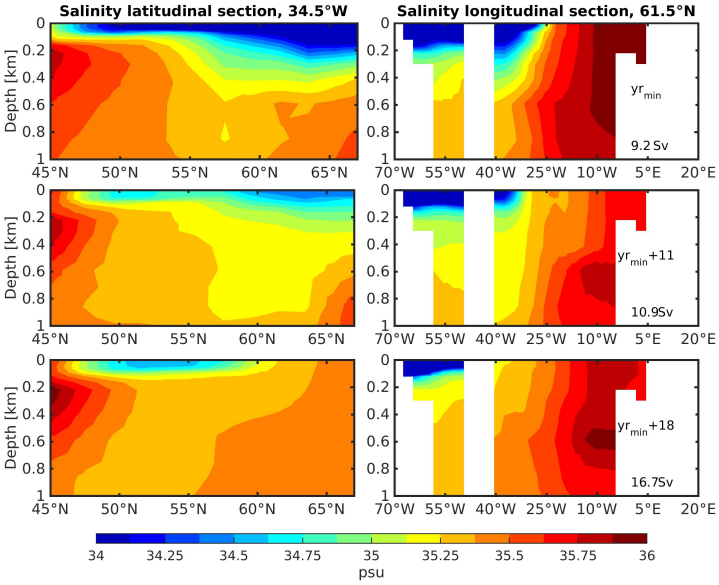

Figure 8. Vertical sections of the salinity in the North Atlantic along (left panels) the longitude 34.5°W and (right panels) the latitude 61.5°N. The first row corresponds to the initial year of the upward trend of the AMOC in 116.799ka (yr_{min}). The middle row represents the state of the ocean salinity 11 years after the AMOC starts to increase, while the last row corresponds to the end of the onset of this event when the AMOC reaches the nearly maximum (simulated 18 years after yr_{min}).

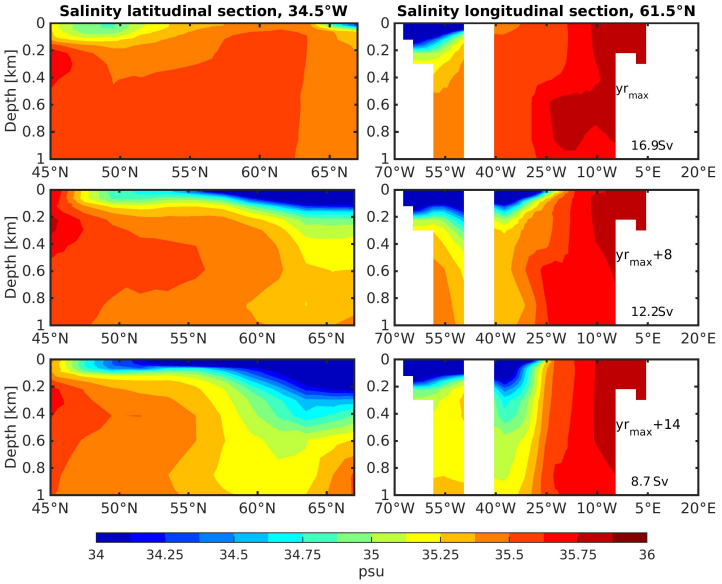

Figure 9. Similar to Fig. 8, but for the offset of the upward AMOC trend. Here, yr_{max} represents the last maximum value of the AMOC in 116.657ka (142 years after yr_{min}) before it starts to decrease to finally reach its minimum at yr_{max}+14.

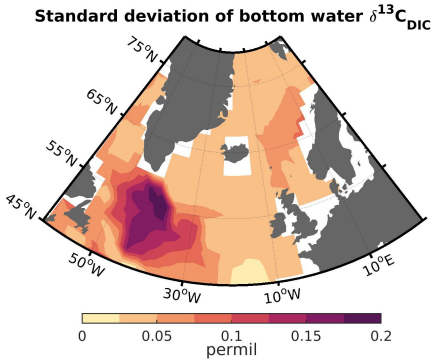

Figure 10. Standard deviation of bottom water $\delta^{13}C_{DIC}$ over the entire simulation.

Bibliography

Adkins, J. F., E. A. Boyle, L. Keigwin, and E. Cortijo (1997), Variability of the north atlantic thermohaline circulation during the last interglacial period, *Nature*, *390*(6656), 154, doi:10.1038/36540. 1.2.3

Arzel, O., M. H. England, A. C. de Verdiere, and T. Huck (2012), Abrupt millennial variability and interdecadal-interstadial oscillations in a global coupled model: sensitivity to the background climate state, *Climate dynamics*, *39*(1-2), 259–275, doi:10.1007/s00382-011-1117-y. 1.2.2

Bakker, P., A. Govin, D. J. Thornalley, D. M. Roche, and H. Renssen (2015), The evolution of deep-ocean flow speeds and δ13c under large changes in the atlantic overturning circulation: Toward a more direct model-data comparison, *Paleoceanography*, *30*(2), 95–117. 1.2.3, 2

Barker, S., G. Knorr, R. L. Edwards, F. Parrenin, A. E. Putnam, L. C. Skinner, E. Wolff, and M. Ziegler (2011), 800,000 years of abrupt climate variability, *science*, *334*(6054), 347–351, doi:10.1126/science.1203580. 1.2.2

Barker, S., J. Chen, X. Gong, L. Jonkers, G. Knorr, and D. Thornalley (2015), Icebergs not the trigger for north atlantic cold events, *Nature*, *520*(7547), 333–336, doi:10.1038/nature14330. 1.2.2

Blunier, T., and E. J. Brook (2001), Timing of millennial-scale climate change in antarctica and greenland during the last glacial period, *Science*, *291*(5501), 109–112, doi:10.1126/science.291.5501.109. 1.2.2

Bond, G. C., and R. Lotti (1995), Iceberg discharges into the north atlantic on millennial time scales during the last glaciation, *Science*, *267*(5200), 1005–1010, doi:10.1126/science.267.5200.1005. 1.2.2

Broecker, W., and D. McGee (2013), The 13c record for atmospheric co2: What is it trying to tell us?, *Earth and Planetary Science Letters*, *368*, 175–182, doi:10.1016/j.epsl.2013.02.029. 1.2.4

Broecker, W. S. (1994), Massive iceberg discharges as triggers for global climate change, *Nature*, *372*(6505), 421–424, doi:10.1038/372421a0. 1.2.2

Brown, N., and E. D. Galbraith (2016), Hosed vs. unhosed: interruptions of the atlantic meridional overturning circulation in a global coupled model, with and without freshwater forcing., *Climate of the Past*, *12*(8), doi:10.5194/cp-12-1663-2016. 1.2.2

Buckley, M. W., and J. Marshall (2016), Observations, inferences, and mechanisms of the atlantic meridional overturning circulation: A review, *Reviews of Geophysics*, *54*(1), 5–63, doi:10.1002/2015RG000493. 1.2.1

Castellana, D., S. Baars, F. W. Wubs, and H. A. Dijkstra (2019), transition probabilities of noise-induced transitions of the atlantic ocean circulation, *Scientific Reports*, *9*(1), 1–7, doi:10.1038/s41598-019-56435-6. 1.1

Clark, P. U., N. G. Pisias, T. F. Stocker, and A. J. Weaver (2002), The role of the thermohaline circulation in abrupt climate change, *Nature*, *415*(6874), 863–869, doi:10.1038/415863a. 1.2.1, 1.2.2

Clement, A. C., and L. C. Peterson (2008), Mechanisms of abrupt climate change of the last glacial period, *Reviews of Geophysics*, *46*(4), doi:10.1029/2006RG000204. 1.2.2

Clement, A. C., M. A. Cane, and R. Seager (2001), An orbitally driven tropical source for abrupt climate change, *Journal of Climate*, *14*(11), 2369–2375, doi:10.1175/1520-0442(2001)014<2369:AODTSF>2.0.CO;2. 1.2.2

Colville, E. J., A. E. Carlson, B. L. Beard, R. G. Hatfield, J. S. Stoner, A. V. Reyes, and D. J. Ullman (2011), Sr-nd-pb isotope evidence for ice-sheet presence on southern greenland during the last interglacial, *Science*, *333*(6042), 620–623, doi:10.1126/science.1204673. 1.2.3

Craig, H. (1957), Isotopic standards for carbon and oxygen and correction factors for mass-spectrometric analysis of carbon dioxide, *Geochimica et cosmochimica acta*, *12*(1-2), 133–149, doi:10.1016/0016-7037(57)90024-8. 1.2.4

Crowley, T. J. (1992), North atlantic deep water cools the southern hemisphere, *Paleoceanography*, *7*(4), 489–497, doi:10.1029/92PA01058. 1.2.2

Crucifix, M. (2005), Distribution of carbon isotopes in the glacial ocean: a model study, *Paleoceanography*, *20*(4), doi:10.1029/2005PA001131. 1.2.4

Curry, W. B., and D. W. Oppo (2005), Glacial water mass geometry and the distribution of δ13c of σco2 in the western atlantic ocean, *Paleoceanography*, *20*(1), doi:10.1029/2004PA001021. 1.2.4

Dansgaard, W., S. Johnsen, H. Clausen, D. Dahl-Jensen, N. Gundestrup, C. Hammer, and H. Oeschger (1984), North atlantic climatic oscillations revealed by deep greenland ice cores, *Climate processes and climate sensitivity*, *29*, 288–298, doi:10.1029/GM029p0288. 1.2.2

De Ruijter, W., A. Biastoch, S. Drijfhout, J. Lutjeharms, R. Matano, T. Pichevin, P. Van Leeuwen, and W. Weijer (1999), Indian-atlantic interocean exchange: Dynamics, estimation and impact, *Journal of Geophysical Research: Oceans*, *104*(C9), 20,885–20,910, doi:10.1029/1998JC900099. 1.2.1

de Vries, P., and S. L. Weber (2005), The atlantic freshwater budget as a diagnostic for the existence of a stable shut down of the meridional overturning circulation, *Geophysical Research Letters*, *32*(9), doi:10.1029/2004GL021450. 1.2.2

Demény, A., Z. Kern, G. Czuppon, A. Németh, S. Leél-Őssy, Z. Siklósy, K. Lin, H.-M. Hu, C.-C. Shen, T. W. Vennemann, et al. (2017), Stable isotope compositions of speleothems from the last interglacial–spatial patterns of climate fluctuations in europe, *Quaternary Science Reviews*, *161*, 68–80, doi:10.1016/j.quascirev.2017.02.012. 1.2.3

Denton, G. H., R. B. Alley, G. C. Comer, and W. S. Broecker (2005), The role of seasonality in abrupt climate change, *Quaternary Science Reviews*, *24*(10-11), 1159–1182, doi:10.1016/j.quascirev.2004.12.002. 1.2.2

Drijfhout, S., E. Gleeson, H. A. Dijkstra, and V. Livina (2013), Spontaneous abrupt climate change due to an atmospheric blocking–sea-ice–ocean feedback in an unforced climate model simulation, *Proceedings of the National Academy of Sciences*, *110*(49), 19,713–19,718, doi:10.1073/pnas.1304912110. 1.2.2

Drijfhout, S. S., S. L. Weber, and E. van der Swaluw (2011), The stability of the moc as diagnosed from model projections for pre-industrial, present and future climates, *Climate Dynamics*, *37*(7-8), 1575–1586, doi:10.1007/s00382-010-0930-z. 1.2.2

Duplessy, J., N. Shackleton, R. Fairbanks, L. Labeyrie, D. Oppo, and N. Kallel (1988), Deepwater source variations during the last climatic cycle and their impact on the global deepwater circulation, *Paleoceanography*, *3*(3), 343–360, doi:10.1029/PA003i003p00343. 1.2.4

Eide, M., A. Olsen, U. S. Ninnemann, and T. Johannessen (2017a), A global ocean climatology of preindustrial and modern ocean δ13c, *Global Biogeochemical Cycles*, *31*(3), 515–534, doi:10.1002/2016GB005473. 1.2.4, 1.2.4

Eide, M., A. Olsen, U. S. Ninnemann, and T. Johannessen (2017b), A global ocean climatology of preindustrial and modern ocean δ13c, *Global Biogeochemical Cycles*, *31*(3), 515–534, doi:10.1002/2016GB005473. 1.4, 1.2.4

Emile-Geay, J., M. A. Cane, N. Naik, R. Seager, A. C. Clement, and A. van Geen (2003), Warren revisited: Atmospheric freshwater fluxes and why is no deep water formed in the north pacific, *Journal of Geophysical Research: Oceans*, *108*(C6), doi:10.1029/2001JC001058. 1.2.1

Foster, T. D., and E. C. Carmack (1976), Frontal zone mixing and antarctic bottom water formation in the southern weddell sea, in *Deep Sea Research and Oceanographic Abstracts*, vol. 23, pp. 301–317, Elsevier, doi:10.1016/0011-7471(76)90872-X. 1.2.1

Frankignoulle, M., C. Canon, and J.-P. Gattuso (1994), Marine calcification as a source of carbon dioxide: Positive feedback of increasing atmospheric co2, *Limnology and Oceanography*, *39*(2), 458–462, doi:10.4319/lo.1994.39.2.0458. 3.2

Friedrich, T., A. Timmermann, L. Menviel, O. Elison Timm, A. Mouchet, and D. Roche (2010), The mechanism behind internally generated centennial-to-millennial scale climate variability in an earth system model of intermediate complexity, *Geoscientific Model Development*, *3*(2), 377–389, doi:10.5194/gmd-3-377-2010. 1.2.2

Fronval, T., and E. Jansen (1996), Rapid changes in ocean circulation and heat flux in the nordic seas during the last interglacial period, *Nature*, *383*(6603), 806–810, doi:10.1038/383806a0. 1.2.3

Galaasen, E. V., U. S. Ninnemann, N. Irvalı, H. K. F. Kleiven, Y. Rosenthal, C. Kissel, and D. A. Hodell (2014), Rapid reductions in north atlantic deep water during the peak of the last interglacial period, *Science*, *343*(6175), 1129–1132, doi:10.1126/science.1248667. 1.2.3, 2, 2.1, 3.1, 3.2

Galaasen, E. V., U. S. Ninnemann, A. Kessler, N. Irvalı, Y. Rosenthal, J. Tjiputra, N. Bouttes, D. M. Roche, H. K. F. Kleiven, and D. A. Hodell (2020), Interglacial instability of north atlantic deep water ventilation, *Science*, *367*(6485), 1485–1489, doi:10.1126/science.aay6381. 1.2.3, 1.3, 1.2.3, 1.4, 3.2

Ganachaud, A., and C. Wunsch (2000), Improved estimates of global ocean circulation, heat transport and mixing from hydrographic data, *Nature*, *408*(6811), 453, doi:10.1038/35044048. 1.2.1

Ganopolski, A., and S. Rahmstorf (2001), Rapid changes of glacial climate simulated in a coupled climate model, *Nature*, *409*(6817), 153–158, doi:10.1038/35051500. 1.2.2

Gildor, H., and E. Tziperman (2003), Sea-ice switches and abrupt climate change, *Philosophical Transactions of the Royal Society of London. Series A: Mathematical, Physical and Engineering Sciences*, *361*(1810), 1935–1944, doi:10.1098/rsta.2003.1244. 1.2.2

Gutjahr, M., and J. Lippold (2011), Early arrival of southern source water in the deep north atlantic prior to heinrich event 2, *Paleoceanography*, *26*(2), doi:10.1029/2011PA002114. 1.2.2

Heinrich, H. (1988), Origin and consequences of cyclic ice rafting in the northeast atlantic ocean during the past 130,000 years, *Quaternary research*, *29*(2), 142–152, doi:10.1016/0033-5894(88)90057-9. 1.2.2

Hemming, S. R. (2004), Heinrich events: Massive late pleistocene detritus layers of the north atlantic and their global climate imprint, *Reviews of Geophysics*, *42*(1), doi:10.1029/2003RG000128. 1.2.2

Henry, L., J. McManus, W. Curry, N. Roberts, A. Piotrowski, and L. Keigwin (2016), North atlantic ocean circulation and abrupt climate change during the last glaciation, *Science*, *353*(6298), 470–474, doi:10.1126/science.aaf5529. 1.2.2

Hilting, A. K., L. R. Kump, and T. J. Bralower (2008), Variations in the oceanic vertical carbon isotope gradient and their implications for the paleocene-eocene biological pump, *Paleoceanography*, *23*(3), doi:10.1029/2007PA001458. 1.2.4

Hodell, D. A., E. K. Minth, J. H. Curtis, I. N. McCave, I. R. Hall, J. E. Channell, and C. Xuan (2009), Surface and deep-water hydrography on gardar drift (iceland basin) during the last interglacial period, *Earth and Planetary Science Letters*, *288*(1-2), 10–19, doi:10.1016/j.epsl.2009.08.040. 1.2.3, 2, 2.1, 3.1

Hoffman, J. S., P. U. Clark, A. C. Parnell, and F. He (2017), Regional and global sea-surface temperatures during the last interglaciation, *Science*, *355*(6322), 276–279, doi:10.1126/science.aai8464. 1.2.3

Irvalı, N., U. S. Ninnemann, H. K. F. Kleiven, E. V. Galaasen, A. Morley, and Y. Rosenthal (2016), Evidence for regional cooling, frontal advances, and east greenland ice sheet changes during the demise of the last interglacial, *Quaternary Science Reviews*, *150*, 184–199, doi:10.1016/j.quascirev.2016.08.029. 1.2.3

Kageyama, M., A. Paul, D. M. Roche, and C. J. Van Meerbeeck (2010), Modelling glacial climatic millennial-scale variability related to changes in the atlantic meridional overturning circulation: a review, *Quaternary Science Reviews*, *29*(21-22), 2931–2956, doi:10.1016/j.quascirev.2010.05.029. 1.2.2

Kageyama, M., P. Braconnot, S. P. Harrison, A. M. Haywood, J. H. Jungclaus, B. L. Otto-Bliesner, J.-Y. Peterschmitt, A. Abe-Ouchi, S. Albani, P. J. Bartlein, et al. (2018), The pmip4 contribution to cmip6–part 1: Overview and over-arching analysis plan, *Geoscientific Model Development*, *11*(3), 1033–1057, doi:10.5194/gmd-11-1033-2018. 3.2

Kaspar, F., N. Kühl, U. Cubasch, and T. Litt (2005), A model-data comparison of european temperatures in the eemian interglacial, *Geophysical Research Letters*, *32*(11), doi:10.1029/2005GL022456. 1.2.3

Kaspi, Y., R. Sayag, and E. Tziperman (2004), A triple sea-ice state mechanism for the abrupt warming and synchronous ice sheet collapses during heinrich events, *Paleoceanography*, *19*(3), doi:10.1029/2004PA001009. 1.2.2

Kleinen, T., V. Brovkin, and G. Munhoven (2016), Modelled interglacial carbon cycle dynamics during the holocene, the eemian and marine isotope stage (mis) 11, *Climate of the Past*, *12*(12), 2145–2160, doi:10.5194/cp-12-2145-2016. 3.2

Kopp, R. E., F. J. Simons, J. X. Mitrovica, A. C. Maloof, and M. Oppenheimer (2009), Probabilistic assessment of sea level during the last interglacial stage, *Nature*, *462*(7275), 863, doi:10.1038/nature08686. 1.2.3, 3.2

Kuhlbrodt, T., A. Griesel, M. Montoya, A. Levermann, M. Hofmann, and S. Rahmstorf (2007), On the driving processes of the atlantic meridional overturning circulation, *Reviews of Geophysics*, *45*(2), doi:0.1029/2004RG000166. 1.2.1

Li, C., and A. Born (2019), Coupled atmosphere-ice-ocean dynamics in dansgaard-oeschger events, *Quaternary Science Reviews*, *203*, 1–20, doi:10.1016/j.quascirev.2018.10.031. 3.2

Li, C., D. S. Battisti, D. P. Schrag, and E. Tziperman (2005), Abrupt climate shifts in greenland due to displacements of the sea ice edge, *Geophysical Research Letters*, *32*(19), doi:10.1029/2005GL023492. 1.2.2, 1.2.2

Li, C., D. S. Battisti, and C. M. Bitz (2010), Can north atlantic sea ice anomalies account for dansgaard–oeschger climate signals?, *Journal of climate*, *23*(20), 5457–5475, doi:10.1175/2010JCLI3409.1. 1.2.2

Liu, W., S.-P. Xie, Z. Liu, and J. Zhu (2017), Overlooked possibility of a collapsed atlantic meridional overturning circulation in warming climate, *Science Advances*, *3*(1), e1601,666, doi:10.1126/sciadv.1601666. 1.2.1, 1.2.2

Liu, Z., B. Otto-Bliesner, F. He, E. Brady, R. Tomas, P. Clark, A. Carlson, J. Lynch-Stieglitz, W. Curry, E. Brook, et al. (2009), Transient simulation of last deglaciation with a new mechanism for bølling-allerød warming, *Science*, *325*(5938), 310–314, doi:10.1126/science.1171041. 1.2.2

Lourantou, A., J. Chappellaz, J.-M. Barnola, V. Masson-Delmotte, and D. Raynaud (2010), Changes in atmospheric co2 and its carbon isotopic ratio during the penultimate deglaciation, *Quaternary Science Reviews*, *29*(17-18), 1983–1992, doi:10.1016/j.quascirev.2010.05.002. 2

Lynch-Stieglitz, J. (2017), The atlantic meridional overturning circulation and abrupt climate change, *Annual review of marine science*, *9*, 83–104, doi:10.1146/annurev-marine-010816-060415. 1.2.2

Lynch-Stieglitz, J., T. F. Stocker, W. S. Broecker, and R. G. Fairbanks (1995), The influence of air-sea exchange on the isotopic composition of oceanic carbon: Observations and modeling, *Global Biogeochemical Cycles*, *9*(4), 653–665, doi:10.1029/95GB02574. 1.2.4

MacAyeal, D. (1993), Binge/purge oscillations of the laurentide ice sheet as a cause of the north atlantic's heinrich events, *Paleoceanography*, *8*(6), 775–784, doi:10.1029/93PA02200. 1.2.2

Menviel, L., A. Timmermann, T. Friedrich, and M. England (2014), Hindcasting the continuum of dansgaard–oeschger variability: mechanisms, patterns and timing., *Climate of the Past*, *10*(1), doi:10.5194/cp-10-63-2014. 1.2.2

Menviel, L., J. Yu, F. Joos, A. Mouchet, K. Meissner, and M. England (2017), Poorly ventilated deep ocean at the last glacial maximum inferred from carbon isotopes: A data-model comparison study, *Paleoceanography*, *32*(1), 2–17, doi:10.1002/2016PA003024. 1.2.4

Mokeddem, Z., J. F. McManus, and D. W. Oppo (2014), Oceanographic dynamics and the end of the last interglacial in the subpolar north atlantic, *Proceedings of the National Academy of Sciences*, *111*(31), 11,263–11,268, doi:10.1073/pnas.1322103111. 1.2.3

Morée, A. L., J. Schwinger, and C. Heinze (2018), Southern ocean controls of the vertical marine δ 13 c gradient–a modelling study, *Biogeosciences*, *15*(23), 7205–7223, doi:10.5194/bg-15-7205-2018. 1.2.4

Nicholl, J. A., D. A. Hodell, B. D. A. Naafs, C. Hillaire-Marcel, J. E. Channell, and O. E. Romero (2012), A laurentide outburst flooding event during the last interglacial period, *Nature Geoscience*, *5*(12), 901, doi:10.1038/ngeo1622. 3.2

North Greenland Ice Core Project members, . (2004), High resolution record of northern hemisphere climate extending into the last interglacial period, *Nature*, *431*(7005), 147–151. 1.2

Oliver, K. I., B. A. Hoogakker, S. Crowhurst, G. Henderson, R. E. Rickaby, N. Edwards, and H. Elderfield (2010), A synthesis of marine sediment core δ 13 c data over the last 150 000 years, *Climate of the Past*, *6*, 645–673, doi:10.5194/cp-6-645-2010. 1.2.4

Oppo, D. W., M. Horowitz, and S. J. Lehman (1997), Marine core evidence for reduced deep water production during termination ii followed by a relatively stable substage 5e (eemian), *Paleoceanography*, *12*(1), 51–63, doi:10.1029/96PA03133. 1.2.3

Otto-Bliesner, B. L., S. J. Marshall, J. T. Overpeck, G. H. Miller, A. Hu, et al. (2006), Simulating arctic climate warmth and icefield retreat in the last interglaciation, *science*, *311*(5768), 1751–1753, doi:10.1126/science.1120808. 1.2.3, 1.2.3

Otto-Bliesner, B. L., N. Rosenbloom, E. J. Stone, N. P. McKay, D. J. Lunt, E. C. Brady, and J. T. Overpeck (2013), How warm was the last interglacial? new model–data comparisons, *Philosophical Transactions of the Royal Society A: Mathematical, Physical and Engineering Sciences*, *371*(2001), 20130,097, doi:10.1098/rsta.2013.0097. 1.2.3

Palter, J. B. (2015), The role of the gulf stream in european climate, *Annual review of marine science*, *7*, 113–137, doi:10.1146/annurev-marine-010814-015656. 1.2.1

Petersen, S. V., D. P. Schrag, and P. U. Clark (2013), A new mechanism for dansgaard-oeschger cycles, *Paleoceanography*, *28*(1), 24–30, doi:10.1029/2012PA002364. 1.2.2

Pierrehumbert, R. T. (2000), Climate change and the tropical pacific: The sleeping dragon wakes, *Proceedings of the National Academy of Sciences*, *97*(4), 1355–1358, doi:10.1073/pnas.97.4.1355. 1.2.2

Rahmstorf, S. (2002), Ocean circulation and climate during the past 120,000 years, *Nature*, *419*(6903), 207, doi:10.1038/nature01090. 1.1, 1.2.1, 1.2.2, 1.2, 1.2.2

Rahmstorf, S. (2006), Thermohaline ocean circulation, *Encyclopedia of quaternary sciences*, *5*. 1.2.1

Sakai, K., and W. Peltier (1997), Dansgaard–oeschger oscillations in a coupled atmosphere–ocean climate model, *Journal of Climate*, *10*(5), 949–970, doi:10.1175/1520-0442(1997)010<0949:DOOIAC>2.0.CO;2. 1.2.2

Schmittner, A. (2005), Decline of the marine ecosystem caused by a reduction in the atlantic overturning circulation, *Nature*, *434*(7033), 628–633, doi:10.1038/nature03476. 1.2.1

Schmittner, A., and E. D. Galbraith (2008), Glacial greenhouse-gas fluctuations controlled by ocean circulation changes, *Nature*, *456*(7220), 373–376, doi:10.1038/nature07531. 1.2.2

Schmittner, A., E. D. Galbraith, S. W. Hostetler, T. F. Pedersen, and R. Zhang (2007), Large fluctuations of dissolved oxygen in the indian and pacific oceans during dansgaard-oeschger oscillations caused by variations of north atlantic deep water subduction, *Paleoceanography*, *22*(3), doi:10.1029/2006PA001384. 1.2.2

Schmittner, A., N. Gruber, A. C. Mix, R. M. Key, A. Tagliabue, and T. K. Westberry (2013), Biology and air-sea gas exchange controls on the distribution of carbon isotope ratios (delta c-13) in the ocean, *Biogeosciences*, *10*(9), 5793–5816, doi:10.5194/bg-10-5793-2013. 1.2.4

Schneider, R., J. Schmitt, P. Köhler, F. Joos, and H. Fischer (2013), A reconstruction of atmospheric carbon dioxide and its stable carbon isotopic composition from the penultimate glacial maximum to the last glacial inception, *Climate of the Past*, *9*(6), 2507–2523, doi:10.5194/cp-9-2507-2013. 2

Schulz, M., A. Paul, and A. Timmermann (2002), Relaxation oscillators in concert: A framework for climate change at millennial timescales during the late pleistocene, *Geophysical Research Letters*, *29*(24), 46–1, doi:10.1029/2002GL016144. 1.2.2

Schuster, U., and A. J. Watson (2007), A variable and decreasing sink for atmospheric co2 in the north atlantic, *Journal of Geophysical Research: Oceans*, *112*(C11), doi:10.1029/2006JC003941. 1.2.1

Smeed, D., G. McCarthy, S. Cunningham, E. Frajka-Williams, D. Rayner, W. E. Johns, C. Meinen, M. Baringer, B. Moat, A. Duchez, et al. (2014), Observed decline of the atlantic meridional overturning circulation 2004–2012, *Ocean Science*, *10*(1), 29–38, doi:10.5194/os-10-29-2014. 1.1

Stein, R., K. Fahl, P. Gierz, F. Niessen, and G. Lohmann (2017), Arctic ocean sea ice cover during the penultimate glacial and the last interglacial, *Nature communications*, *8*(1), 1–13, doi:10.1038/s41467-017-00552-1. 3.2

Stocker, T. F., D. Qin, G.-K. Plattner, M. M. Tignor, S. K. Allen, J. Boschung, A. Nauels, Y. Xia, V. Bex, and P. M. Midgley (2014), Climate change 2013: The physical science basis. contribution of working group i to the fifth assessment report of ipcc the intergovernmental panel on climate change, doi:10.1017/CBO9781107415324. 1.1

Stommel, H. (1961), Thermohaline convection with two stable regimes of flow, *Tellus*, *13*(2), 224–230, doi:10.1111/j.2153-3490.1961.tb00079.x. 1.2.2

Stouffer, R. J., J. Yin, J. Gregory, K. Dixon, M. Spelman, W. Hurlin, A. Weaver, M. Eby, G. Flato, H. Hasumi, et al. (2006), Investigating the causes of the response of the thermohaline circulation to past and future climate changes, *Journal of Climate*, *19*(8), 1365–1387, doi:10.1175/JCLI3689.1. 1.2.2

Talley, L. D. (2013), Closure of the global overturning circulation through the indian, pacific, and southern oceans: Schematics and transports, *Oceanography*, *26*(1), 80–97, doi:10.5670/oceanog.2013.07. 1.2.1

Toggweiler, J., and B. Samuels (1995), Effect of drake passage on the global thermohaline circulation, *Deep Sea Research Part I: Oceanographic Research Papers*, *42*(4), 477–500, doi:10.1016/0967-0637(95)00012-U. 1.2.1

Tzedakis, P., R. N. Drysdale, V. Margari, L. C. Skinner, L. Menviel, R. H. Rhodes, A. S. Taschetto, D. A. Hodell, S. J. Crowhurst, J. C. Hellstrom, et al. (2018), Enhanced climate instability in the north atlantic and southern europe during the last interglacial, *Nature communications*, *9*(1), 1–14, doi:10.1038/s41467-018-06683-3. 1.2.3

Vellinga, M., and R. A. Wood (2002), Global climatic impacts of a collapse of the atlantic thermohaline circulation, *Climatic change*, *54*(3), 251–267, doi:10.1023/A:1016168827653. 1.2.1

Vettoretti, G., and W. R. Peltier (2015), Interhemispheric air temperature phase relationships in the nonlinear dansgaard-oeschger oscillation, *Geophysical Research Letters*, *42*(4), 1180–1189, doi:10.1002/2014GL062898. 1.2.2

Voelker, A. H., et al. (2002), Global distribution of centennial-scale records for marine isotope stage (mis) 3: a database, *Quaternary Science Reviews*, *21*(10), 1185–1212, doi:10.1016/S0277-3791(01)00139-1. 1.2.2

Warren, B. A. (1983), Why is no deep water formed in the north pacific?, *Journal of Marine Research*, *41*(2), 327–347, doi:10.1357/002224083788520207. 1.2.1

Weaver, A. J., J. Sedláček, M. Eby, K. Alexander, E. Crespin, T. Fichefet, G. Philippon-Berthier, F. Joos, M. Kawamiya, K. Matsumoto, et al. (2012), Stability of the atlantic meridional overturning circulation: A model intercomparison, *Geophysical Research Letters*, *39*(20), doi:10.1029/2012GL053763. 1.2.2

Weber, S. L., and S. S. Drijfhout (2007), Stability of the atlantic meridional overturning circulation in the last glacial maximum climate, *Geophysical Research Letters*, *34*(22), doi:10.1029/2007GL031437. 1.2.2

Weijer, W., W. Cheng, S. Drijfhout, A. Fedorov, A. Hu, L. Jackson, W. Liu, E. McDonagh, J. Mecking, and J. Zhang (2019), Stability of the atlantic meridional overturning circulation: A review and synthesis, *Journal of Geophysical Research: Oceans*, doi:10.1029/2019JC015083. 1.2.2

Winton, M. (1993), Deep decoupling oscillations of the oceanic thermohaline circulation, in *Ice in the climate system*, pp. 417–432, Springer, doi:10.1007/978-3-642-85016-5_24. 1.2.2

Zeebe, R. E., and D. Wolf-Gladrow (2001), *CO2 in seawater: equilibrium, kinetics, isotopes*, 65, Gulf Professional Publishing. 1.2.4

Zhang, J., P. Quay, and D. Wilbur (1995), Carbon isotope fractionation during gas-water exchange and dissolution of co2, *Geochimica et Cosmochimica Acta*, *59*(1), 107–114, doi:10.1016/0016-7037(95)91550-D. 1.2.4

Ziegler, M., P. Diz, I. R. Hall, and R. Zahn (2013), Millennial-scale changes in atmospheric co 2 levels linked to the southern ocean carbon isotope gradient and dust flux, *Nature Geoscience*, *6*(6), 457–461, doi:10.1038/ngeo1782. 1.2.4, 3.2

Graphic design: Communication Division, UiB / Print: Skipnes Kommunikasjon AS

uib.no

ISBN: 9788230865200 (print)
9788230864616 (PDF)